Interaction Notes

Note 340

June 1977

High Frequency Surface Current and Charge
Densities Induced on Aircraft by
a Plane Electromagnetic Wave

C. L. Yu and W. D. Burnside
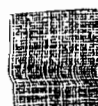Ohio State University Electro-Science Laboratory
Columbus, Ohio

ABSTRACT

Surface current and charge densities induced on aircraft
fuselage by an electromagnetic plane wave of arbitrary inci-
dence at high frequencies is the object of this research. The
primary goal of this investigation is to develop a theoretical
solution for predicitng the induced surface and charge densities
on aircraft fuselage in an accurate and efficient manner. Since
it is a study of general-type aircraft, the aircraft is modeled
in its most basic form. The fuselage is assumed to be an infin-
itely long, perfectly conducting elliptic cylinder in its cross-
section and a composite elliptic cylinder in its elevation
profile. The wing, cockpit, stabilizers (horizontal and vertical)
and landing gear are modeled by "n" sided bent or flat plates
which can be arbitrarily attached to the fuselage.

The solution developed in this study utilizes two elliptic
cylinders, namely the roll plane and elevation plane models to
approximate the principal surface profile (longitudinal and
transverse) at the observation location. With the belt concept
and the aid of appropriate coordinate system transformations
the solution can be used to predict the surface current and
charge densities induced on the fuselage in an accurate and
efficient manner. The radiation patterns due to infinitesimal
monopole and slot antennas on aircraft are related to the sur-
face current and charge densities induced on the antenna loca-
tion via the reciprocity theorem.

Interaction Notes

Note 340

June 1977

High Frequency Surface Current and Charge
Densities Induced on Aircraft by
a Plane Electromagnetic Wave

C. L. Yu and W. D. Burnside
Ohio State University Electro-Science Laboratory
Columbus, Ohio

ABSTRACT

Surface current and charge densities induced on aircraft
fuselage by an electromagnetic plane wave of arbitrary inci-
dence at high frequencies is the object of this research. The
primary goal of this investigation is to develop a theoretical
solution for predicitng the induced surface and charge densities
on aircraft fuselage in an accurate and efficient manner. Since
it is a study of general-type aircraft, the aircraft is modeled
in its most basic form. The fuselage is assumed to be an infin-
itely long, perfectly conducting elliptic cylinder in its cross-
section and a composite elliptic cylinder in its elevation
profile. The wing, cockpit, stabilizers (horizontal and vertical)
and landing gear are modeled by "n" sided bent or flat plates
which can be arbitrarily attached to the fuselage.

The solution developed in this study utilizes two elliptic
cylinders, namely the roll plane and elevation plane models to
approximate the principal surface profile (longitudinal and
transverse) at the observation location. With the belt concept
and the aid of appropriate coordinate system transformations
the solution can be used to predict the surface current and
charge densities induced on the fuselage in an accurate and
efficient manner. The radiation patterns due to infinitesimal
monopole and slot antennas on aircraft are related to the sur-
face current and charge densities induced on the antenna loca-
tion via the reciprocity theorem.

CONTENTS

Page

SECTION I

INTRODUCTION

The object of the research is to calculate the surface current and charge density induced on aircraft by an incident electromagnetic plane wave. The primary goal of this investigation is to develop a theoretical solution for predicting the induced surface current and charge densities on the aircraft fuselage in an accurate and efficient manner. Since it is a study of general-type aircraft, the aircraft is modeled in its most basic form. The fuselage is assumed to be an infinitely long perfectly-conducting elliptic cylinder in its cross-section and a composite elliptic cylinder in its elevation profile. The wing, cockpit and stabilizers (horizontal and vertical) are modeled by "n"-sided bent or flat plates which can be arbitrarily attached to the fuselage. The cylinder solution employed in the analysis is quite accurate and useful in that reasonable approximations are made in obtaining the necessary diffraction terms.

The surface current and charge density induced on the aircraft fuselage with plane-wave incidence are related to the radiation patterns due to fuselage-mounted, infinitesimal monopole and slot antennas. The relation between them will be discussed in the following. Let (E_m^θ, E_m^ϕ), (E_a^θ, E_a^ϕ) and (E_c^θ, E_c^ϕ) be the radiation patterns due to an infinitesimal monopole, axial slot and circumferential slot antenna respectively. Let $(\rho_S^{\theta^i}; \rho_S^{\phi^i})$ be the induced surface charge density, and $(J_\phi^{\theta^i}, J_\phi^{\phi^i})$, $(J_z^{\theta^i}, J_z^{\phi^i})$ be the induced surface current density due to $\hat{\theta}$- and $\hat{\phi}$-incident plane waves with unit electric field intensity. From the reciprocity theorem, the following relations exist:

$$|\rho_S^{\theta^i}| = 2\varepsilon_o \ |E_m^\theta|$$

$$|\rho_S^{\phi^i}| = 2\varepsilon_o \ |E_m^\phi|$$

$$|J_\phi^{\theta^i}| = \frac{2}{\eta} \ |E_a^\theta|$$

$$|J_\phi^{\phi^i}| = \frac{2}{\eta} \ |E_a^\phi|$$

$$|J_z^{\theta^i}| = \frac{2}{\eta} \ |E_c^\theta|$$

$$|J_z^{\phi^i}| = \frac{2}{\eta} \ |E_c^\phi|$$

3

Note that the fuselage axis is assumed to be the $\hat{z}$-axis of the conventional spherical coordinate system where θ (theta) is the angle measured from the z-axis and φ (phi) is the angle measured from the x-y plane. A θ-incident plane wave means the electric field intensity associated with the incident plane wave is θ-polarized. Similarly, a φ-incident plane wave means the electric field intensity is φ-polarized.

Since extensive experimental scale-model measurements for flush-mounted and blade antennas on aircraft are available for comparison, the analysis for the induced surface current and charge density is carried out in terms of antenna problems.

Based on the two principal plane (roll and elevation) model analyses from previous work [1] and extensive work on prolate spheroids [2], a numerical solution for the volumetric pattern of fuselage mounted antennas is developed. The solution present here not only predicts the volumetric pattern accurately, it also reduces computer time and improves computational efficiency considerably over that of a previous surface of revolution approach [2]. The validity and capability of this new solution are illustrated through comparison with extensive scale-model measurements performed at NASA (Hampton, Va.).

Among the first solutions used to compute on-aircraft antenna patterns were the modal solutions for infinitely long circular [4,5] and elliptical [6] cylinders. These solutions modeled the fuselage by a cylinder whose elliptical cross-section approximated the fuselage cross section at the antenna location. Arbitrary antennas were considered in these studies in which the antenna was mounted either on or above the fuselage. However, these solutions were not always adequate in that the effects of various scatterers such as wings and stabilizers were ignored.

A more recent approach for solving antenna pattern and impedance problems is the integral equation method via moment methods. By enforcing the boundary conditions on aircraft structure, the surface currents and the resulting scattered fields can be found. One of the first moment solutions applied to aircraft problems was the wire grid technique, developed by Richmond [7], using a point matching scheme [8]. This solution required the determination of approximately 100 unknown currents per square wavelength in order that the wire grid adequately model a perfectly conducting surface. A more sophisticated approach has been developed by Richmond [9] in which the reaction technique is used to solve for the unknown currents. Yet this solution still requires a wire grid model of the aircraft with approximately 100 unknown currents per square wavelength.

Another approach is the surface current model method [10] in which the surface of a conducting body is divided into patches with each patch having two orthogonal unknown complex currents. Using this approach, the unknown currents have been reduced to about 20 per square wavelength. Thus, one is able to consider a much larger surface using these surface patch solutions. However, all of these solutions are restricted to lower

4

frequencies, based on the fundamental limitation on the size of matrices which modern computers can solve without excessive loss of accuracy.

Another approach that has found great success at analyzing aircraft antennas is the Geometrical Theory of Diffraction (GTD). GTD is basically a high frequency solution which is divided into two basic problems; these being wedge diffraction and curved surface diffraction. The wedge diffraction solution has been applied to determine the radiation patterns of such basic antennas as parallel plate antennas [11,12,13], parallel plate arrays [14,15], horn antennas [16,17], parabolic reflectors [18,19], and rectangular waveguide antennas [20]. Both of these diffraction solutions have been applied in computing the patterns of antennas mounted on cylinders [21,22,23], rockets [24], wings [25,26], and aircraft [1,2, 27-32]. Using this approach, one applies a ray optics technique to determine components of the field incident on the various scatterers. Components of the diffracted field are found using the GTD solutions in terms of rays which are summed with the geometrical optics terms in the far field. The rays from a given scatterer tend to interact with the other structures causing various higher order terms. In this way one can trace out the various possible combinations of rays that interact between scatterers and determine and include only the dominant terms. Thus, one need only be concerned with the important scattering components and neglect all other higher-order terms. This makes the GTD approach ideal for a general high frequency study of aircraft antennas in that only the most basic structural features of the aircraft need to be modeled.

Since GTD is essentially a high frequency solution, the lower frequency limit of this solution is dictated by the spacings between the various scattering centers in that they should be at least a wavelength apart. In some cases even this requirement can be relaxed. Under this restriction, the low frequency limit is typically around 100 MHz. The upper frequency limit is dependent on how well the theoretical model simulates the important details of the actual structure.

The basic approach applied in the present study is based on previous work [1] which demonstrated the capability of the numerical solutions to predict the radiation patterns of fuselage mounted antennas in an efficient and economical way. If the volumetric patterns were found directly by analyzing rays on complex three-dimensonal surfaces as done previously in Reference [2], the resulting numerical solution would be very complex, time-consuming, and uneconomical. Nevertheless, if certain assumptions can be made, the approach undertaken previously can be used to overcome these difficulties and simplify the problem a great deal.

First, it has been shown by comparison with numerous scale model measurements that the roll plane model (an infinite elliptic cylinder with flat plate wings) can be extended to cover almost the complete volumetric pattern except for two conical sectors (fore and aft) [30]. The limitations of the roll plane model are due to the finite length of fuselage. Yet, the problem of finite length fuselage has been solved, previously, in an elevation plane analysis (an infinite composite

elliptic cylinder). Furthermore, based on previous three-dimensional studies of geodesic rays which contribute to the radiation pattern of an antenna on various prolate spheroids, one is able to combine the analysis of these two models to give the complete pattern.

In addition, the cockpit/radome section and vertical stabilizer previously ignored are taken into account in the present study. The cockpit/radome section and stabilizers are approximated by flat or bent plates which can be arbitrarily attached to the fuselage. This is an improvement over the previous roll plane model [1]. Using this approach, the complete volumetric pattern can be obtained with a model consisting of a composite elliptic cylinder to which are attached flat or bent plates. As a result of this simplified model, the solution is very efficient and requires little computer storage.

The basic theoretical background on the geometrical theory of diffraction (GTD) is presented in Section II. Both wedge diffraction and curved surface diffraction are discussed. The infinitely long elliptic cylinders (curved surfaces) is also presented in that section. This formulation is essential for fuselage mounted antennas. Section II also includes the near field scattering by a finite bent plate which is necessary for the determination of the scattering effects of secondary contributors such as wings, cockpit, and stabilizers.

Section III describes the mathematical model of the aircraft. This section starts with a review of the two principal plane (roll and elevation) analyses and their application to the radiation patterns. It, then, explains the way these two analyses are combined into a complete solution for the three dimensional aircraft model. The computer simulation method to approximate the cross section and elevation profile of an aircraft fuselage is also discussed.

Section IV presents the numerical results for the antenna patterns using these newly developed solutions. Volumetric patterns of both calculated and the experimental results are presented to demonstrate the validity and capability of this solution. Section V presents the calculated surface current and charge densities induced on various aircraft models. A complete volumetric pattern for the charge density induced on a Boing 737 is also presented in this section. Finally, a summary of the present study and a discussion of future topics are presented in Section VI.

SECTION II

THEORETICAL BACKGROUND

As stated in the introduction, the Geometrical Theory of Diffraction (GTD) is ideal for a general high frequency study of fuselage mounted aircraft antennas and induced surface densities of current and charge. This is particularly true when the scattering object is large in terms of the wavelength such as for electrically large aircraft. An aircraft shape is, in general, quite complex consisting of many complicated scattering structures. To be able to obtain an accurate radiation pattern, one must take these various scattering structures into account.

Based on past performance, the GTD has proven itself well suited to this type of analytical study. Not only does this approach fit nicely into a ray optics format, but it also provides a means of analyzing the effects of three-dimensional structures and identifying the significant contributions in the resulting antenna pattern. Consequently, the GTD is employed in this study to analyze the volumetric patterns of fuselage-mounted antennas.

The Geometrical Theory of Diffraction was introduced by Keller [33] as an extension of geometrical optics to include diffracted fields in the high frequency solution. The theory is based on the following postulates:

(1) The diffracted field propagates along rays which are determined by a generalization of Fermat's Principle to include points on edges, vertices, and smooth surfaces in the ray trajectory.

(2) Diffraction like reflection and transmission is a local phenomenon at high frequencies, i.e., it depends only on the nature of the boundary surface and the incident field in the immediate neighborhood of the point of diffraction.

(3) The diffracted wave propagates along its ray so that

  (a) power is conserved in a tube (or strip of rays),

  (b) the phase delay along the ray path equals the product of the wave number of the medium and the distance s.

Using these postulates, one can express the diffracted field in the same form as a geometrical optics field with some coefficient of proportionality to the incident field at the point of diffraction. The coefficient is determined from a canonical problem and is referred to as a diffraction coefficient.

For practical purposes, the GTD can be divided into two categories: (1) wedge diffraction theory - to treat diffraction by edges and (2) creeping wave theory - to treat diffraction by curved surfaces. The GTD has evolved considerably from its original form in References [34] and [35]. Consequently, descriptions of the wedge diffraction problem and the diffraction by a curved surface are presented in the following paragraphs.

1. DIFFRACTION BY A WEDGE

An asymptotic solution for the diffraction from a conducting wedge was first solved by Sommerfeld [36]. Originally, plane wave diffraction coefficients as presented by Keller were used as the sole GTD solution; however, as shown in Reference [37] diffraction of cylindrical waves is necessary in the treatment of antennas.

Pauli [38] introduced the V_B function as a practical formulation to the solution for a finite angle conducting wedge. Recently, however, Hutchins and Kouyoumjian [39,40] presented a formulation for the diffracted field (V_B), which significantly improves the accuracy over that obtained from Pauli's form. This improved diffraction solution [39,40] $V_B(L,\phi,n)$ provides superior results in the transition regions (near the incident and reflected shadow boundaries). It can be written in the form

$$V_B(L,\phi,n) = I_{-\pi}(L,\phi,n) + I_{+\pi}(L,\phi,n) \tag{1}$$

where

$$I_{\pm\pi}(L,\phi,n) = \frac{e^{-j(kL + \pi/4)}}{jn\sqrt{2\pi}} \; \sqrt{a} \, \cot\left(\frac{\pi\pm\phi}{2\,n}\right) \quad x \tag{2}$$

$$e^{jkLa} \int_{\sqrt{kLa}}^{\infty} e^{-j\tau^2} \, d\tau + [\text{higher-order terms}]$$

8

and where the higher-order terms are negligible for large kL and with n defined by the wedge angle [WA = (2-n)π]. Also, a = 1 + cos (φ-2nπN) and N is a positive or negative integer or zero, whichever most nearly satisfies the equations

$$2n\pi N-\phi = -\pi \qquad \text{for } I_{-\pi} \tag{3a}$$

$$2n\pi N-\phi = +\pi \qquad \text{for } I_{+\pi} \tag{3b}$$

The variables L and φ are defined later.

The three-dimensional wedge diffraction problem is depicted in Fig. 1. A source whose radiated $\bar{E}$ field is given by $\bar{E}^i(s)$ is located at point s'. It can be an arbitrary electric or magnetic source causing a plane, cylindrical, conical, or spherical wave incidence on the wedge. The diffracted vector field at observation point s can be written in terms of a dyadic diffraction coefficient. Kouyoumjian and Pathak [41,42] have given a more rigorous basis for the GTD formulation and have shown that the diffracted fields may be written compactly if they are in terms of a ray-fixed coordinate system. The ray-fixed coordinate system is centered at the point of diffraction Q_E (or points of diffraction in the case of plane wave incidence). Q_E is a unique point (or points) for a given source and observation point. The incident ray diffracts as a cone of rays such that the half cone angle $\hat{\beta}_0 = \beta'_0$, the angle which the incident ray makes with the edge.

The relationship between the orthogonal unit vectors associated with the ray-fixed coordinate system ($\hat{s}', \hat{\beta}'_0, \hat{\phi}'; \hat{s}, \hat{\beta}_0, \hat{\phi}$) are given by

$$\begin{aligned}
\hat{I} &= -\hat{s}' \\
\hat{I} &= \hat{\beta}'_0 \times \hat{\phi}' \\
\hat{s} &= \hat{\beta}_0 \times \hat{\phi}
\end{aligned} \tag{4}$$

where $\hat{I}$ is the incident direction unit vector, and $\hat{s}$ is the diffraction direction unit vector. The diffracted field is, now, given by

$$\bar{E}^d(s) = \bar{E}^i(Q_E) \cdot \overline{\overline{D}}_E(\hat{s},\hat{I}) \, A(s) \, e^{-jks} \tag{5}$$

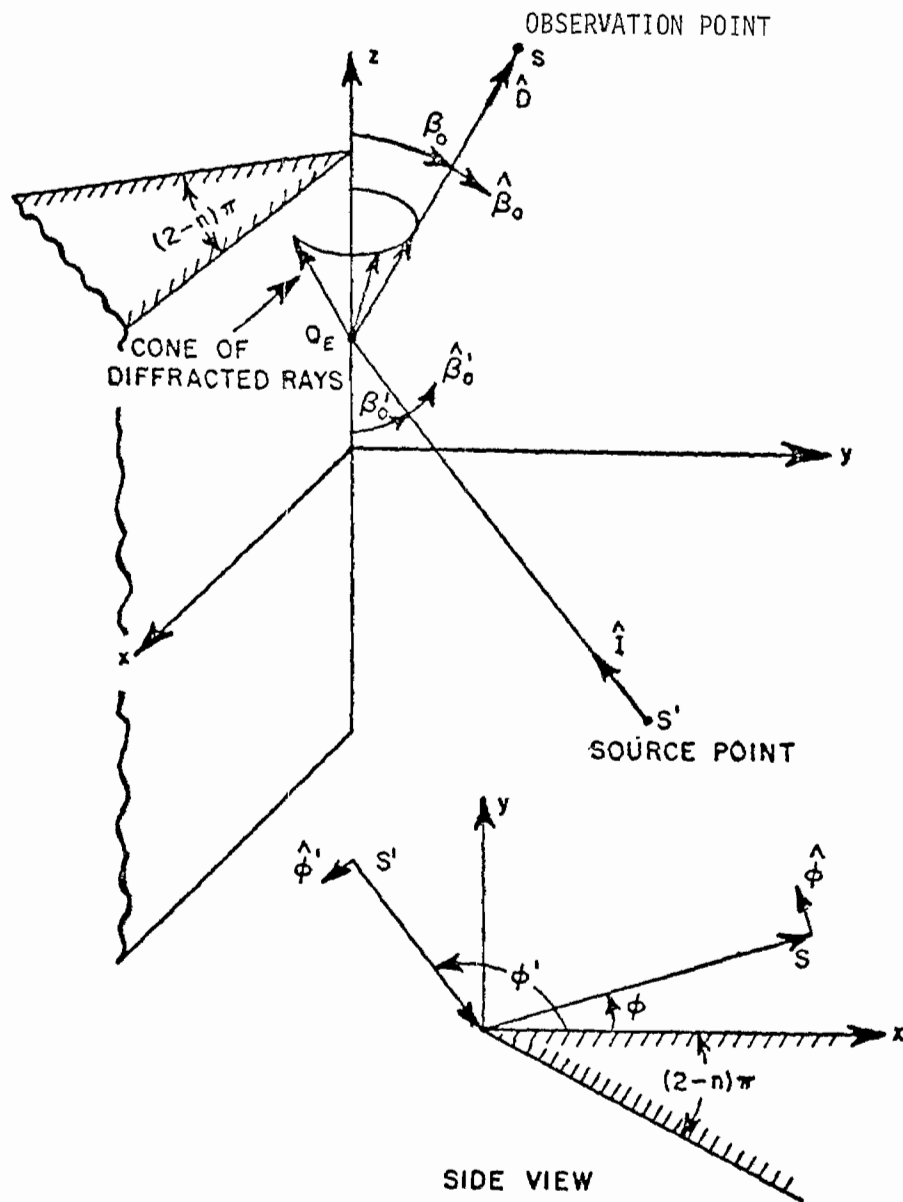The quantity A(s) is defined in Equation (13,) and Q_E is the diffraction point located on the edge.

9

Figure 1. Geometry for three-dimensional wedge diffraction problem.

Where

$$\overline{\overline{D}}_E(\hat{s},\hat{I}) = -\hat{\beta}_0' \hat{\beta}_0 D_s - \hat{\phi}'\hat{\phi} D_h \tag{6}$$

Equation (6) is a dyadic diffraction coefficient as given in Reference [41,42]. The quantities D_s and D_h are the scalar diffraction coefficients for the soft (Dirichlet) boundary condition at the surface of the wedge and the hard (Neumann) boundary condition, respectively. These diffraction coefficients D_s and D_h are related to the V_B function described earlier by a constant as

$$D_{\substack{s \\ h}} = \frac{\sqrt{L}\, e^{jkL}}{\sin\beta_0} V_B \mp \quad , \tag{7}$$

where L will be defined later when applied to straight edge.

For our purpose, it is more convenient to write the diffracted field in terms of the V_B function in Eq. (7) as*

$$\begin{bmatrix} E_\parallel^d(s) \\[2ex] E_\perp^d(s) \end{bmatrix} \sim \begin{bmatrix} -V_B^- & 0 \\[2ex] 0 & -V_B^+ \end{bmatrix} \begin{bmatrix} E_\parallel^i(Q_E) \\[2ex] E_\perp^i(Q_E) \end{bmatrix} \frac{\sqrt{L}\, e^{jkL}}{\sin\beta_0} A(s)\, e^{-jks} \tag{8}$$

where

$$V_B^{\mp} = V_B(L,\Phi^-,n) \mp V_B(L,\Phi^+,n) \tag{9}$$

The minus sign (V_B^-) applies for the $\overline{E}$-field vector parallel to the edge with boundary condition

$$(\overline{E}|_{wedge}) = 0 \tag{10}$$

_____

*If an edge fixed coordinate system is used, Eq. (8) takes the form of a 3 x 3 matrix.

11

The plus sign (V_B^+) applies for the $\bar{E}$-field vector perpendicular to the edge with boundary condition

$$\left(\frac{\partial \bar{E}}{\partial \bar{n}} \bigg|_{wedge} \right) = 0 \tag{11}$$

The angular relations are expressed by

$$\Phi = \phi^{\mp} = \phi \mp \phi' \tag{12}$$

where the minus sign (ϕ^-) is associated with the incident field and the plus sign (ϕ^+) with the reflected field. The quantity $A(s)$ is a ray divergence factor given by [41,42]

$$A(s) = \begin{cases} \dfrac{1}{\sqrt{s}} & \text{plane, cylindrical } (s = \rho), \\ & \quad \text{and conical wave incidence} \\[2mm] \sqrt{\dfrac{s'}{s(s'+s)}} & \text{spherical wave incidence} \end{cases} \tag{13}$$

and L, distance parameter, is given by [41,42]

$$L = \begin{cases} s \sin^2 \beta_o & \text{plane wave incidence} \\[2mm] \dfrac{\rho'\rho}{\rho + \rho'} & \text{cylindrical wave incidence} \\[2mm] \dfrac{s's \sin^2\beta_o}{s + s'} & \text{conical and spherical wave} \\ & \quad \text{incidence.} \end{cases} \tag{14}$$

For the two-dimensional wedge problem, illustrated in Fig. 2, where there is cylindrical wave incidence with $\beta_o = 90°$, Eq. (8) reduces to give

$$\begin{bmatrix} E_{\|}^d(\rho,\phi) \\[3mm] E_{\perp}^d(\rho,\phi) \end{bmatrix} \sim \begin{bmatrix} -V_B^- & 0 \\[3mm] 0 & -V_B^+ \end{bmatrix} \begin{bmatrix} E_{\|}^i(\rho',\phi') \\[3mm] E_{\perp}^i(\rho',\phi') \end{bmatrix} \sqrt{\frac{\rho'}{\rho + \rho'}} \ e^{jk\frac{\rho'\rho}{\rho+\rho'}} \ e^{-jk\rho}. \tag{15}$$

12

In the far field $(\rho \gg \rho')$, this becomes

$$\begin{bmatrix} E_{\parallel}^d(\rho,\phi) \\ \\ E_{\perp}^d(\rho,\phi) \end{bmatrix} \sim \begin{bmatrix} -V_B^- & 0 \\ \\ 0 & -V_B^+ \end{bmatrix} \begin{bmatrix} E_{\parallel}^i(\rho',\phi') \\ \\ E_{\perp}^i(\rho',\phi') \end{bmatrix} \sqrt{\rho'} \; e^{jk\rho'} \frac{e^{-jk\rho}}{\sqrt{\rho}} \qquad (16)$$

Putting this in ray form and factoring out $\dfrac{e^{-jk\rho}}{\sqrt{\rho}}$, one obtains

$$\begin{bmatrix} R_{\parallel}^d(\phi) \\ \\ R_{\perp}^d(\phi) \end{bmatrix} \sim \begin{bmatrix} -V_B^- & 0 \\ \\ 0 & -V_B^+ \end{bmatrix} \begin{bmatrix} R_{\parallel}^i(\phi') \\ \\ R_{\perp}^i(\phi') \end{bmatrix} \qquad (17)$$

The ray form used here is given by

$$\overline{E}(\rho,\phi) = \overline{R}(\phi) \frac{e^{-jk\rho}}{\sqrt{\rho}} \qquad (18)$$

Thus, $\overline{R}(\phi)$ is related to the far field pattern function.

For the three-dimensional wedge problem, where there is spherical wave incidence, Eq. (8) reduces to give

$$\begin{bmatrix} E_{\parallel}^d(s,\beta_0,\phi) \\ \\ E_{\perp}^d(s,\beta_0,\phi) \end{bmatrix} \sim \begin{bmatrix} -V_B^- & 0 \\ \\ 0 & -V_B^+ \end{bmatrix} \begin{bmatrix} E_{\parallel}^i(s',\beta_0',\phi') \\ \\ E_{\perp}^i(s',\beta_0',\phi') \end{bmatrix} \frac{s'}{s+s'} e^{\dfrac{jks's\,\sin^2\beta_0}{s+s'}} e^{-jks}$$

$$(19)$$

In the far field $(s \gg s')$, we have

$$\begin{bmatrix} E_{\parallel}^d(s,\beta_0,\phi) \\ \\ E_{\perp}^d(s,\beta_0,\phi) \end{bmatrix} \sim \begin{bmatrix} -V_B^- & 0 \\ \\ 0 & -V_B^+ \end{bmatrix} \begin{bmatrix} E_{\parallel}^i(s',\beta_0',\phi') \\ \\ E_{\perp}^i(s',\beta_0',\phi') \end{bmatrix} s'e^{jks'\sin^2\beta_0} \frac{e^{-jks}}{s}$$

$$(20)$$

Putting this in ray form and factoring out $\dfrac{e^{-jks}}{s}$, it is seen that

$$
\begin{bmatrix} R_{\parallel}^{d}(\beta_{0},\phi) \\[3ex] R_{\perp}^{d}(\beta_{0},\phi) \end{bmatrix} \sim \begin{bmatrix} -V_{B}^{-} & 0 \\[3ex] 0 & -V_{B}^{+} \end{bmatrix} \begin{bmatrix} R_{\parallel}^{i}(\beta_{0}',\phi') \\[3ex] R_{\perp}^{i}(\beta_{0}',\phi') \end{bmatrix} e^{-jks'} \cos^{2}\beta_{0}
\tag{21}
$$

It is interesting to note that in the principal plane ($\beta_0 = 90°$) the ray form of the three-dimensional case takes on the same form as the two-dimensional problem.

The total ray value at the observation point s is given by the sum of the geometrical optics terms and the diffracted terms

$$
\overline{R}^{T}(s) = \overline{R}^{G.O.}(s) + \overline{R}^{d}(s)
\tag{22}
$$

where

$$
\overline{R}^{G.O.}(s) = \begin{cases} \overline{R}^{i}(s) + \overline{R}^{r}(s) & \text{incident and reflected region I} \\[2ex] \overline{R}^{i}(s) & \text{incident region II} \\[2ex] 0 & \text{shadowed region III} \end{cases}
\tag{23}
$$

and $\overline{R}^{r}(s)$ may be determined from the image of the source term using basic geometrical optics techniques. These three regions are illustrated in Fig. 2 for a two-dimensional wedge diffraction problem.

2. DIFFRACTION BY A CURVED SURFACE

When an incident ray strikes a smooth, curved perfectly conducting surface at grazing incidence, i.e., at the shadow boundary, a part of its energy is diffracted into the shadow region. To describe this phenomenon, Keller [43] introduced a second class of diffracted rays which is now well known as creeping waves. These ray paths include the points Q_1 and Q_2 which form a curve on the diffracting surface, as illustrated in Fig. 3. However, the actual concept of creeping waves was introduced by Franz and Depperman [44,45]. The basic concept as presented in the following discussion is taken from "Asymptotic High-Frequency Methods" by Kouyoumjian [46].
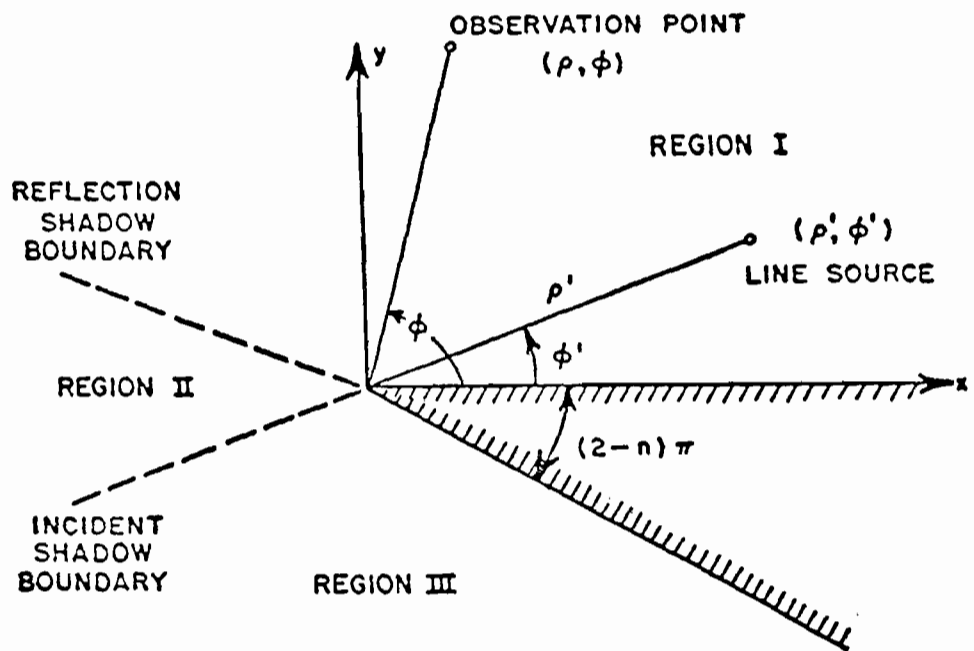
Figure 2. Two-dimensional wedge diffraction geometry.
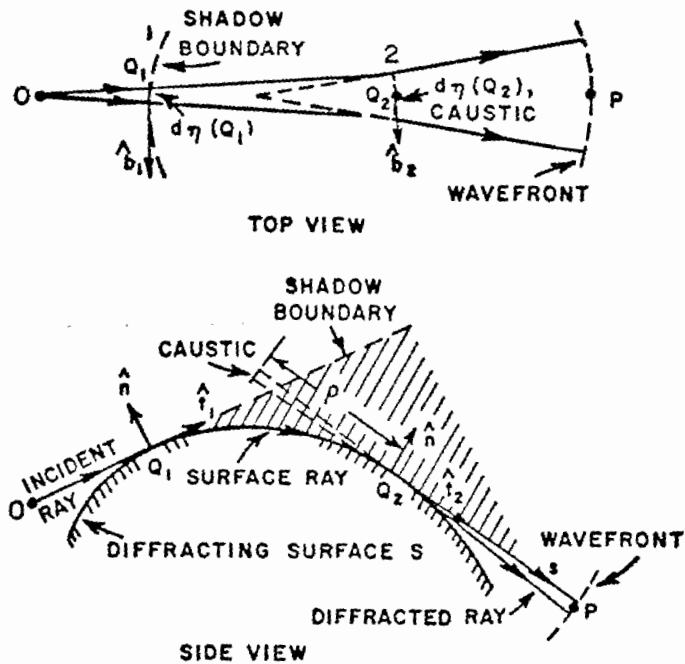
Figure 3. Diffraction by a smooth curved surface.

The diffraction by a smooth curved surface is shown in Fig. 3 in which O is the source point and P is the observation point in the shadow region. Applying Fermat's principle, the line OQ_1Q_2P is the shortest distance between O and P which does not penetrate the surface. In detail, a ray incident on the shadow boundary at Q_1 divides; one part of the incident energy continues straight on as predicted by geometrical optics, a second part follows the surface s into the shadow region as a surface ray shedding diffracted rays tangentially as it propagates where $\hat{t}$, $\hat{n}$, and $\hat{b}$ are the unit vectors in the direction of incidence, normal to the surface s and binormal to the surface ($\hat{b} = \hat{t} \times \hat{n}$), respectively. The incident field $\bar{E}^i(Q_1)$ may be resolved into its normal and binormal components ($\hat{n} \cdot \bar{E}^i(Q_1)$ and $\hat{b} \cdot \bar{E}^i(Q_1)$). It is assumed that these two components induce surface ray fields which propagate independently of each other along the geodesic arc between Q_1 and Q_2.

From Reference [46] the binormal surface ray field at Q_1 is related to the binormal component of the incident field at Q_1 by

$$A(Q_1) \ e^{j\phi(Q_1)} = D_s(Q_1) \ \hat{b}_1 \cdot \overline{E}^i(Q_1) \tag{24}$$

where $D_s(Q_1)$ is the scalar diffraction coefficient for a soft surface. The amplitude of the surface ray is assumed to be governed by the conservation of energy between a pair of adjacent surface rays. Hence, the amplitude behavior of the fields is given as

$$A(Q_2) = A(Q_1) \sqrt{\frac{dn_1}{dn_2}} \ e^{\left[-\int_{Q_1}^{Q_2} \alpha(t') \ dt' \right]} \tag{25}$$

where

> dn_1 and dn_2 = the separation between a pair of rays at Q_1 and Q_2, respectively.

> $\alpha(t)$ = the attenuation constant wich is a function of t, the coordinate along the surface ray, because it depends on the local radius of curvature and its derivatives.

The attenuation constant $\alpha(t)$ is introduced due to the tangential shedding of rays as the surface ray propagates. It is seen from Fig. 3 that Q_2 is a caustic of the diffracted field and the second caustic is located at a distance ρ from Q_2 Thus, the binormal component of the diffracted field which radiates from Q_2 towards P can be found, as in the previous edge diffraction case, with one of the caustics used as a reference point and is given by

$$\hat{b}_2 \cdot \overline{E}^d(P) = D_s(Q_2) \ A(Q_2) \ e^{j\phi(Q_2)} \sqrt{\frac{\rho}{s(\rho + s)}} \ e^{-jks} \tag{26}$$

From Eqs. (24), (25), and (26), there results

$$\hat{b}_2 \cdot \overline{E}^d(P) = \left[\hat{b}_1 \cdot \overline{E}^i(Q_1) \right] D_s(Q_1) \, D_s(Q_2) \sqrt{\frac{dn_1}{dn_2}} \sqrt{\frac{\rho}{s(\rho + s)}}$$

$$e^{-j\left[k(t+s) + \int_{Q_1}^{Q_2} \alpha(t') \, dt' \right]} \qquad (27)$$

It is found that $b_1 \cdot \overline{E}^i(Q_1)$ excites an infinity of surface ray modes each with its own diffraction coefficient and attenuation constant. Thus, the expression in Eq. (27) is replaced by

$$\hat{b}_2 \cdot \overline{E}^d(P) = \left[\hat{b}_1 \cdot \overline{E}^i(Q_1) \right] \sqrt{\frac{dn_1}{dn_2}} \sqrt{\frac{\rho}{s(\rho + s)}} \, e^{-j[k(t+s)]}$$

$$\left[\sum_m^{\infty} D_{sm}(Q_1) \, D_{sm}(Q_2) \, e^{- \int_{Q_1}^{Q_2} \alpha_m(t') \, dt'} \right] \qquad (28)$$

Equation (28) relates the diffracted field at P to the incident field at Q_1 for the soft surface boundary condition.

An expression similar to Eq. (28) is also obtained for the normal component of the incident field; in this case, the scalar diffraction coefficients and attenuation constants for the hard surface replace those of the soft surface. Therefore, the vector diffracted field at P can be written in terms of the electromagnetic field incident at Q_1 as

$$\overline{E}(P) = \left[\hat{n}_2 \hat{n}_1 \, v(1,2) + \hat{b}_2 \hat{b}_1 \, u(1,2) \right] \cdot \overline{E}^i(1) \sqrt{\frac{\rho}{s(\rho + s)}} \, e^{-jks} \qquad (29)$$

in which $v(1,2)$, $u(1,2)$ are

$$v(1,2) = u(1,2) = \sqrt{\frac{dn_1}{dn_2}} \, e^{-jkt} \sum_m^{\infty} D_m(1) \, D_m(2) \, e^{- \int_1^2 \alpha_m(t') \, dt'} \qquad (30)$$

18

with the subscripts h, s, respectively, added to D_m and α_m. Note that Q_1 and Q_2 have been replaced by 1 and 2 for the sake of brevity. Finding dn_1, dn_2, and ρ is simply a matter of differential geometry involving the rays and surface; this is discussed at length in Levy and Keller [43]. The generalized diffraction coefficient and attenuation constant can be found in Reference [47].

The diffraction thus far discussed is applied to the open curved surface. For a closed surface, each surface ray mode produced at Q_1 encircles the surface an infinite number of times. The length of the surface ray path for the nth encirclement is t+nT where T is the circumference of the closed surface. These multiple-encircling rays may be summed to contribute

$$\left[1 - e^{-jkT - \int_0^T \alpha_m(t') \, dt'} \right]$$

to the denominator of the diffracted field. It is interesting to note that there must be another pair of diffraction points, Q_3 and Q_4, for the closed surface as shown in Fig. 4. Therefore, the field at any point P in the shadow region is the sum of these two diffracted fields from Q_1-Q_2 and Q_3-Q_4. The total field at any point in the illuminated region is, by the superposition principle, the sum of incident, reflected and diffracted fields. A detailed discussion of this subject can be found in Reference [47].

3. DIFFRACTION BY AN INFINITELY LONG ELLIPTIC CYLINDER

An important special case of this GTD solution is the one in which the antenna is mounted directly on the curved surface. This is especially true for our purpose, since the radiation from slots and monopoles mounted on smooth curved surfaces is pertinent to the design of flush-mounted antennas for aircraft and spacecraft. Recently, Pathak and Kouyoumjian [48-51] have extended the GTD technique to treat the radiation from apertures or slots in convex perfectly conducting surfaces. This extension of GTD has been successfully applied to circular and elliptic cylinders, spheres, and spheroids. A similar GTD analysis of the radiation from monopoles on a convex surface has, also, been recently completed by Pathak and Luebbers [52] with the same degree of success.

19
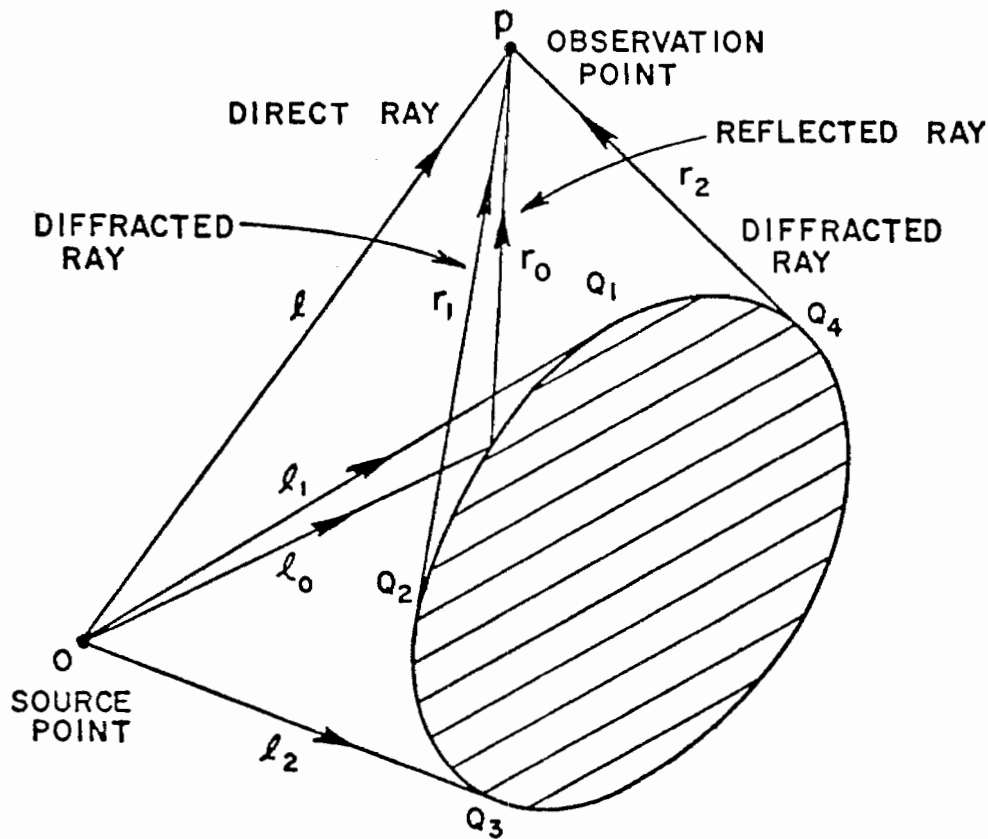
Figure 4. Diffraction by a smooth closed cylindrical surface.

The GTD solutions for analyzing the radiation of antennas mounted on convex surfaces are found from asymptotic solutions of appropriate canonical problems [48-51]. In the deep shadow region, the surface rays excited by the antennas account entirely for the field there; whereas, the geometrical optics ray field adequately describes the field in the illuminated region (for sufficiently large closed convex surfaces, the contribution from the surface rays is negligible). In the transition region adjacent to the shadow boundary, the Fock-type functions are employed to describe the field. This field reduces uniformly to the surface ray and geometrical optics solutions outside the transition regions. This modification in the transition regions is required since the ordinary ray solutions fail therein.

Using the GTD solution, a launching coefficient is introduced to relate the antenna field to the boundary layer surface waves which propagate around the surface along geodesic paths. Energy is continually diffracted by the surface wave in the tangent direction to the propagation path. This diffracted energy is related to the surface rays by a diffraction coefficient which is dependent on the surface geometry at the point of diffraction. The surface wave energy decays along the geodesic path in that energy is continually diffracted. This decay is expressed by an attenuation coefficient which is dependent on the surface geometry along the geodesic path.

The GTD solutions for infinitesimal slot and monopole antennas mounted on an elliptic cylinder as shown in Fig. 5 are given, with torsional effects included [49-52], by:

a. Monopole Case

(1) Illuminated region

$$\bar{E} = - \sin \theta_m \hat{\theta}_m F(source) \tag{31}$$

(2) Transition region

(a) Illuminated side

$$\bar{E} = \left\{ \hat{n} \cdot \frac{\hat{n}' \times \hat{s}_o}{\hat{z} \times \hat{s}_o} g^*(\xi) \right.$$

$$+ \hat{b} \left\{ (sgn) \left| \frac{\hat{n}' \cdot \hat{s}_o}{\left(\frac{k \, \rho_g(Q')}{2}\right)^{1/3}} \right|_\xi \sqrt{\frac{\rho_g(Q')}{\rho_\tau(Q')} - 1} \left[-j\left(\frac{2}{k \, \rho_g(Q')}\right)^{1/3} \right] \right\}$$

$$\left. \tilde{g}^*(\xi) \quad e^{-j(ks_o + \xi^3/3)} \right\} \cdot F(tangent) \tag{32}$$
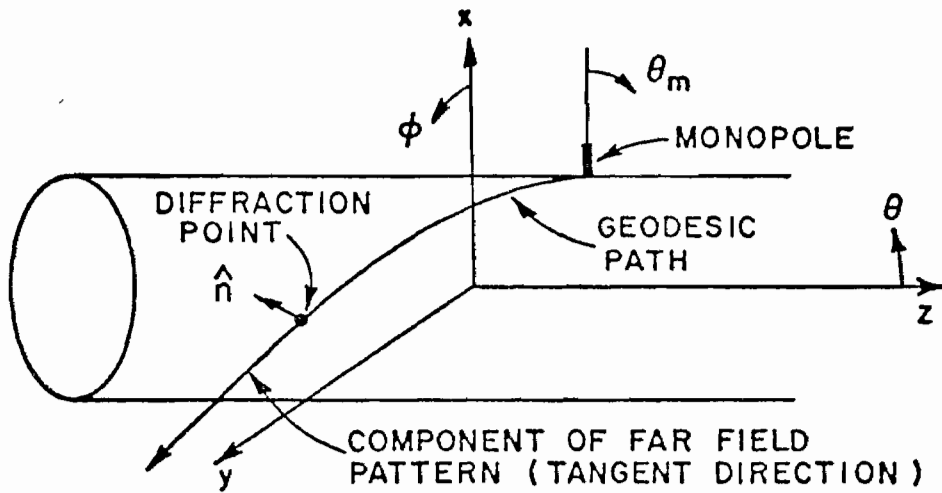
(a) GEOMETRY OF MONOPOLE PROBLEM
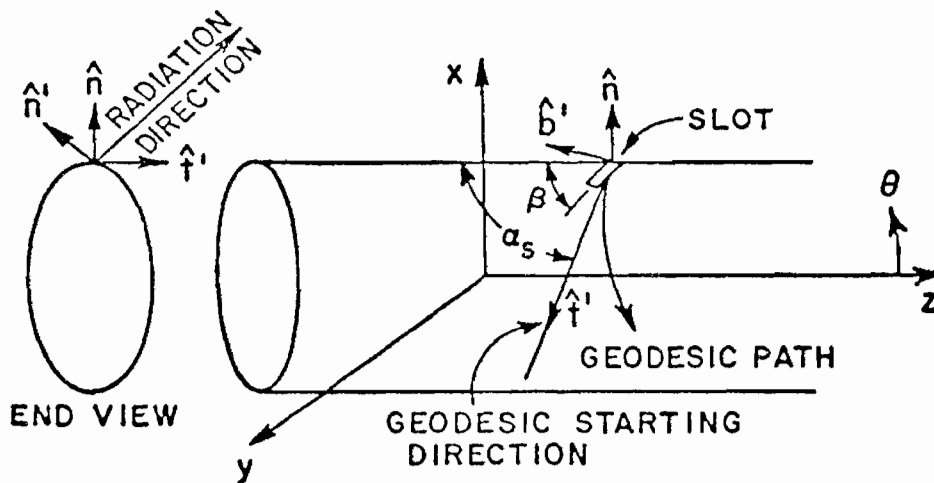
(b) GEOMETRY OF SLOT PROBLEM

Figure 5. Geometry of antennas mounted on an infinitely long elliptic cylinder.

22

(b) Shadow side

$$\bar{E} = \sqrt{\frac{d\psi_o}{d\psi}} \left[\frac{\rho_g(Q)}{\rho_g(Q')} \right]^{1/6} \left\{ \hat{n} \, g*(\xi) + \right.$$

$$\hat{b} \, (sgn) \sqrt{\frac{\rho_g(Q')}{\rho_\tau(Q')} - 1} \, \left[-j\left(\frac{2}{k\rho_g(Q')}\right) \right]^{1/3} \, \left. \tilde{g}*(\xi) \right\}$$

$$e^{-jk\ell} \cdot F \text{ (tangent)} \tag{33}$$

(3)   Deep Shadow Region

$$\bar{E} = \sum_j \left[\hat{n}_j \, E_j^h + \hat{b}_j (sgn) \sqrt{\frac{\rho_g(Q')}{\rho_\tau(Q')} - 1} \, E_j^s \right] \cdot F_j \text{ (tangent)} \tag{34}$$

b.   Slot Case

(1) Illuminated region

$$\bar{E} = [(\hat{e}_1 \sin \beta - \hat{e}_2 \cos \beta) \times \hat{s}] \cdot F \text{ (source)} \tag{35}$$

(2) Transition Region

(a) Lit side

$$\bar{E} = \frac{1}{2} \left\{ \hat{n} \left[\sin \alpha_s \cos \beta - \left| \frac{\hat{n}' \times \hat{s}_0}{\hat{z} \times \hat{s}_0} \right| \cos \alpha_s \sin \beta \right] g*(\xi) \right.$$

$$+ \hat{b} \, \frac{\rho_g(Q')}{\rho_\tau(Q')} \left| \frac{\hat{n}' \cdot \hat{s}_0}{\left[\frac{k\rho_g(Q')}{2}\right]^{1/3} \xi} \right| \left(-j\left[\frac{2}{k\rho_g(Q')}\right]^{1/3} \right)$$

$$\left. \sin \alpha_s \sin \beta \tilde{g}*(\xi) \right\} e^{-j(ks_0 + \xi^3/3)} \cdot F \text{ (tangent)} \tag{36}$$

(b) Shadow side

$$\overline{E} = \frac{1}{2}\sqrt{\frac{d\psi_0}{d\psi}}\left[\frac{\rho_g(Q)}{\rho_g(Q')}\right]^{1/6}\left\{\hat{n}\left[\sin(\alpha_s - \beta)\, g^*(\xi)\right]\right.$$

$$\left. + \hat{b}\left[\frac{\rho_g(Q')}{\rho_\tau(Q')}\left(-j\left[\frac{2}{k\rho_g(Q')}\right]^{1/3}\right)\sin\alpha_s\,\sin\beta\tilde{g}^*(\xi)\right.\right.$$

$$\cdot\, e^{-jk\ell}\cdot F\,(\text{tangent}) \tag{37}$$

(3) Deep Shadow Region

$$\overline{E} = \frac{1}{2}\left[\sum_j\,\hat{n}_j\,\sin(\alpha_s - \beta)\,E_j^h + \hat{b}_j\,\frac{\rho_g(Q')}{\rho_\tau(Q')}\cdot\sin\alpha_s\,\sin\beta\,E_j^s\right]$$

$$\cdot\, F_j\,(\text{tangent}) \tag{38}$$

where

$$E^h = \sqrt{\frac{d\psi_0}{d\psi}}\sum_{m=0}^{1}\,D_m^h\,L_m^h\,e^{-\int\gamma_m^h(\ell)d\ell}$$

$$E^s = \sqrt{\frac{d\psi_0}{d\psi}}\sum_{m=0}^{1}\,D_m^s\,L_m^s\,e^{-\int\gamma_m^s(\ell)d\ell}$$

$$\text{sgn} = \frac{\hat{t}'\cdot(\hat{n}'\times\hat{z}')}{|\hat{t}'\cdot(\hat{n}'\times\hat{z}')|}$$

$$\xi = \mp\left|\int_{Q'}^{Q}\left(\frac{k}{2\,\rho_g^2(\ell)}\right)^{1/3}d\ell\right|\quad\text{for}\begin{cases}\text{illuminated side}\\\text{shadow side}\end{cases}$$

$g^*(\cdot),\tilde{g}^*(\cdot)$ complex conjugates of the Fock functions [48]

24

$\hat{n}',\hat{b}',\hat{t}',\hat{n},\hat{b},\hat{t}$ normal, binormal, and tangent unit vectors to the surface, at source point Q' and diffraction point Q, respectively.

$F(\cdot)$ phase factor required to refer the phase of a ray to the center of the coordinate system

$\sqrt{d\psi_0/d\psi}$ spread factor and equals unity for this case [48]

ρ_g,ρ_τ longitudinal and transverse radii of curvature

$\hat{z}',\hat{\tau}'$ unit vectors in the principal directions in which the geodesics have no torsion

$\hat{s}_0$ unit vector pointed from the source to the observation point

s_0 the distance from the source to the observation point

Note that the superscripts h and s indicate the hard and soft boundary conditions, respectively.

The launching coefficients are given by [48]

$$L_m^h = \left[\pi e^{j(\pi/12)}\ D_m^h\ \left(\frac{2}{k\rho_g}\right)^{1/3} A_i'(-\overline{q}_m)\right] \text{ at the source } Q'$$

$$L_m^s = \left[\pi e^{-j(\pi/12)}\ D_m^s\left(\frac{2}{k\rho_g}\right)^{2/3} A_i(-q_m)\right] \text{ at the source } Q'$$

where D_m is defined in Table 1. The subscript m refers to the mth mode of the boundary layer surface wave. Thus, γ_m is the propagation constant for the mth mode surface wave such that $\gamma_m = \alpha_m + jk$, where α_m is defined in Table I. The quantity q_m is the root of Miller-type Airy function $A_i(-q_m)$, that is, $A_i(-q_m)=0$. Similarly $\overline{q}_m$ is the root of $A_i'(-\overline{q}_m)$, the derivative of $A_i(-q_m)$ with respect to the argument of the Airy function.

The incremental arc length along the geodesic path is expressed by $d\ell$. The summation over j in the shadow region indicates that several terms can contribute in that region. It is noted that for a slot oriented at 45° with respect to the z-axis, Eqs. (36) to (38) are not sufficiently accurate for calculating the radiation pattern as a function of ϕ where $\theta = 45°$. For this special case and for cases sufficiently close to it, an additional correction term $\overline{E}_c$ should be included as indicated in Reference [50,51].

One must first find an efficient solution for the geodesic paths on the elliptic cylinder surface in order to analyze this problem successfully using GTD. A preferred coordinate system for the elliptic cylinder is illustrated in Fig. 6 and defined by

$$x = d \cosh u \cos v = a_f \cos v$$

$$y = d \sinh u \sin v = b_f \sin v \qquad (39)$$

$$z = z$$

where 2d is the distance between the foci of the ellipse. Note that for $u = u_f$, where $u_f = \tanh^{-1}(b_f/a_f)$, the preceding equations define an elliptical surface. Thus, any point on the elliptical surface is expressed by v, which varies from 0 to 2π.

Using the calculus of variations, the z-coordinate of the geodesic paths on an elliptical surface are given by

$$z(v) = \frac{C}{\sqrt{1 - C^2}} \int_{v_i}^{v_f} \sqrt{a_f^2 \sin^2 v + b_f^2 \cos^2 v} \; dv + z(v_i)$$

$$(40)$$

Note that v_i and v_f are, respectively, the initial and final values of v along a given geodesic path. If one defines the geodesic starting direction by the angle (α_s) as shown in Fig. 5, then $C = -\cos \alpha_s$. The advantage of this geodesic solution lies in the fact that the integral can be quickly evaluated using numerical techniques. The important parameters of this problem are listed below:
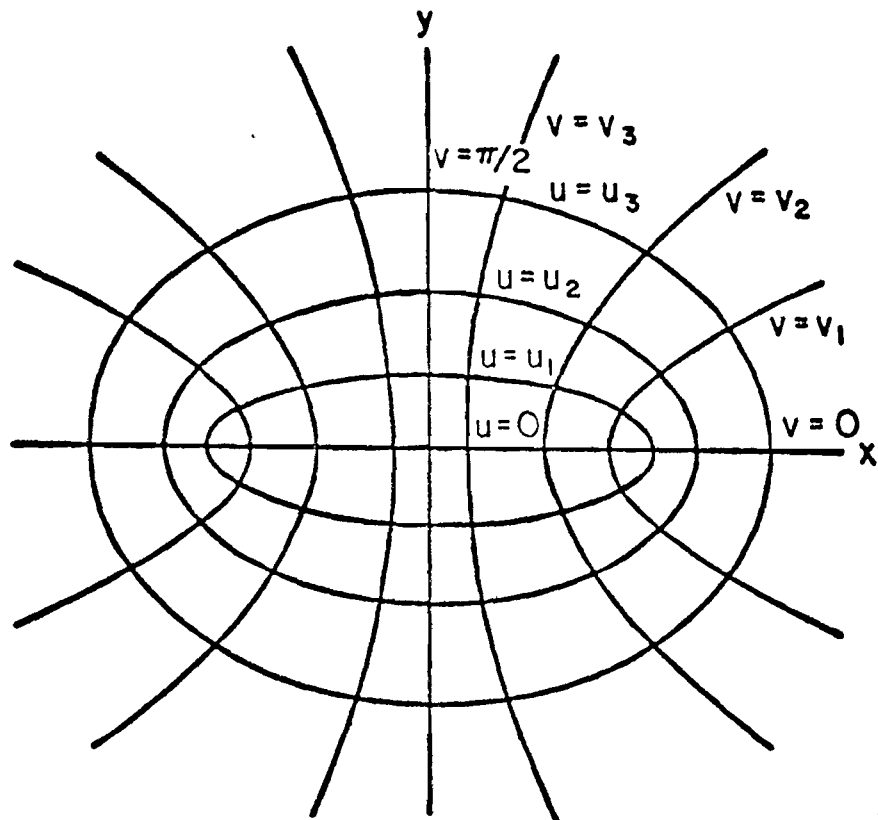
Figure 6. Diagram showing the elliptic cylinder coordinate system.

$$z = \frac{-\cos \alpha_s}{|\sin \alpha_s|} \int_{v_i}^{v_f} \sqrt{a_f^2 \sin^2 v + b_f^2 \cos^2 v} \;\; dv$$

(geodesic equation)

$$\ell = \frac{1}{|\sin \alpha_s|} \int_{v_i}^{v_f} \sqrt{a_f^2 \sin^2 v + b_f^2 \cos^2 v} \;\; dv$$

(arc length)

$$\hat{e}_1 = \frac{-a_f \sin v\hat{x} + b_f \cos v\hat{y}}{\sqrt{a_f^2 \sin^2 v + b_f^2 \cos^2 v}}$$

(curvalinear coordinates)

$$\hat{e}_2 = \hat{z}$$

$$\hat{t} = \sin \alpha_s \hat{e}_1 - \cos \alpha_s \hat{e}_2 \qquad \text{(unit tangent vector)}$$

$$\hat{n} = \frac{b_f \cos v\hat{x} + a_f \sin v\hat{y}}{\sqrt{a_f^2 \sin^2 v + b_f^2 \cos^2 v}} \qquad \text{(unit normal vector)}$$

$$\hat{b} = \hat{t} \times \hat{n} = -\cos \alpha_s \hat{e}_1 - \sin \alpha_s \hat{e}_2$$

(unit binormal vector)

$$\rho_g = \frac{(a_f^2 \sin^2 v + b_f^2 \cos^2 v)^{3/2}}{a_f b_f \sin^2 \alpha_s}$$

(longitudinal radius of curvature).

Using the preceding relations, one can employ (31)-(38) to determine the total radiated fields in the whole space except for two small sectors around the cylinder axis where α_s is near 0 or π, since the solution fails in these regions.

4.   NEAR FIELD SCATTERING BY A FINITE BENT PLATE

The near field scattering by a finite bent plate is a relatively new topic at higher frequencies where the plate is large in terms of the wavelength. The solution presented here is a practical application of the three-dimensional wedge diffraction theory given earlier. The source is defined by its location and far-field pattern. The far-field pattern of the source is appropriate in that the plate is located at least $2D^2/\lambda$ away from the source where D is the maximum dimension of the source. The finite plate is simply specified by location of its n corners. The junction edge is defined by the first corner specified plus an additional corner (MC) defined as input to the computer program. The plate is initially flat ($\alpha = 180°$ in

Fig. 7). It can then be bent about the line joining corner #1
and MC such that $90° \leq \alpha \leq 270°$.
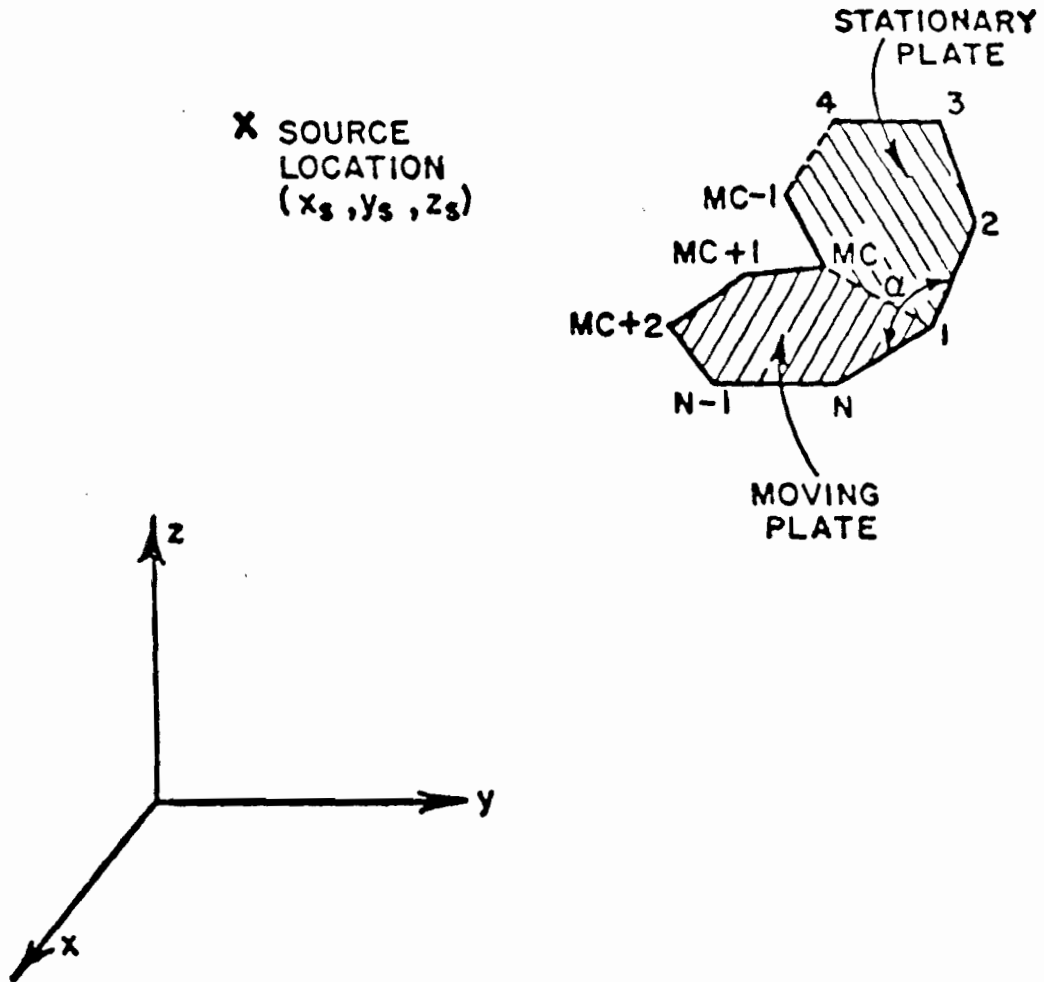
Figure 7. Bent plate geometry.

It is known that for a given scatter direction there is only
one point along an infinitely long straight edge at which the
diffracted field can emanate for a near zone source. Thus, this
point must be found for each of the n edges that describe the

finite plate. There are many ways of finding this diffraction point, one of which is described here. Since it is known that $\beta_0 = \beta_0'$ (see Fig. 1), it is obvious that

$$\hat{e}_m \cdot \hat{I} = \hat{e}_m \cdot \hat{d} \tag{41}$$

where $\hat{e}_m$, $\hat{I}$, and $\hat{d}$ are, respectively, the mth edge unit vector, incident direction unit vector, and diffraction direction unit vector. Since the scatter direction is known (θ_s, ϕ_s), the value of $\hat{e}_m \cdot \hat{d} = c_m$ is easily computed at each edge. One needs only search along the edge to find the point where $\hat{e}_m \cdot \hat{I} = c_m$.

Once the diffraction point is located, one must find the diffracted field value from the mth edge. The far field pattern of the source can be written as

$$\vec{E}_s(\theta,\phi) = [\hat{\theta}\, F(\theta,\phi) + \hat{\phi} G(\theta,\phi)] \frac{e^{-jks'}}{s'} = \vec{R}(\theta,\phi) \frac{e^{-jks'}}{s'} \tag{42}$$

where s' is the range from the source to the field point. Using the geometry illustrated in Fig. 7 and applying the results presented earlier, one finds that

$$
\begin{bmatrix} R_{\shortparallel}^d \\[1em] R_{\perp}^d \end{bmatrix}
=
\begin{bmatrix} -V_B^- & 0 \\[1em] 0 & -V_B^+ \end{bmatrix}
\begin{bmatrix} R_{\shortparallel}^i \\[1em] R_{\perp}^i \end{bmatrix}
e^{-j[k(s' - \gamma) - k_\rho \rho]} \tag{43}
$$

where

$$R_{\shortparallel}^i = \vec{R}(\theta_i, \phi_i) \cdot \hat{\beta}_0'$$

$$R_{\perp}^i = \vec{R}(\theta_i, \phi_i) \cdot \hat{\phi}_0$$

$$k_\rho \rho = ks' \sin^2 \beta_0$$

$$\gamma = x_{dp} \sin \theta_s \cos \phi_s + y_{dp} \sin \theta_s \sin \phi_s + z_{dp} \cos \theta_s$$

$$V_B^{\mp} = V_B(k_\rho \rho/k, \phi-\phi', 2) \mp V_B(k_\rho \rho/k, \phi+\phi', 2)$$

$$\hat{\phi}_0 = \hat{I} \times \hat{\beta}_0'$$

30

The coordinates (x_{dp}, y_{dp}, z_{dp}) define the point of diffraction.

Once these terms are determined, the total diffracted field in ray form from a general m^{th} edge is given by

$$\vec{R}_m^d(\theta_s, \phi_s) = R_{\shortparallel}^d \hat{\beta}_0 + R_{\perp}^d \hat{\phi} \qquad (44)$$

where $\hat{\phi} = \hat{d} \times \hat{\beta}_0$. Using the superposition principle, the total singly diffracted field in ray form by the n edges of the plate is given using Eq. (44) by

$$\vec{R}^d(\theta_s, \phi_s) = \sum_{m=1}^{n} \vec{R}_m^d(\theta_s, \phi_s) \qquad (45)$$

The first step in calculating the reflected field is to find the locations of the image sources, which are uniquely determined once the planes of the flat plates are defined relative to the source location. In fact, the image is located along lines which are orthogonal to the different portions of the plate and positioned an equal distance on the opposite side of the plate.

With the image position known, one needs to determine if the reflected field contributes to the total scattered field using the geometrical optics approach. If the reflected field is a contributor, the ray from the image source in the scatter direction (θ_s, ϕ_s) must pass through the finite plate limits. Thus, one must find the location of the intersection point of this ray and the plane containing the flat plate. This can easily be accomplished using vector analysis. One can, then, predict within certain limits whether this intersection point falls within the bounds of the finite flat plate.

If reflections do occur, the reflected field from the image source can be written in ray form as

$$\vec{R}^r(\theta_s, \phi_s) = [\hat{\theta}^r F^r(\theta_s, \phi_s) + \hat{\phi}^r G^r(\theta_s, \phi_s)]$$
$$\cdot e^{jk[x_i \sin \theta_s \cos \phi_s + y_i \sin \theta_s \sin \phi_s + z_i \cos \theta_s]}$$
$$\qquad (46)$$

where $\hat{\theta}^r$ and $\hat{\phi}^r$ are related to the image source coordinate system with the image location defined by (x_i, y_i, z_i). The functions

31

$[F^r(\theta_s, \phi_s)$ and $G^r(\theta_s, \phi_s)]$ are found by employing the boundary conditions on the perfectly conducting flat plate. The total scattered field from the flat plate is, then, given by

$$\vec{R}^s(\theta_s, \phi_s) = \vec{R}^d(\theta_s, \phi_s) + \vec{R}^r(\theta_s, \phi_s) \tag{47}$$

The four basic terms included in the present solution are as follows:

(a) single diffraction of incident field as shown in Fig. 8(a)

(b) single reflection of incident field as shown in Fig. 8(b)

(c) double reflection of incident field as shown in Fig. 8(c)

(d) single diffraction of reflected field as shown in Fig. 8(d).

Each of the terms has been illustrated in a two-dimensional view just for simplicity in illustrating the mechanisms· whereas, the actual solution is for the three-dimensional geometry. These terms have all been incorporated in a general bent plate solution. Note that only those terms are included which are not shadowed by another portion of the bent plate.

The accuracy of this solution is illustrated by the example shown in Fig. 9 where it compares very favorably with measured results taken for a $\lambda/2$ dipole illuminating a flat plate. This solution is also compared with results obtained using a moment method patch technique [50] as illustrated in Figs. 10 and 11. Note that for these comparisons the plate dimensions are quite small in terms of the wavelength, which accounts for the small discrepancies in the patterns between the two solutions. This structure will be incorporated into the aircraft model of Section III in order to account for bent wings, moving flaps, **vertical stabilizer**, etc.

32
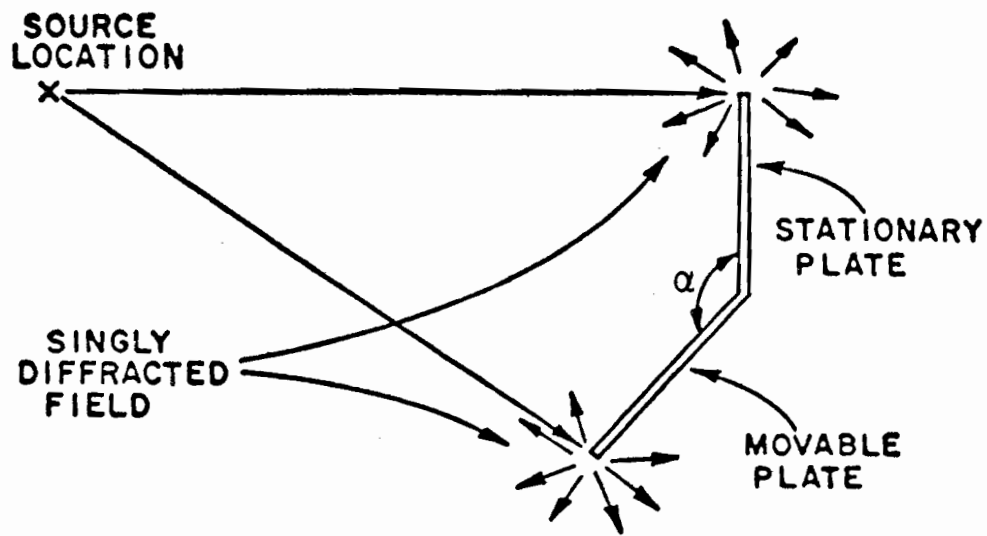
Figure 8a. Single diffraction of incident field.
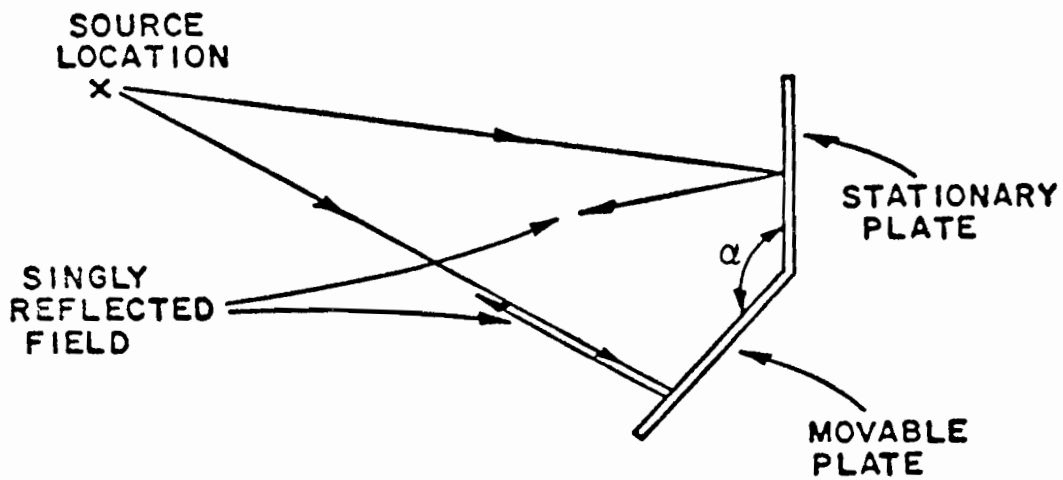
Figure 8b. Single reflection of incident field.

SOURCE
LOCATION
X

DOUBLY
REFLECTED
FIELD

STATIONARY
PLATE

α

MOVABLE
PLATE
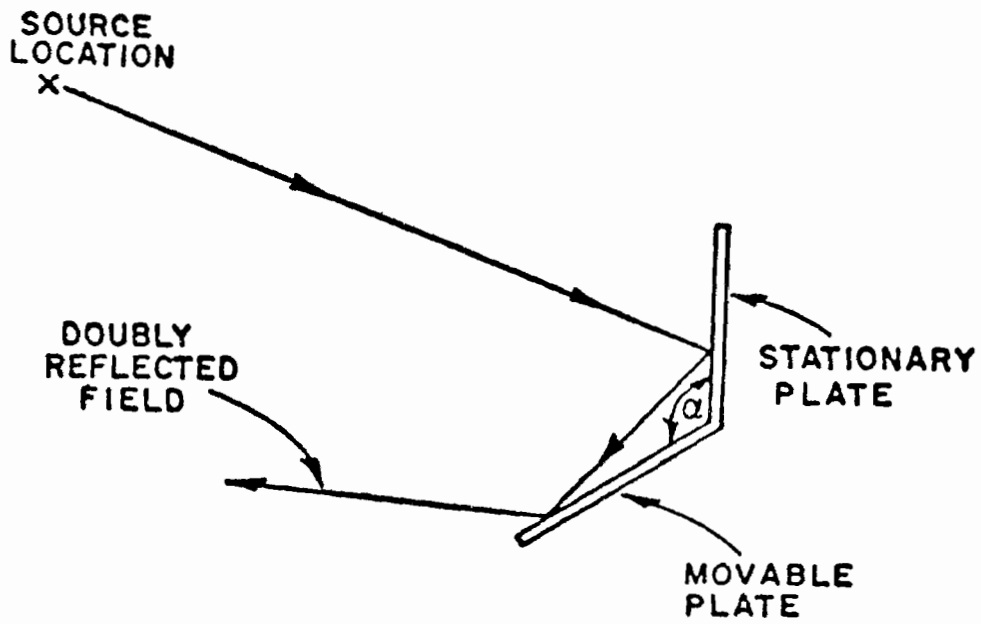
Figure 8c.   Double reflection of incident field.

SOURCE
LOCATION
X

SINGLY
DIFFRACTED
REFLECTED
FIELD

STATIONARY
PLATE

α

MOVABLE
PLATE
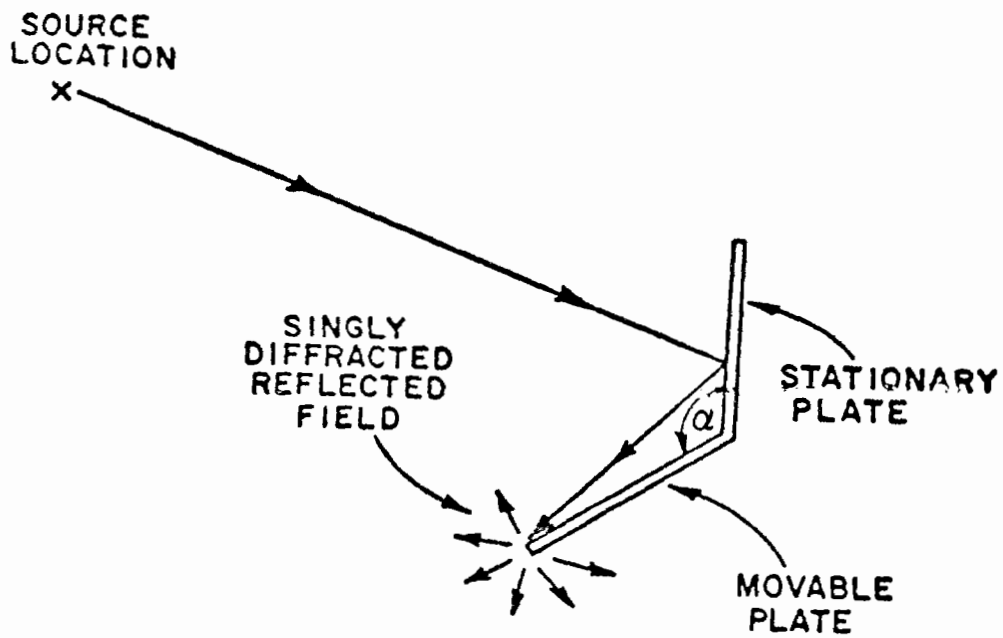
Figure 8d. Single diffraction of reflected field.
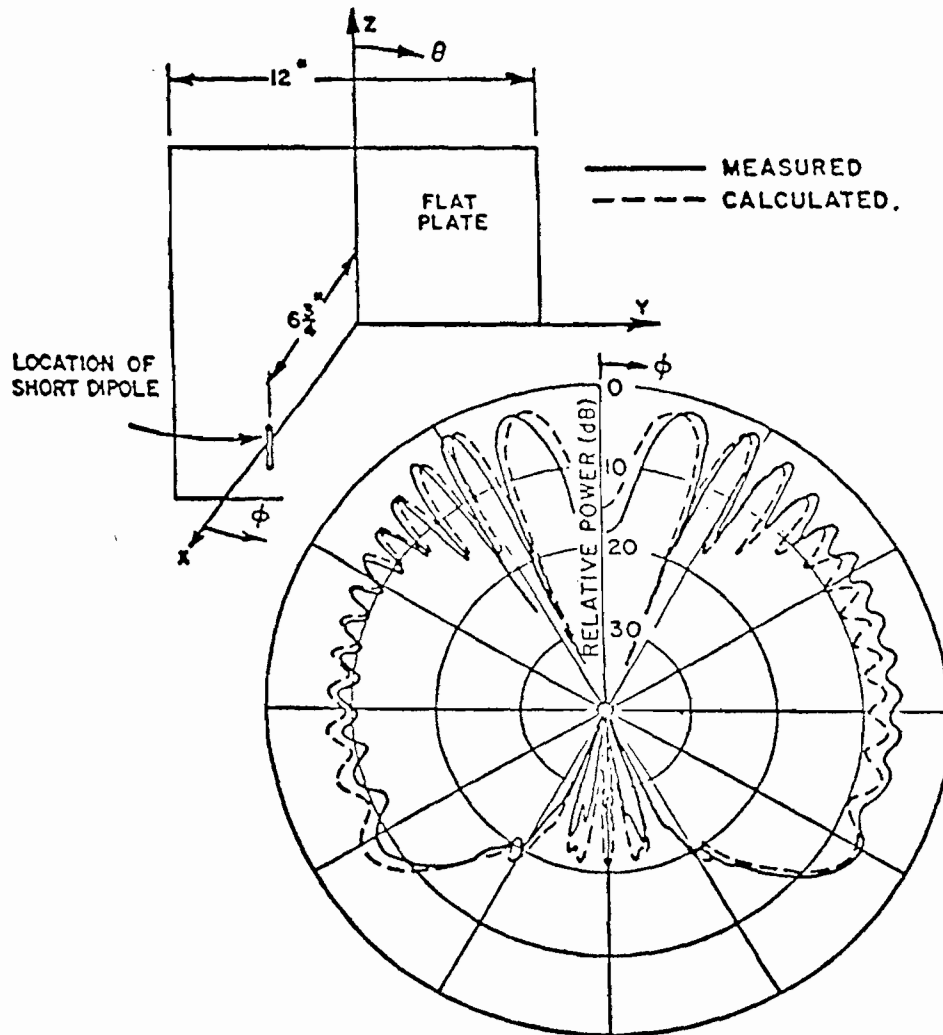
Figure 9. E_θ radiation pattern for a small dipole mounted above a square plate for $\theta = 90°$ and $0 \stackrel{\le}{} \phi \stackrel{\le}{} 360°$ at f = 10.436 GHz.
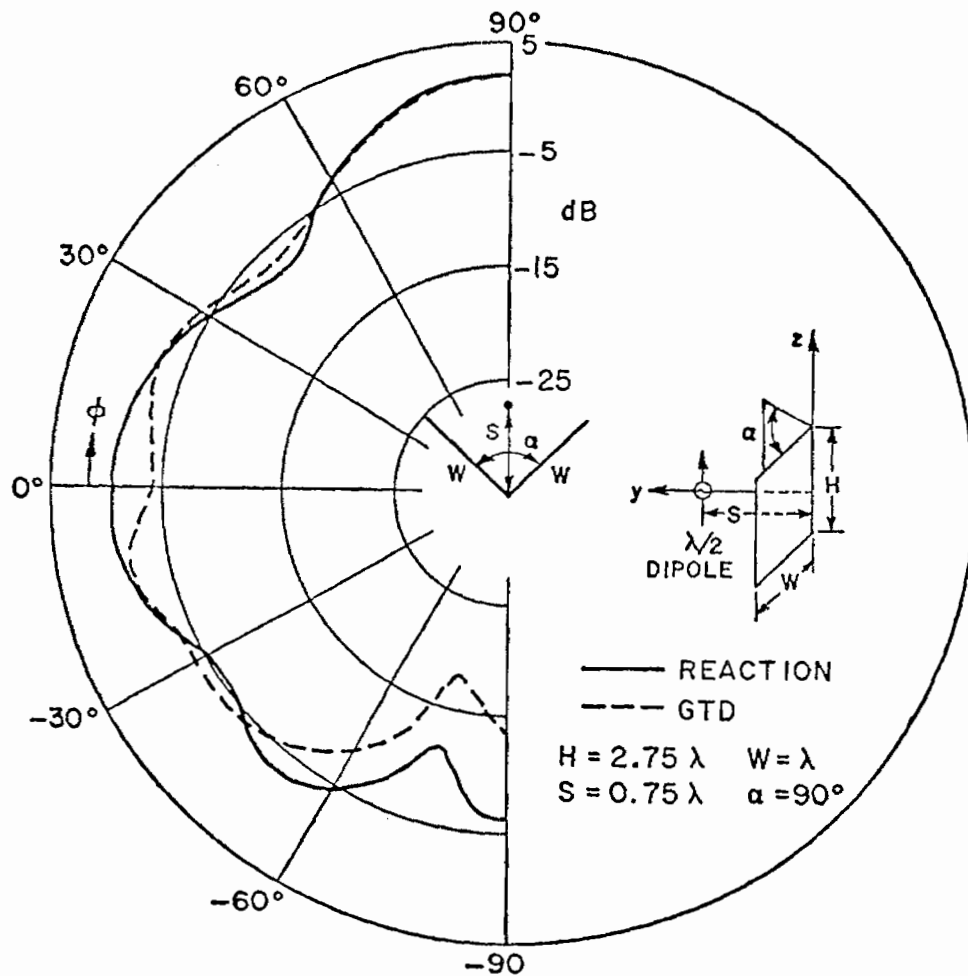
Figure 10a. H-plane pattern.
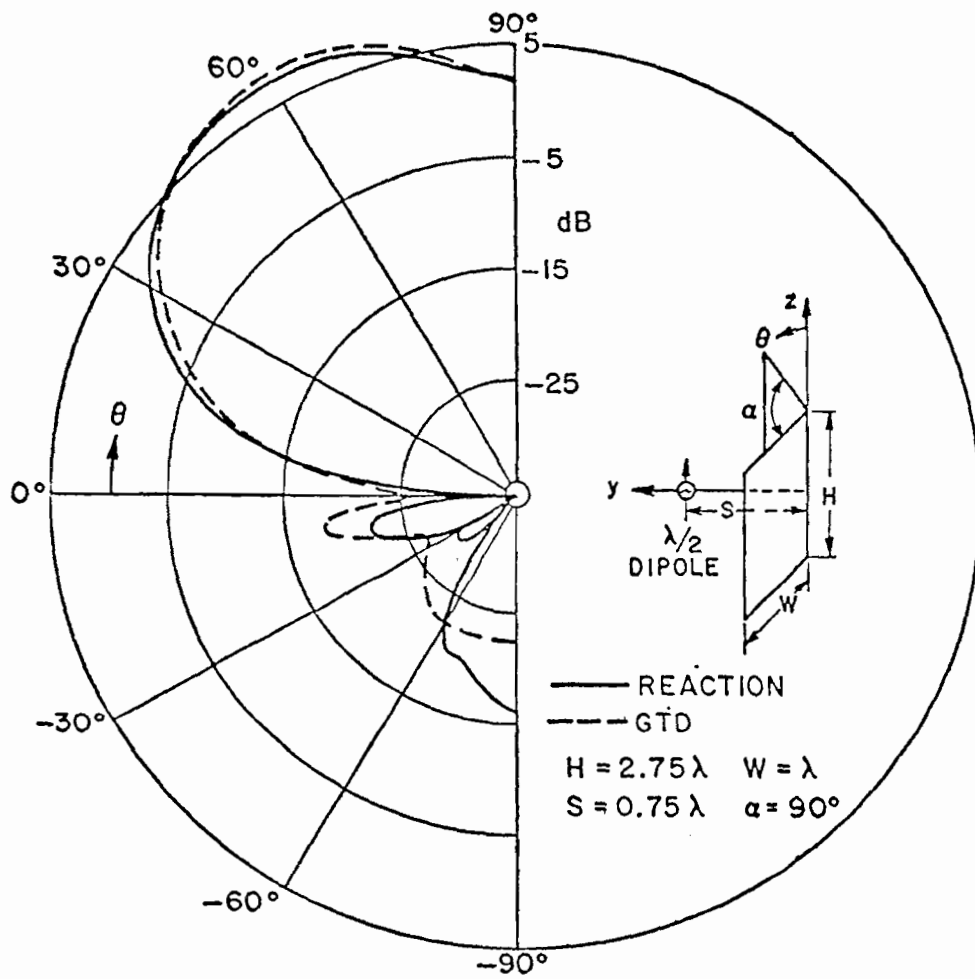
Figure 10b. E-plane pattern.
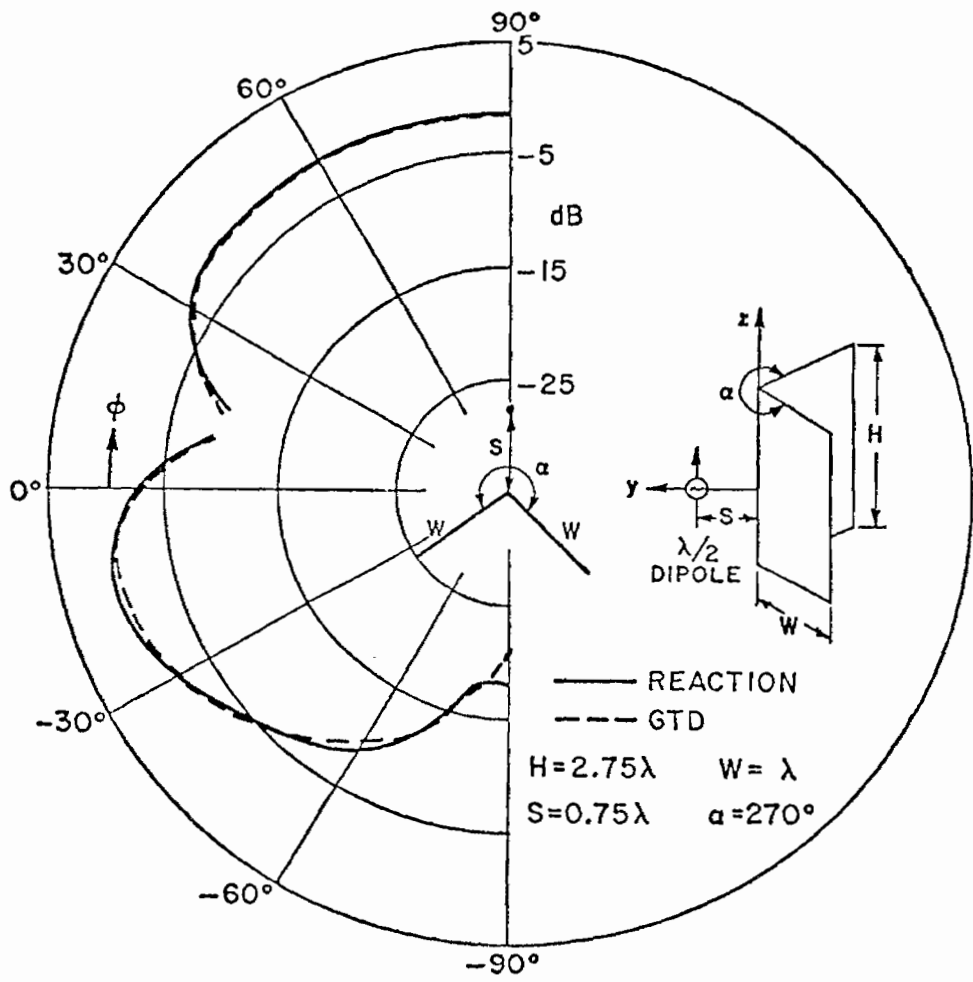
Figure 11a. H-plane pattern.
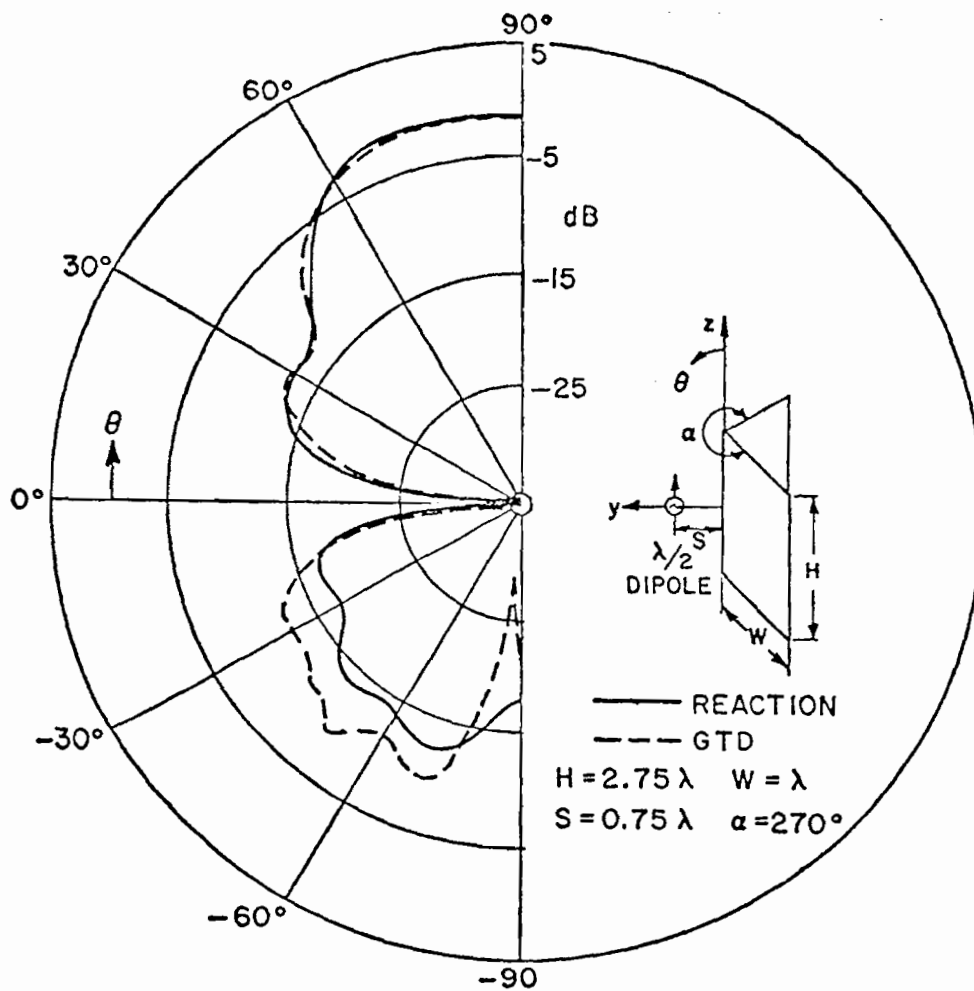
Figure 11b. E-plane pattern.

SECTION III
MATHEMATICAL MODELING OF AIRCRAFT
FOR PATTERN COMPUTATIONS

In this section, the mathematical modeling of an antenna
on an aircraft is described. This mathematical model is intended
to be as simple as possible so that it can be used to simulate a
wide variety of aircraft structures, yet accurate enough that the
computed radiation patterns are comparable to measured results.
The model is systematically increased in complexity to resolve
discrepancies between calculated and measured results, yet basic
simplicity is retained. One of the restrictions in the model is
that the antenna under consideration is located near the top or
bottom of the fuselage surface.

This section begins with a brief review of the analyses
using the elevation plane model and the roll plane model. This
is followed by solutions for the volumetric patterns of antennas
on a three-dimensional aircraft structure.   The approach used to
model the aircraft by two elliptic cylinders is explained in detail.
The numerical technique to generate the necessary elliptic cylinders
is also discussed. Finally, the radiation patterns in principal
planes for various cases are calculated to illustrate the versa-
tility of the newly developed solutions.

1.   ANALYSIS OF ELEVATION PLANE MODEL

In most cases, the dominant structural effect in the
elevation plane is the profile of the aircraft for fuselage
mounted antennas. An aircraft fuselage is usually a convex
body that cannot be completely described by simple mathematical
equations. Hence, in practice, an aircraft shape is often
specified by points. Consequently, a method called "section
matching method" has been developed [28] to handle the problem of
an antenna mounted on a fuselage surface of general shape.
However, this method is restricted to principal plane pattern
calculations. For off-principal plane pattern calculations
the method is hard to apply, since a complete three-dimensional
description of the fuselage surface is difficult to obtain.
Furthermore, the lack of information on the geodesic paths and
torsion effect of the curved surface create serious problems in
the prediction of antenna patterns. Consequently, a simple
model which simulates a general fuselage profile has been adopted.

Since an aircraft fuselage is usually long and slender, a
composite elliptic cylinder appears to be a good model. This
model consists of two semi-elliptic cylinders mounted back-to-
back as shown in Fig. 12. Note that as discussed in the last
chapter, the model employed here is not limited to the determi-
nation of the elevation plane pattern only. It can be used to
determine off-elevation plane radiation patterns also.

Recall that the solutions presented in the last section are
based on elliptic cylinder models; however, one of the advantages
of GTD is that it can be extended to new structures after making
certain assumptions. In this case, it is assumed that there are no
diffractions from the junction lines of the two ellipses. This
assumption is justified since these junctions are non-existent in the
actual aircraft profile. Note that the GTD solution in the illuminated
region does not depend on the surface parameters in that it is
assumed the source is mounted on an infinite ground plane tangent
to the surface at the source point. On the other hand, the transition
and deep-shadow region solutions are modified due to their dependence
upon the surface parameters. This modification requires that one
use $b_f = b'$ for rays traveling to the right of the junction and
$b_f = b$ for rays traveling to the left of the junction. The parameters
b and b' are illustrated in Fig. 12.
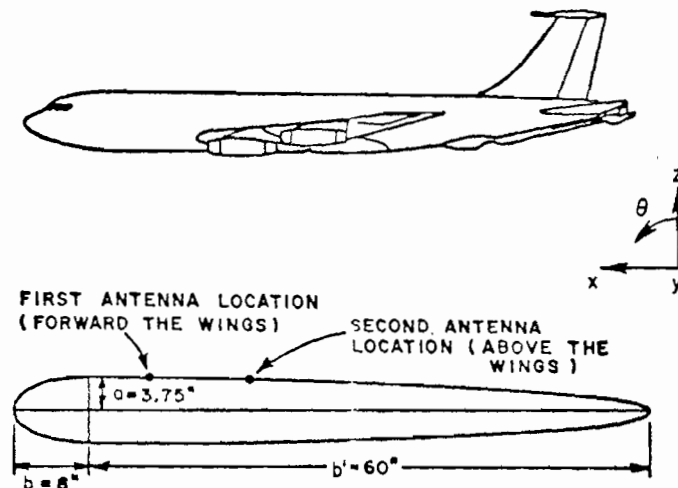
Figure 12. Theoretical model of KC-135 aircraft.

Since the model employed is a composite elliptic cylinder, the surface curvature at the junction line is not continuous due to the different dimensions of the elliptic cylinders. To ensure the assumption made earlier that no diffraction occurs from the junction line, the solution presented in paragraph 3 of Section II needs to be modified to correct for the difference in curvature when the surface wave crosses the junction line. Since no GTD solution for this problem is available at present, an alternate way to account for the continuity of the surface wave crossing the junction line is necessary. It is noted that due to the large radius of curvature at the junction line in our model the reflection effect is so weak that it can be neglected. A way to treat the continuity of the surface wave across the junction is investigated next.

Consider a source located on a composite elliptic cylinder as shown in Fig. 13. The field diffracted by a curved surface can be written, according to Eq. (34) for hard boundary conditions and with only the first mode retained, as

$$E = CL(Q') \, D(Q) \, e^{-\int_{Q'}^{Q} (\alpha + jk) \, ds} \tag{48}$$

where C is a complex constant. This result indicates that the field diffracted from the curved surface is related only to the launching coefficient at the source point and the diffraction coefficient at the diffraction point. Thus, when the diffraction point is on the right half elliptic cylinder, the field is given by

$$E = C \, L(a,b) \, D_2(a,b') \, e^{-\int_{Q'}^{Q} (\alpha + jk) \, ds} \tag{49}$$

note that a and b are the semiminor and semimajor axes of the left half ellipse and a and b' are the semiminor and semimajor axes of the right half ellipse, respectively. Similarly, the field diffracted from point Q on the left half ellipse is expressed as

$$E = C \, L(a,b) \, D_1(a,b) \, e^{-\int_{Q'}^{Q} (\alpha + jk) \, ds} \tag{50}$$
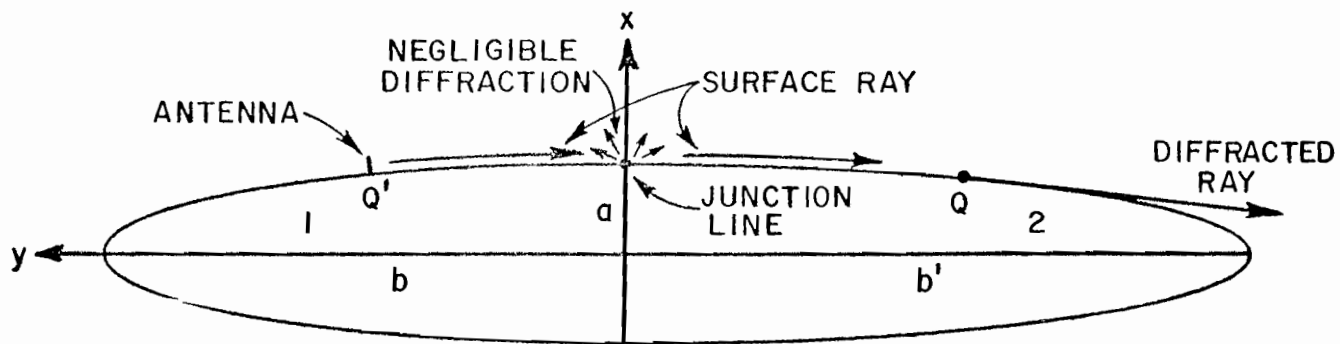
Figure 13. Illustration of surface waves propagating across the junction line of a composite elliptic cylinder.

At the junction, Eqs. (49) and (50) become

$$E_J = C \ L(a,b) \ D_{2J}(a,b') \ e^{- \int_{Q'}^{J} (\alpha + jk) \ ds} \qquad (51)$$

and

$$E_J = C \ L(a,b) \ D_{1J}(a,b) \ e^{- \int_{Q'}^{J} (\alpha + jk) \ ds} \qquad (52)$$

respectively, where the subscript J denotes the junction.

It is noted that Eqs. (51) and (52) do not agree with each other which indicates a discontinuity exists in the diffracted field. However, this is not true in practice, since the field must be continuous as the diffraction point crosses the junction. Comparing Eqs. (51) and (52), one notes that if a modification factor

$$\left[\frac{D_{1J}(a,b)}{D_{2J}(a,b')} \right]$$

is introduced, the field is continuous as the diffraction point crosses the junction. Thus, Eq. (48) is modified to give

$$E = C \ \frac{D_{1J}(a,b)}{D_{2J}(a,b')} \ L(a,b) \ D_2(a,b') \ e^{- \int_{Q'}^{Q} (\alpha + jk) \ ds} \qquad (53)$$

Notice that Eq. (53) is valid only for the surface wave which crosses the junction, i.e., the diffraction point and source point occur on different elliptic cylinders.

From Table I, one sees that the factor introduced in Eq. (53) can be simplified to give

$$\frac{D_{1J}(a,b)}{D_{2J}(a,b')} = \left[\frac{\rho \ g_J(a,b)}{\rho \ g_J(a,b')} \right]^{1/6} = \left[\frac{b}{b'} \right]^{1/3} \qquad (54)$$

which depends only upon the ratio of the two

44

TABLE I

GENERALIZED DIFFRACTION COEFFICIENTS AND ATTENUATION CONSTANTS

Surface	SQUARE OF DIFFRACTION COEFFICIENT $D_p^2 =$ (Column A) · (Column B)		ATTENUATION CONSTANT $\alpha_p =$ (Column C) · (Column D)		ZEROES OF THE AIRY FUNCTION
	A. Keller's Result	B. Correction Terms	C. Keller's Result	D. Correction Terms	
Soft Acoustic and Soft EM	$\dfrac{\pi^{-1/2} 2^{-5/6} \rho_g^{1/3} e^{-j\pi/12}}{k^{1/6}(Ai'(-q_p))^2}$	$1 + \left(\dfrac{2}{k\rho_g}\right)^{2/3} q_p\left(\dfrac{1}{30} + \dfrac{\rho_g}{4\rho_{tn}} + \cdots\right)e^{-j\pi/3}$	$\dfrac{q_p}{\rho_g} e^{j\pi/6}\left(\dfrac{k\rho_g}{2}\right)^{1/3}$	$1 + \left(\dfrac{2}{k\rho_g}\right)^{2/3} q_p\left(\dfrac{1}{60} - \dfrac{2}{45}\rho_g\ddot{\rho}_g + \dfrac{4}{135}\dot{\rho}_g^{\,2}\right)e^{-j\pi/3}$	$Ai(-q_p) = 0$ $q_1 = 2.33811$ $q_2 = 4.08795$ $Ai'(-q_1) = .70121$ $Ai'(-q_2) = -.80311$
Hard Acoustic		$1 + \left(\dfrac{2}{k\rho_g}\right)^{2/3}\left(\bar{q}_p\left(\dfrac{1}{30} + \dfrac{\rho_g}{4\rho_{tn}} + \cdots\right) - \dfrac{1}{\bar{q}_p^{\,2}}\left(\dfrac{1}{10} + \dfrac{\rho_g}{4\rho_{tn}} + \cdots\right)\right)e^{-j\pi/3}$	$\dfrac{\bar{q}_p}{\rho_g} e^{j\pi/6}\left(\dfrac{k\rho_g}{2}\right)^{1/3}$	$1 + \left(\dfrac{2}{k\rho_g}\right)^{2/3}\left(\bar{q}_p\left(\dfrac{1}{60} - \dfrac{2}{45}\rho_g\ddot{\rho}_g + \dfrac{4}{135}\dot{\rho}_g^{\,2}\right) + \dfrac{1}{\bar{q}_p^{\,2}}\left(\dfrac{1}{10} + \dfrac{\rho_g}{4\rho_{tn}} + \dfrac{\dot{\rho}_g^{\,2}}{90}\right)\right)e^{-j\pi/3}$	ZEROES OF THE DERIVATIVE OF THE AIRY FUNCTION $Ai'(-\bar{q}_p) = 0$ $\bar{q}_1 = 1.01879$ $\bar{q}_2 = 3.24820$ $Ai(-\bar{q}_1) = .53566$ $Ai(-\bar{q}_2) = -.41902$
Hard EM	$\dfrac{\pi^{-1/2} 2^{-5/6} \rho_g^{1/3} e^{-j\pi/12}}{k^{1/6}\, \bar{q}_p (Ai(-\bar{q}_p))^2}$	$1 + \left(\dfrac{2}{k\rho_g}\right)^{2/3}\left(\bar{q}_p\left(\dfrac{1}{30} + \dfrac{\rho_g}{4\rho_{tn}} + \cdots\right) - \dfrac{1}{\bar{q}_p^{\,2}}\left(\dfrac{1}{10} - \dfrac{\rho_g}{4\rho_{tn}} + \cdots\right)\right)e^{-j\pi/3}$		$1 + \left(\dfrac{2}{k\rho_g}\right)^{2/3}\left(\bar{q}_p\left(\dfrac{1}{60} - \dfrac{2}{45}\rho_g\ddot{\rho}_g + \dfrac{4}{135}\dot{\rho}_g^{\,2}\right) + \dfrac{1}{\bar{q}_p^{\,2}}\left(\dfrac{1}{10} - \dfrac{\rho_g}{4\rho_{tn}} - \dfrac{\rho_g\ddot{\rho}_g}{60} + \dfrac{\dot{\rho}_g^{\,2}}{90}\right)\right)e^{-j\pi/3}$	

ρ_g = radius of curvature along the geodesic
ρ_{tn} = radius of curvature perpendicular to the geodesic (transverse curve)
Dots indicate differentiation with respect to the arc length variable
The Miller-type Airy function[11] appearing in Column A is given by:

$$Ai(-x) = \frac{1}{\pi}\int_0^\infty \cos\left(\frac{t^3}{3} - xt\right) dt.$$

$Ai'(-x)$ denotes the derivative of $Ai(-x)$ with respect to the argument of the Airy function.

of the composite ellipse. For a continuous elliptic cylinder,
this factor reduces to unity as expected. Note that Eq. (53)
can be generalized to describe the field diffracted from an
arbitrary point on the curved surface as

$$E = C \ L(Q') \ D(Q) \ p \ e^{-\int_{Q'}^{Q} (\alpha + jk) \ ds} \tag{55}$$

where

$$p = \begin{cases} 1 & \text{if Q and Q' are on same elliptic cylinder} \\ \left[\dfrac{^{\rho}g_J(\text{ellipse with source})}{^{\rho}g_J(\text{ellipse without source})} \right]^{1/6} & \text{otherwise.} \end{cases} \tag{56}$$

In a similar manner, this factor can be determined through
the field expression in the transition region as presented in
Chapter II and is found to be the same as Eq. (56).

To illustrate the newly modified solution, the elevation
plane radiation patterns for antennas mounted on the KC-135 air-
craft are now analyzed. Since the antennas of interest are located
on top of the fuselage and along the center line, the most significant
effects on the pattern result from the upper surface of the
fuselage profile. The structure used to simulate the 1/25th
scale model consists of a 3.75" by 60" right semi-elliptic cylinder
and an 3.75" by 8" left semielliptic cylinder as shown in Fig. 12.
Using Eqs. (31) to (38) in Section II with the modifications just
described, the radiation patterns in the elevation plane for
antennas mounted on our model can be easily determined.

The elevation plane patterns for a $\lambda/4$ monopole mounted
forward and over the wings are illustrated in Fig. 14 (a) and (b),
respectively. The patterns for a circumferential KA-band wave-
guide are illustrated in Figs. 15 (a) and (b). Finally, the
results for an axial KA-band waveguide are shown in Fig. 16 (a)
and (b). The KA-band waveguide aperture fields are simulated in
our model by an array of infinitesimal elements as shown in Fig.
17.

46
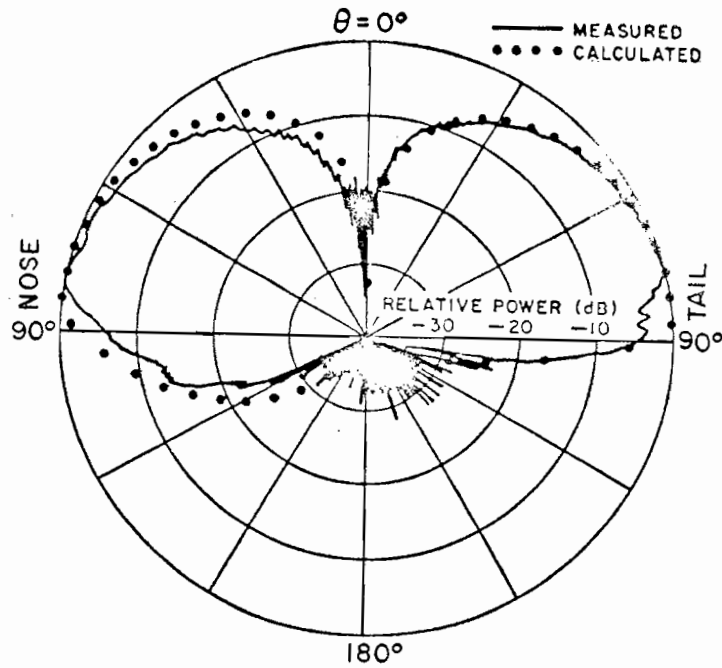
Figure 14a. Elevation plane pattern for a λ/4 monopole mounted forward of the wings on a KC-135 aircraft. (No radome and vertical stabilizer included).
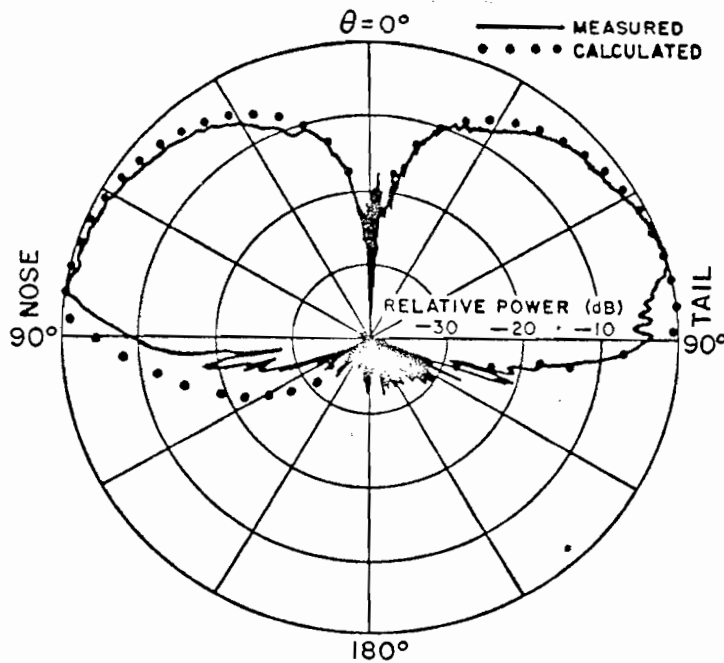
Figure 14b. Elevation plane pattern for a λ/4 monopole mounted above the wings on a KC-135 aircraft. (No radome and vertical stabilizer included).
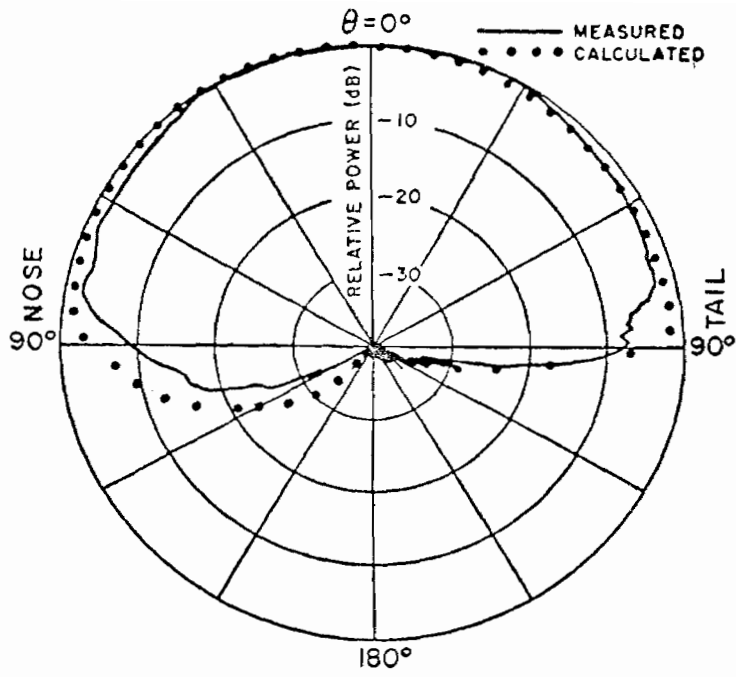
Figure 15a. Elevation plane pattern for a circumferential KA-band
waveguide mounted forward of the wings on a KC-135
aircraft. (No radome and vertical stabilizer included).
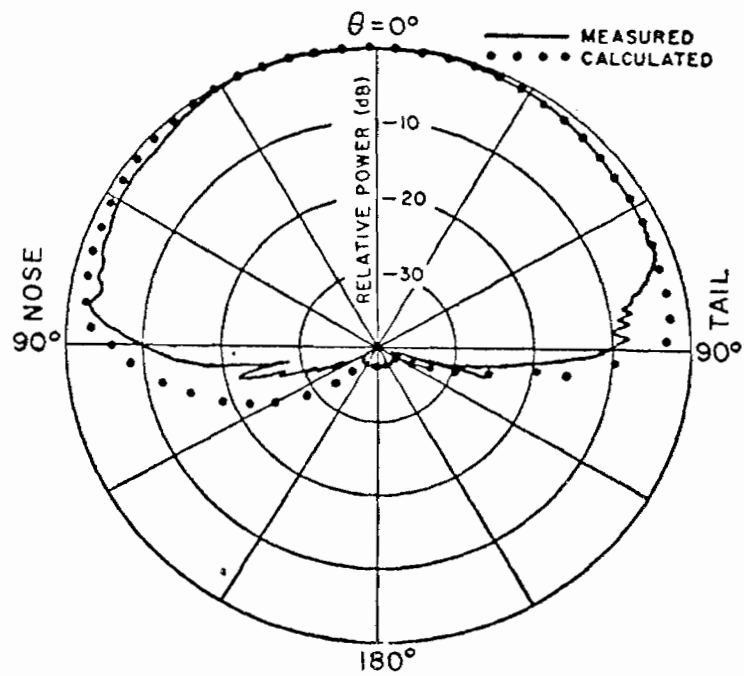
Figure 15b. Elevation plane pattern for a circumferential KA-band
waveguide mounted above the wings on a KC-135 aircraft.
(No radome and vertical stabilizer included).
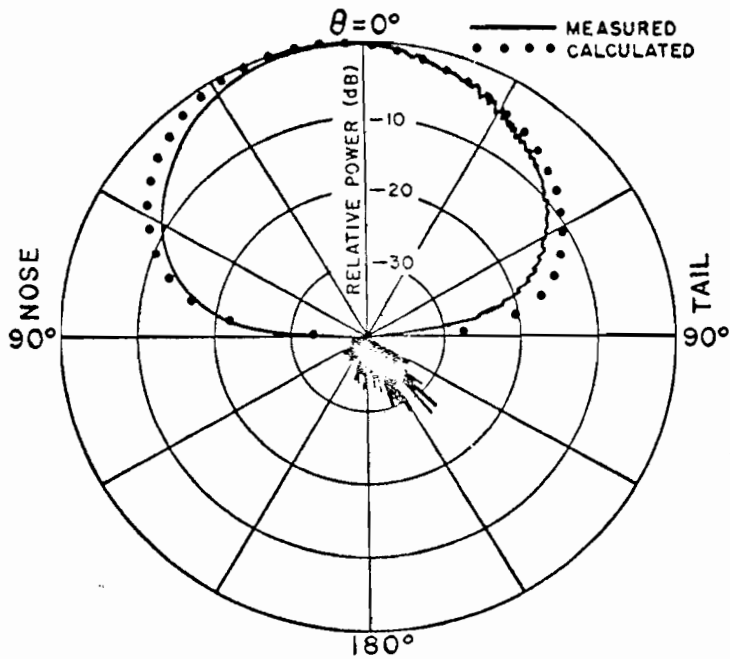
Figure 16a. Elevation plane pattern for an axial KA-band wave-
guide mounted forward of the wings on a KC-135 air-
craft. (No radome and vertical stabilizer included).
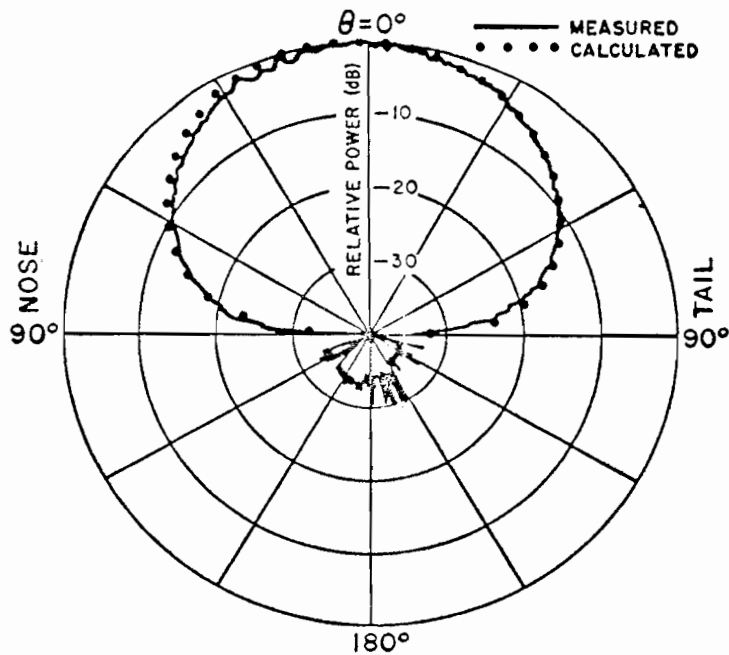
Figure 16b. Elevation plane pattern for an axial KA-band wave-
guide mounted above the wings on a KC-135 aircraft.
(No radome and vertical stabilizer included).
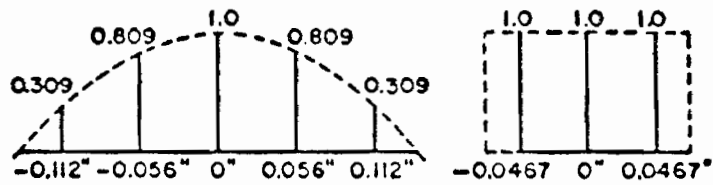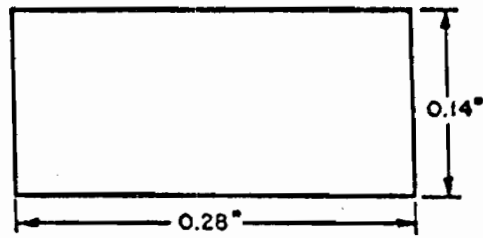
Figure 17. Approximation of an open-end waveguide by an array of 5 infinitesimal broad wall elements with different weights and an array of 3 infinitesimal narrow wall elements with uniform weight.

The comparison between calculated and measured results is encouraging, especially when the antennas are located above the wings. The discrepancy displayed in the fore and aft regions, particularly for the case of antennas located forward of the wing, is due to the effects of the cockpit and nose section and the vertical stabilizer which are neglected in the present theoretical model.

In the preceding analysis, the effect of the aircraft in the nose of the radome was neglected. In order to simulate a fuselage with a radome, a truncated composite elliptic cylinder model as shown in Fig. 18 is adopted. This is based on experimental data that the radome effect appears to be a diffraction from the bulk head as if the radome were not present.

Before proceding to solve this problem, by careful consideration it can be converted into a simpler problem. With the fact that a slot or monopole radiating in the presence of a composite elliptic cylinder can be considered as an antenna itself, the present problem can be approximated by the radiation problem of an equivalent antenna mounted on a wedge type structure as shown in Fig. 19.where the antenna is mounted on the bottom of the fuselage. This equivalent antenna radiates the same pattern as that of a slot or monopole mounted on our previous model without the radome considered. The wedges are formed and defined by the tangent planes at the discontinuities Q_1 and Q_2. Thus, the radiation problem of a fuselage model with a radome included is transformed to a wedge diffraction problem, and can be solved using standard GTD techniques.

Figure 19 illustrates the necessary components of the total electric field in the different regions given by

$$
\bar{E}^t =
\begin{cases}
\bar{E}^i_{eq} + \bar{E}^d + \bar{E}^{dd} & \pi - \phi_{\omega 1} \le \theta \le \pi, \ \phi = 0 \\
\\
\bar{E}^d + \bar{E}^{dd} & 0 \le \theta \le \pi - \phi_{\omega 1}, \phi = 0 \\
\\
\bar{E}^{dd} & 0 \le \theta \le \pi - \phi_{\bar{\omega} 2}, \phi = \pi \\
\\
\bar{E}^i_{eq} + \bar{E}^d & \pi - \phi_{\omega 1} \le \theta \le \pi, \phi = \pi
\end{cases}
\tag{57}
$$

Note that $\bar{E}^i_{eq}$ is the radiated field of the equivalent antenna described above, $\bar{E}^d$ is the singly diffracted field from edge 1 and $\bar{E}^{dd}$ is the diffracted field from edge 2. It is noted that the contributions from any other higher order diffraction terms are so small compared to single and double diffraction that they are ignored for our purposes.
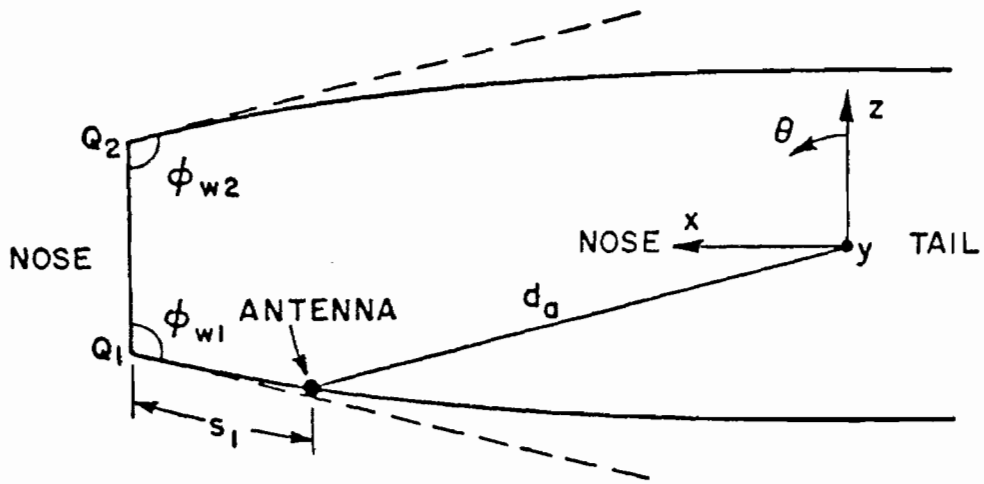
Figure 18. Truncated composite ellipse as simulation of fuselage with radome included.
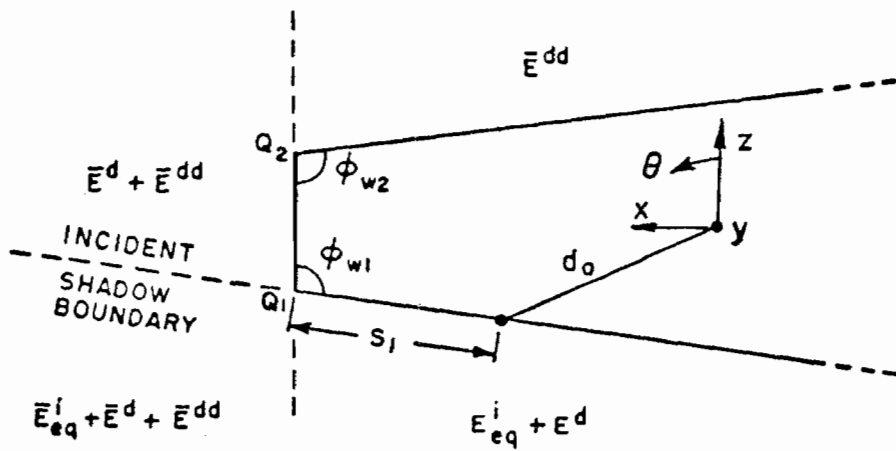
Figure 19. Total field distribution.

Using Eq. (57), the elevation plane patterns for the space shuttle as shown in Fig. 20 with the radome included are calculated. Figures 21 to 23 illustrate the radiation patterns for both vertical (monopole and circumferential waveguide) and horizontal (axial waveguide) polarization sources mounted on the fuselage of the 1/35th scale model of the space shuttle with the radome considered. The structure used to simulate the 1/35th scale model consists of a 2.55" by 12.5" left semi-ellipse and a 2.55" by 60.0" right semi-ellipse. The size of the radome is 6.5" and the source is mounted 2" away from the radome. Figure 24 shows the radiation pattern of the space shuttle with radome size being 2" and antenna mounted 1/2" away from radome. Note that the waveguide used here is the same KA-band waveguide used previously. The experimental results, which were taken at NASA (Hampton, Va.) at a frequency of 35 GHz, are also presented. The agreement between calculated and measured results illustrates the applicability of the numerical analysis technique being developed in this study.

Note also that although the elevation plane model can be used to compute the elevation plane pattern as well as off-elevation plane patterns, it is found that for our fuselage model, this model can only be used to compute the off-elevation plane patterns accurately up to approximately $\pm 30°$ from the elevation plane.

2. ANALYSIS OF ROLL PLANE MODEL

The basic aircraft to be analyzed in this section is composed of flat plates attached to an infinitely long elliptic cylinder. Originally, a circular cylinder was used to represent the fuselage [27], and the modal solutions were employed to determine the field. However, an aircraft cross section is not circular in general. To be able to predict the radiation pattern more accurately, one has to consider a better model for the fuselage approximation.

Since the roll plane cuts orthogonally across the fuselage, one should expect the fuselage cross section to have a strong effect on the roll plane pattern. On the other hand, an aircraft fuselage is normally long and slender, such that its finite length effects are generally secondary. Consequently, the infinitely long elliptic cylinder representation of the fuselage for roll plane calculations appears to be a reasonable approximation in most cases. Since the antenna can be arbitrarily positioned on the fuselage with respect to the wings, one must consider the width of the wing as well as its length in order to obtain a practical analytic model. In order to accomplish this, the near field bent plate scattering solution is adapted to this new model such as illustrated in Fig. 25. Note that the wings are
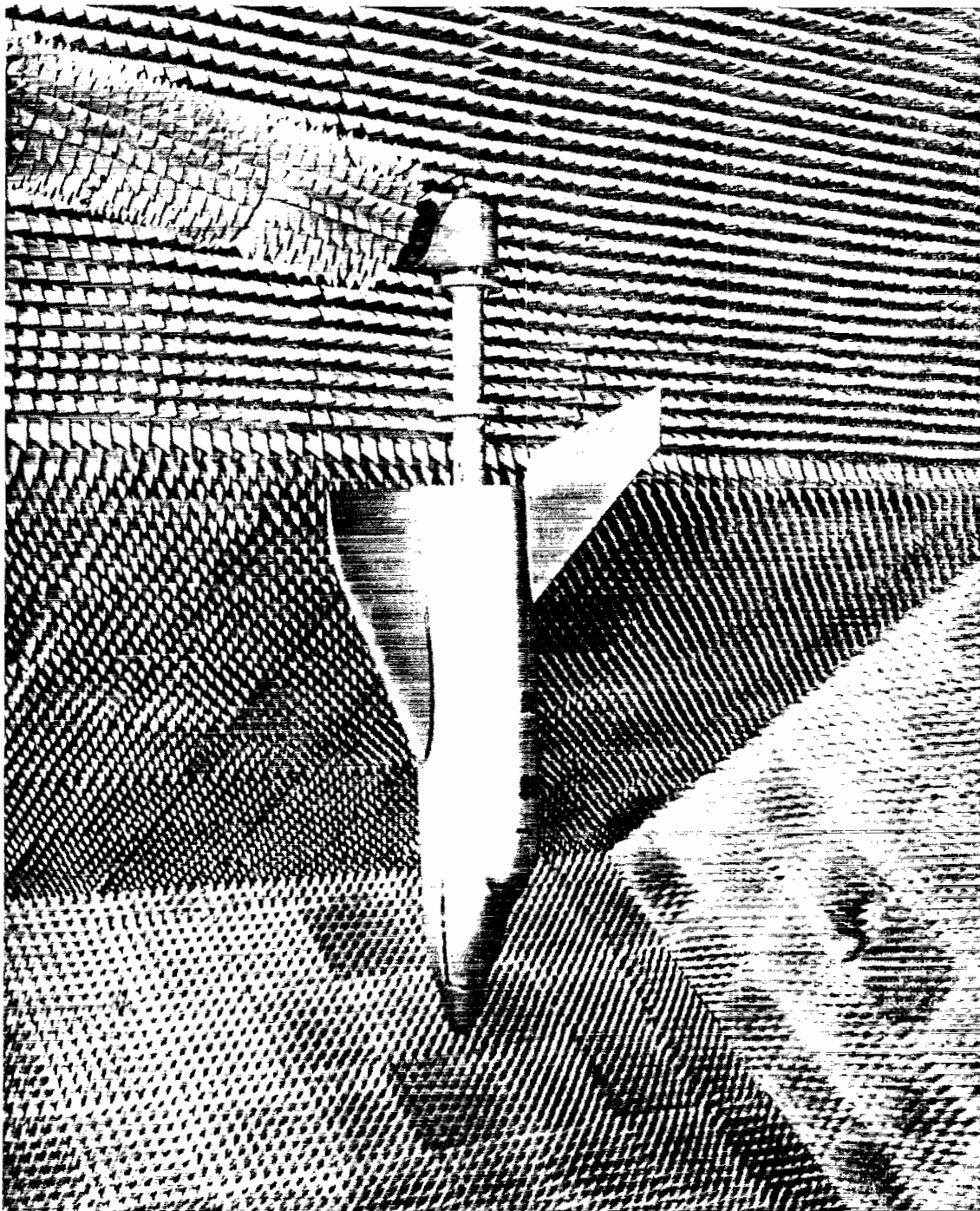
Figure 20a. Scale model (1/35) of Space Shuttle in Anechoic
Chamber at NASA, (Hampton, Va.).
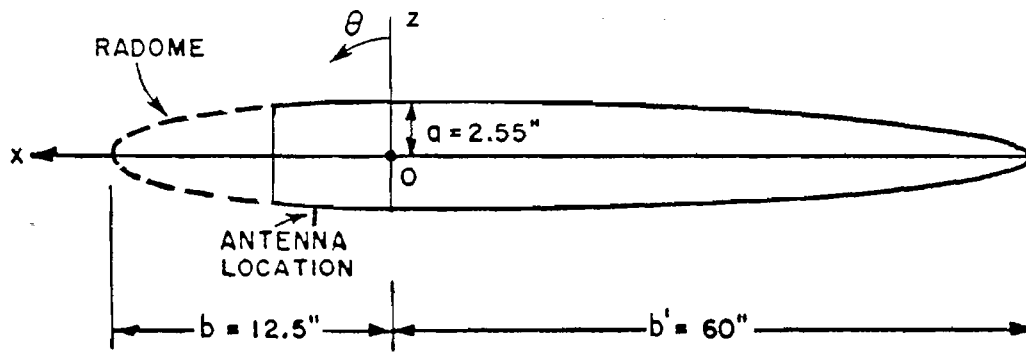
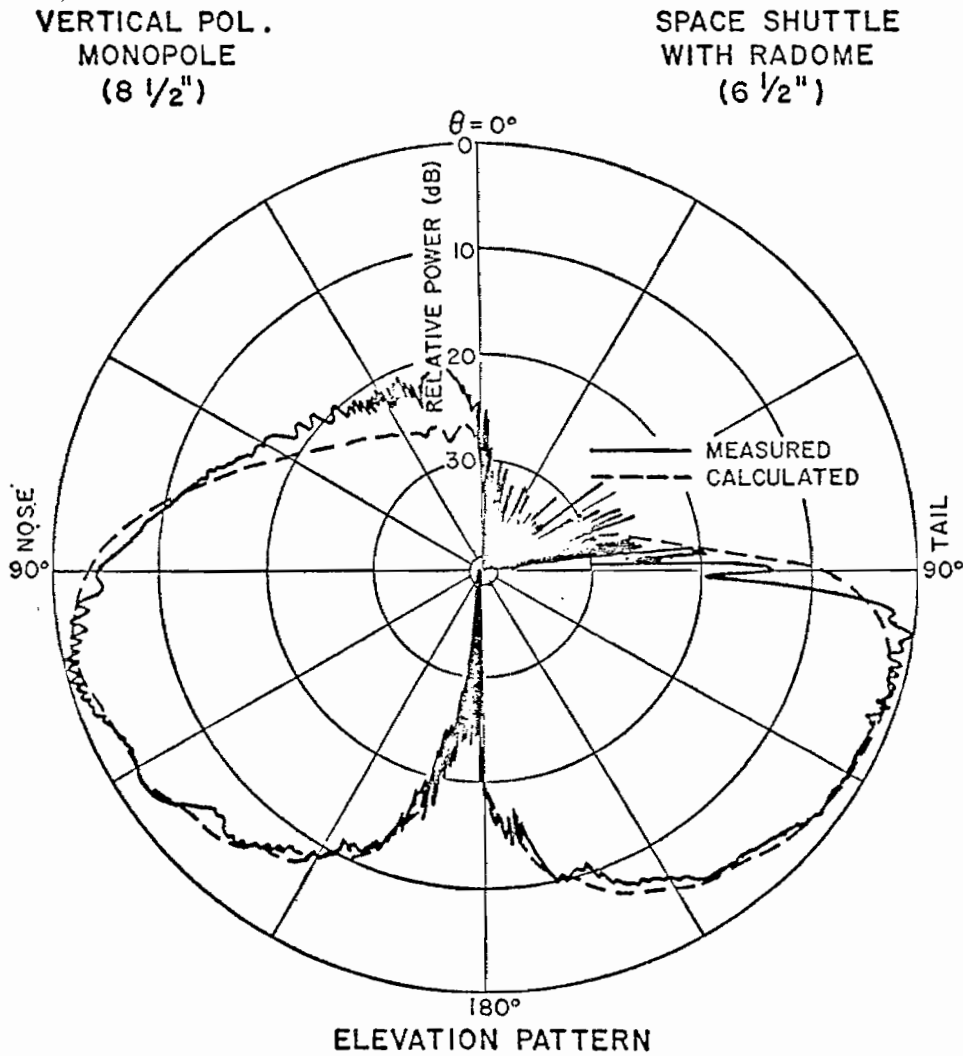Figure 20b. Theoretical model of 1/35th scale model of space shuttle.

VERTICAL POL.
MONOPOLE
(8 ½")

SPACE SHUTTLE
WITH RADOME
(6 ½")

$\theta = 0°$

RELATIVE POWER (dB)

0

10

20

30

MEASURED
CALCULATED

NOSE
90°

TAIL
90°

180°

ELEVATION PATTERN

Figure 21. Elevation pattern of monopole on a 1/35th scale model
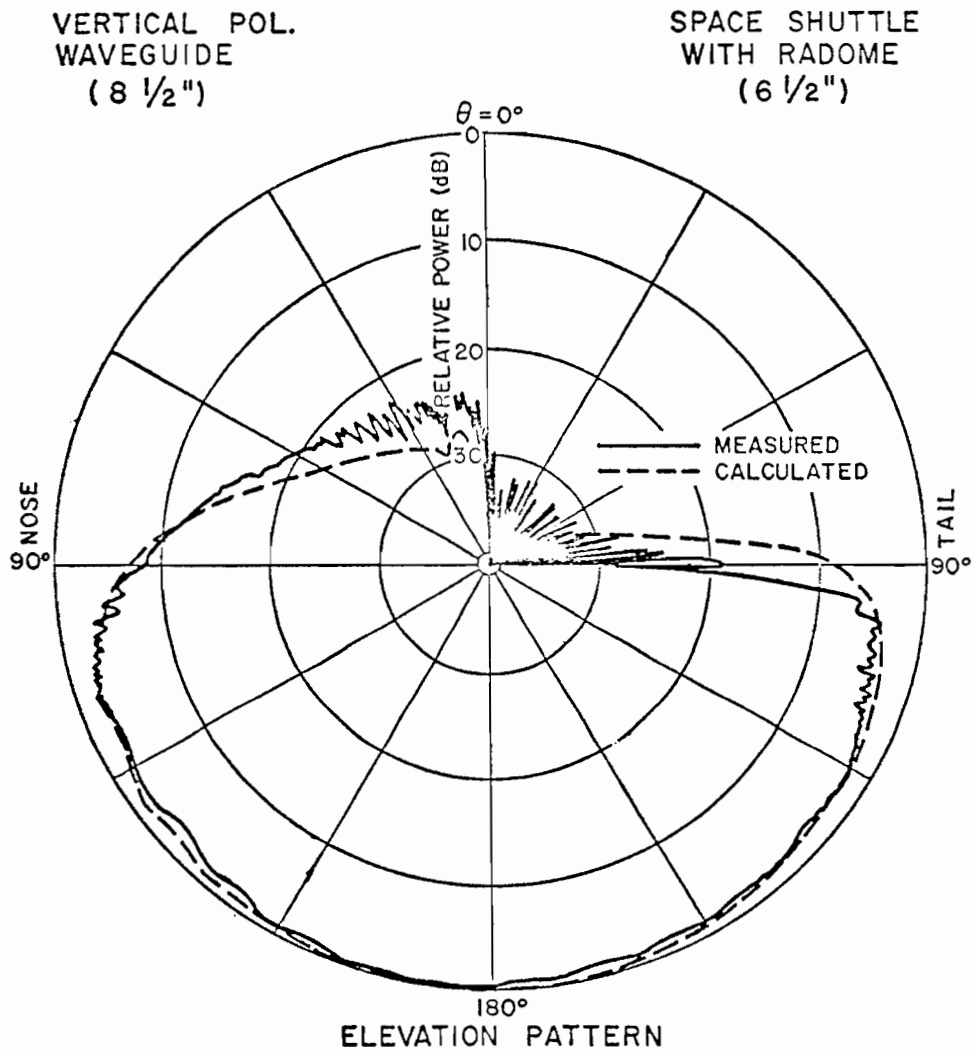of space shuttle (with radome included).

56

VERTICAL POL.
WAVEGUIDE
(8 ½")

SPACE SHUTTLE
WITH RADOME
(6 ½")

$\theta = 0°$

RELATIVE POWER (dB)

90° NOSE

TAIL 90°

—— MEASURED
- - - - CALCULATED

180°
ELEVATION PATTERN

Figure 22. Elevation pattern of circumferential slot on a
1/35th scale model of space shuttle (with radome
included).

57
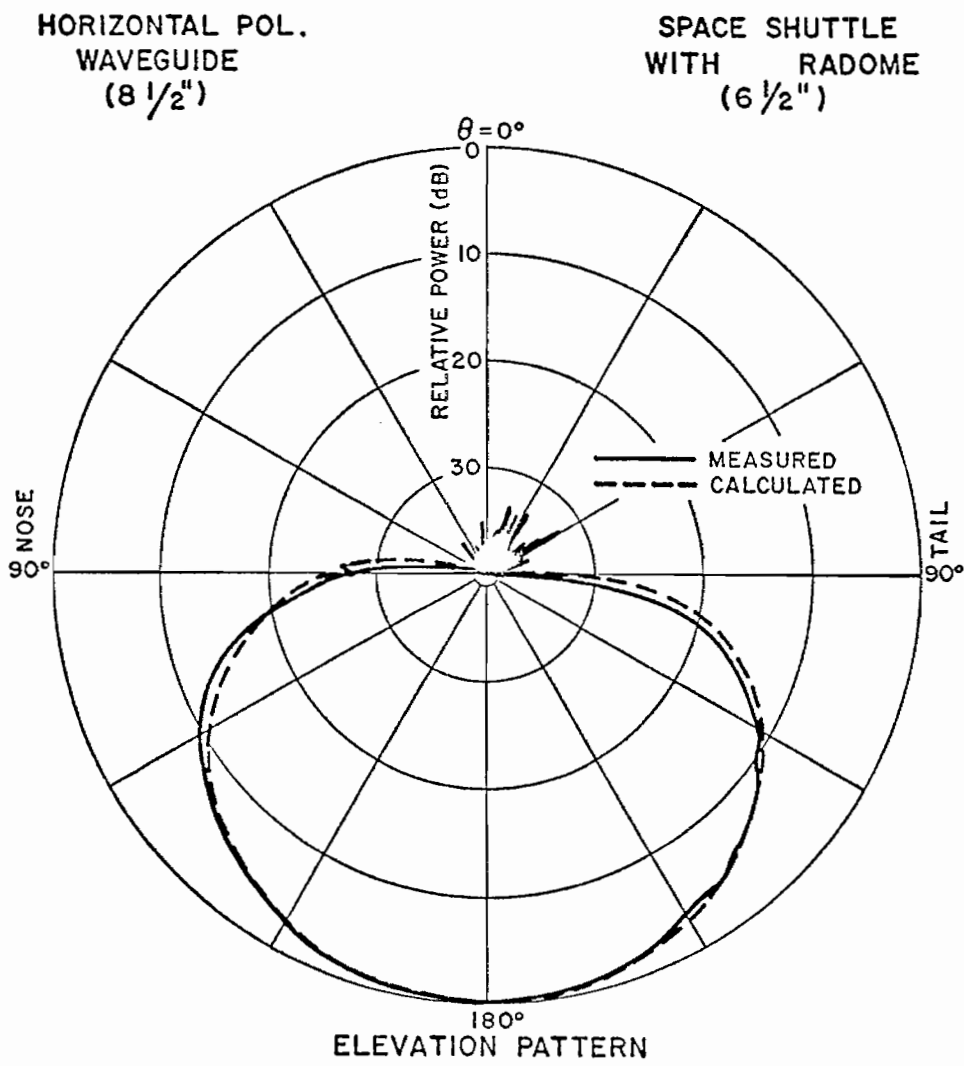
Figure 23. Elevation pattern of axial slot on a 1/35th scale
model of space shuttle (with radome included).

HORIZONTAL POL.
WAVEGUIDE
(2 ½")

SPACE SHUTTLE
WITH RADOME
(2")

θ = 0°

RELATIVE POWER (dB)

10

20

30

MEASURED
CALCULATED

90° NOSE

90° TAIL

180°
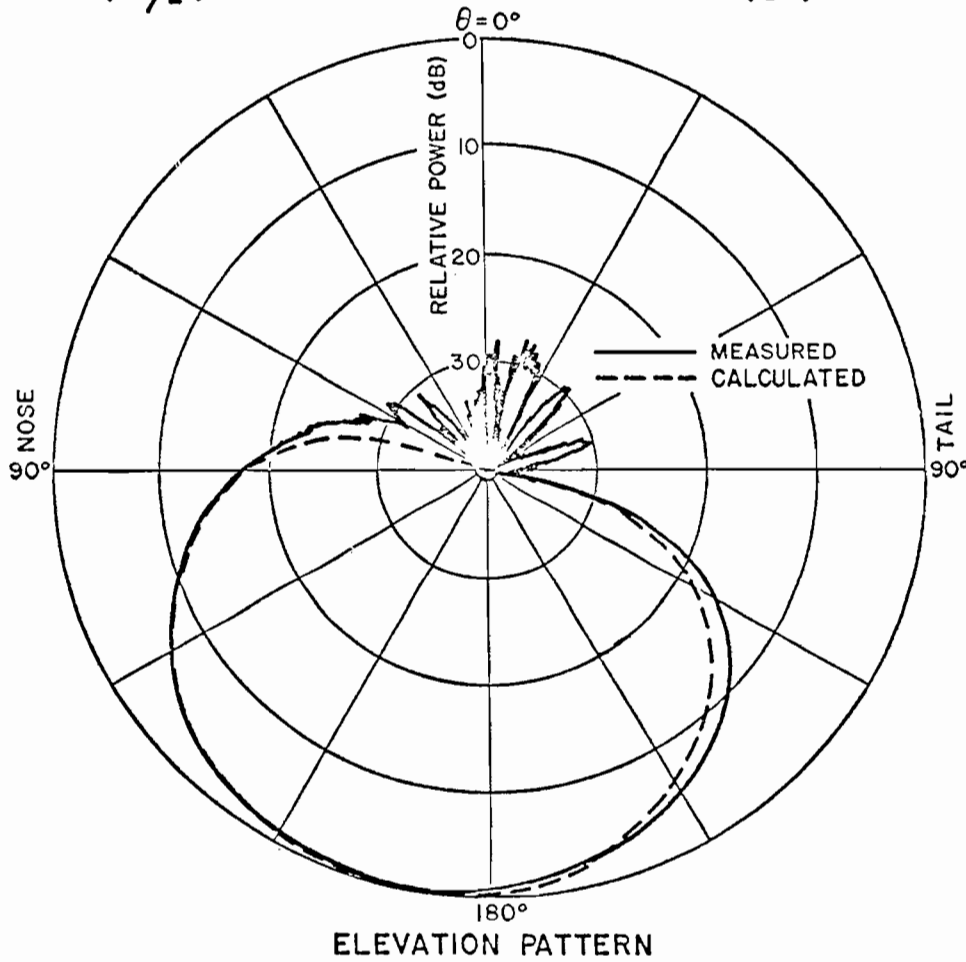
ELEVATION PATTERN

Figure 24. Elevation pattern of axial slot on a 1/35th scale
model of space shuttle (with radome being 2").
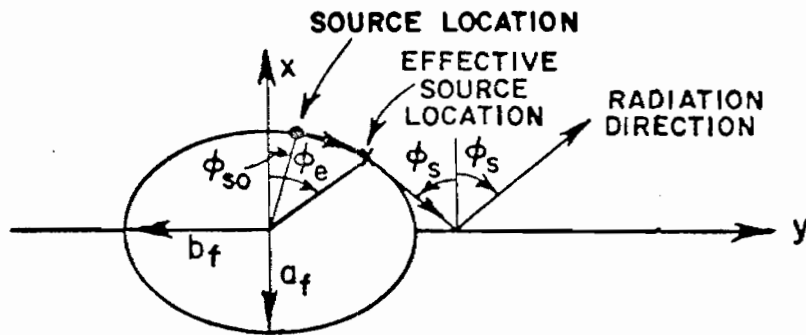
Figure 25a. Reflection problem in x-y plane.
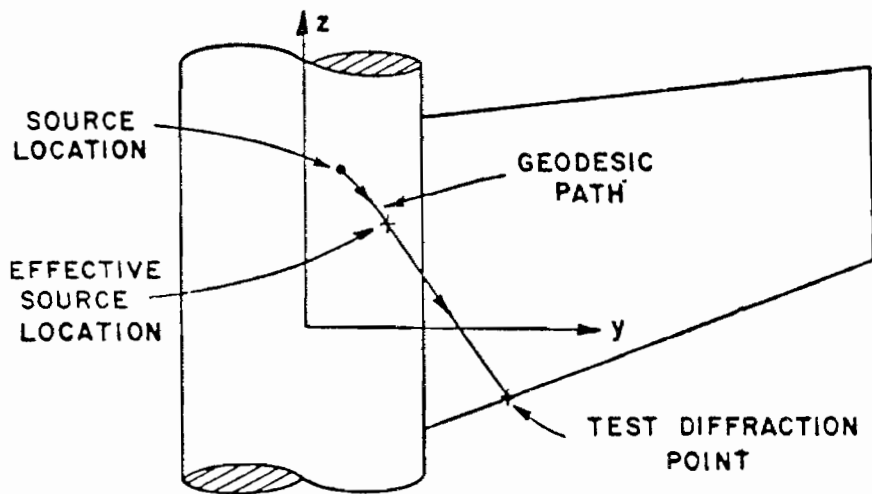
Figure 25b. Diffraction problem in y-z plane.

60

assumed flat here and each wing can be located arbitrarily
with any number of edges. The wings, also, can be mounted up
or down from the central location provided that the wings are
horizontal.

The model, now, consists of an infinitely long elliptic
cylinder fuselage to which finite flat wings are attached. The
various configurations analyzed are shown in Fig. 26 looking
from the front of the aircraft with the antenna mounted in
each case above the wings for the models illustrated. Using
these models, one should be able to analyze a wide variety of
aircraft shapes. This is verified by a comparison of results
taken on actual aircraft scale models and presented later.

Let us first find the effective source location for the
reflected field. Recall that in the flat plate result, the
source was imaged and the reflected field added to the total
solution provided the image ray passed through the finite
flat plate (wing) limits. One must initially determine the
effective source position and then the reflected field. With
the source mounted on an infinitely long elliptic cylinder,
the surface rays from the source propagate around the cylinder
along geodesic paths, from which energy is continually diffracted
tangentially. Now let us assume that the source does not illumi-
nate the right wing directly (as illustrated in Fig. 25(a)) and
proceed to determine the unique geodesic path that diffracts
energy from a known tangent point which is then reflected off
the wing in the desired radiation (or scatter) direction.

The effective source position for reflections from the right
wing in terms of the radiation direction (θ_s, ϕ_s) is given by

$$x_e = a_f \cos v_e$$

$$y_e = b_f \sin v_e \qquad\qquad (58)$$

$$z_e = \cot \theta_s \int_{v_{so}}^{v_e} \sqrt{a_f^2 \sin^2 v + b_f^2 \cos^2 v}\; dv + z_{so}$$

where $v_e = \tan^{-1}(b_f/a_f \cot \phi_s)$. These coordinates can, then,
be used in the flat plate problem as the effective source loca-
tion. Note that as the desired radiation direction is varied,
the effective source location changes. In addition, if the
source directly illuminates the wing for a given reflection
term, then the effective source location is simply the actual
source location (u_f, v_{so}, z_{so}). A result similar to Eq. (58)
can be found for the reflections from the left wing. Finally,
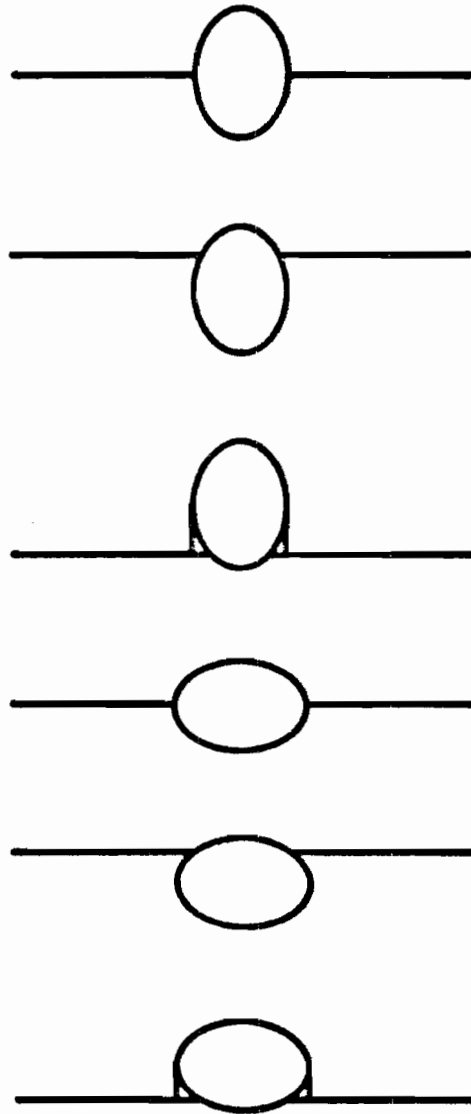
Figure 26. Fuselage and wing geometry for theoretical aircraft
model looking from the front. The antenna is always
mounted on top of the models.

the actual source field value used to compute the reflected term is determined from the GTD solutions in Chapter II.

Using a similar technique, the effective source locations for the diffracted field components may be found. The bent plate solution uses a search technique to find the diffraction point by computing the diffraction angles at selected test points along a given edge. Once a test point (x_d, y_d, z_d) is specified along the edge, one can find the effective source location (x_e, y_e, z_e) using the geometry illustrated in Fig. 25(b). Again it is assumed that the source does not directly illuminate the test point. One finds that the effective source is given by

$$x_e = \frac{a_f^2 b_f^2 x_d + a_f^2 y_d \sqrt{a_f^2 y_d^2 + b_f^2 x_d^2 - a_f^2 b_f^2}}{a_f^2 y_d^2 + b_f^2 x_d^2}$$

$$y_e = \frac{a_f^2 b_f^2 y_d - b_f^2 x_d \sqrt{a_f^2 y_d^2 + b_f^2 x_d^2 - a_f^2 b_f^2}}{a_f^2 y_d^2 + b_f^2 x_d^2}$$

$$z_e = \frac{b_f x_e z_d I_v + a_f z_{so}(y_d - y_e) I_v'}{b_f x_e I_v + a_f (y_d - y_e) I_v'} \tag{59}$$

where

$$I_v = \int_{v_{so}}^{v_e} \sqrt{a_f^2 \sin^2 v + b_f^2 \cos^2 v} \; dv,$$

$$I_v' = \sqrt{a_f^2 \sin^2 v_e + b_f^2 \cos^2 v_e}, \quad \text{and} \quad v_e = \tan^{-1}\left(\frac{y_e/b_f}{x_e/a_f}\right)$$

Given the effective source location for the chosen test point, the search technique is applied to find the actual diffraction point along a given edge. Note that once the actual diffraction point is determined, the effective source of the diffracted field is specified by Eq. (59), and the source field value is, again, computed using the GTD solutions.

The total field is found by summing the directly radiated field with the scattered field using the superposition principle. The results for a λ/4 monopole on the fuselage of a 1/25th scale model of a KC-135 aircraft, as shown in Fig. 12, forward and over the wings are shown in Figs. 27 (a) and (b), respectively. The results for a KA-band circumferential waveguide forward and over the wings are shown in Fig. 28. The results for a KA-band axial waveguide forward and above the wings are shown in Fig. 29. The fuselage, in this case, is approximated by a 3" x 3" infinitely long elliptic cylinder. The waveguide antenna is modeled as in the previous section, and the agreement in each case is very encouraging. Again, it should be stressed that the roll plane model solution not only can predict the radiation pattern accurately in the roll plane, it also can be extended to cover almost the complete volumetric pattern as shown in Ref. [30].

3. THREE-DIMENSIONAL MODEL APPROXIMATION OF AN AIRCRAFT

The analytical solutions described in the previous sections provide a useful, efficient, and economical way for the evaluation, location, and design of fuselage mounted antennas based on their pattern performance in principal planes. However, if modern systems are to function properly, the antenna pattern must meet certain specifications. These specifications are usually given in terms of a coverage diagram for a particular sector in space which is to be met with antenna mounted on the aircraft not on a finite ground plane where the original antenna design was made. Thus, the desire for an accurate solution for the complete pattern performance of antennas mounted on a complex aircraft structure for given applications requires a more thorough study of ways to handle the volumetric pattern.

If this problem is attacked directly by analyzing rays on complex three-dimensional surfaces as done previously in Reference [2], the resulting numerical solution would be very complex, time-consuming, and uneconomical. Nevertheless, if certain assumptions can be made, the approach undertaken in the previous sections can be used to overcome these difficulties and simplify the problem a great deal.

First, it has been shown by numerous scale model measurements that the roll plane model can be extended to almost cover the complete volumetric pattern except for two conical sectors (fore and aft) [30]. The limitations of the roll plane model result are due to the finite length fuselage. Yet, the finite length fuselage has been solved, previously, in the elevation plane model analyses. Furthermore, based on the previous

64
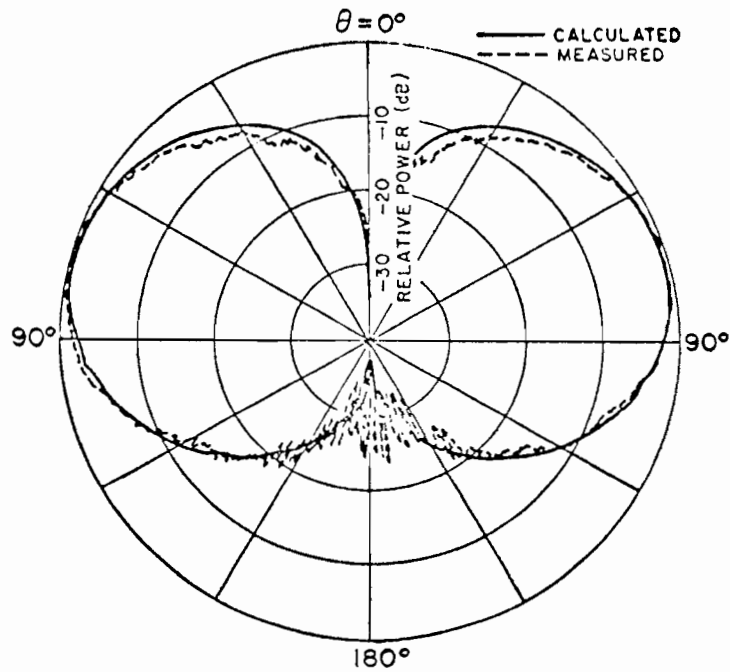
Figure 27a. Roll plane pattern (E_ϕ) for a 1/25 scale model of a KC-135 with a $\lambda/4$ monopole on the fuselage forward of the wings at freq. = 34.92 GHz (model frequency).
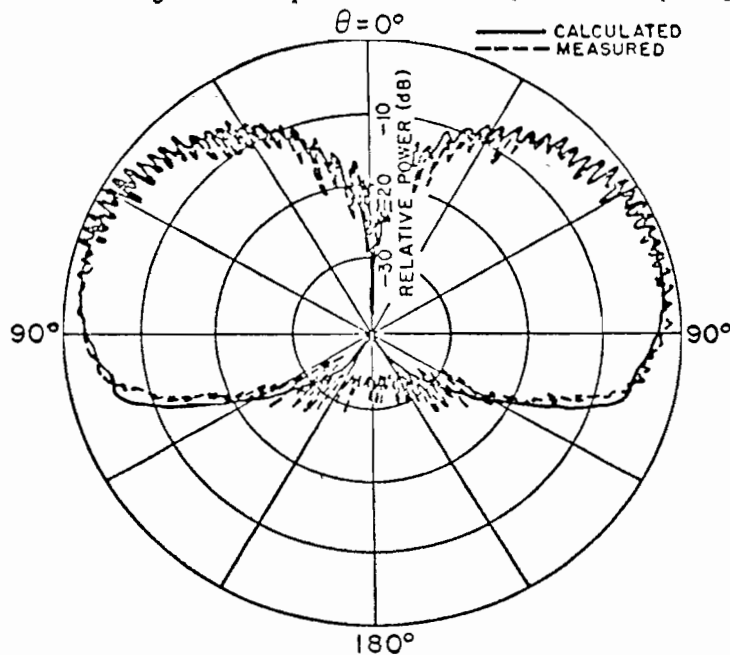

Figure 27b. Roll plane pattern (E_ϕ) for a $\lambda/4$ monopole above the wings.
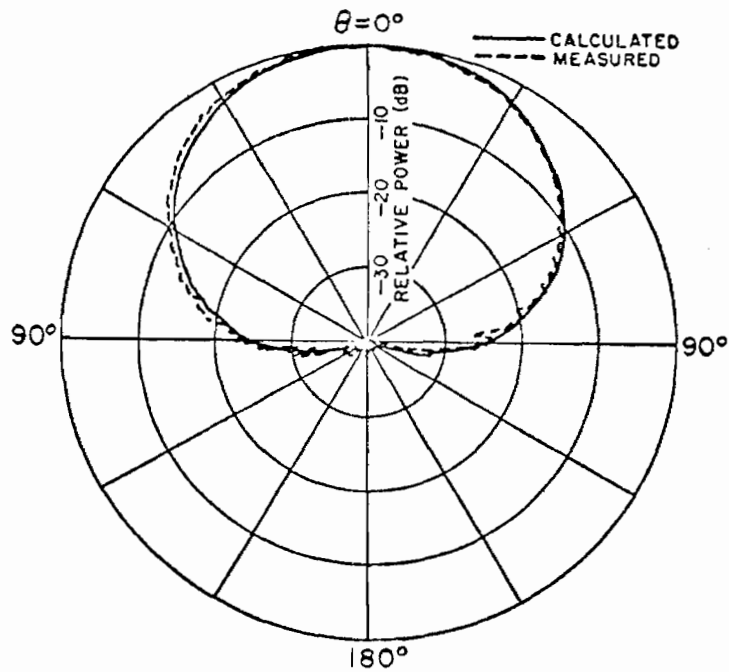
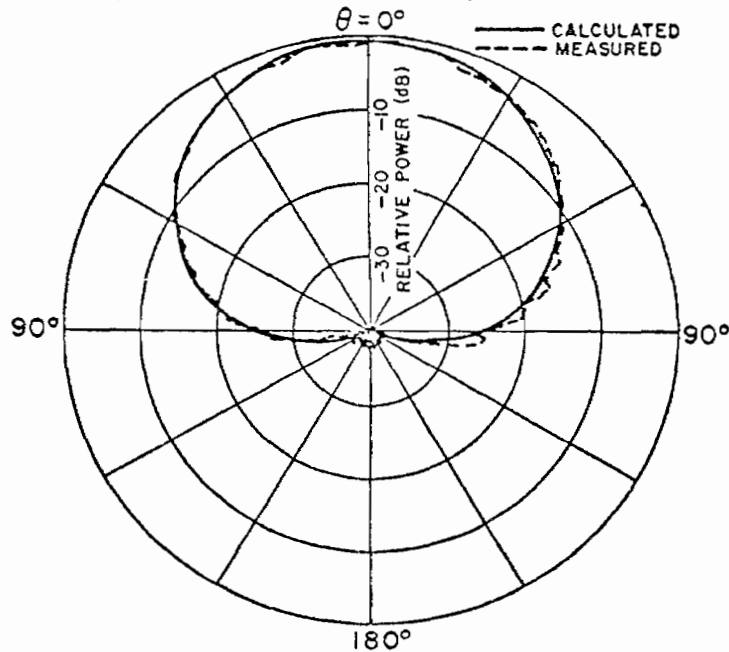Figure 28a. Roll plane pattern (E_θ) for a KA-band circumferential waveguide forward of the wings.

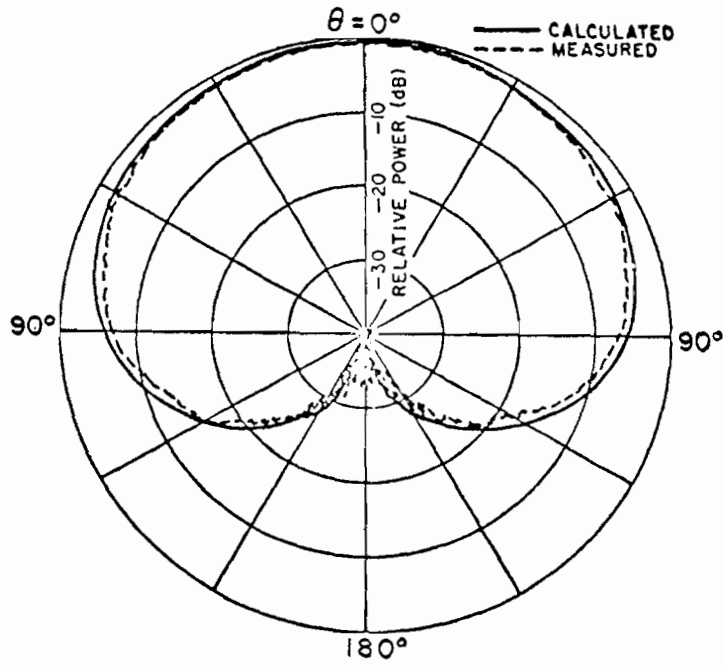Figure 28b. Roll plane pattern (E_θ) for a KA-band circumferential waveguide above the wings.

Figure 29a. Roll plane pattern (E_ϕ) for a KA-band axial waveguide forward of the wings.
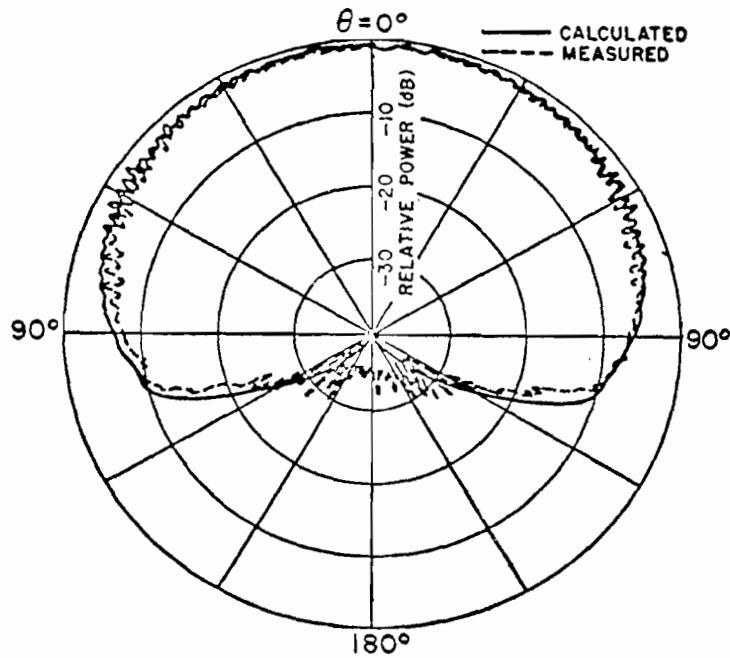
Figure 29b. Roll plane pattern (E_ϕ) for a KA-band axial waveguide above the wings.

three-dimensional studies of geodesic rays which contribute to the
pattern of an antenna on various prolate spheroids, one is
able to combine the analyses of these two principal plane models
to give the complete pattern. In this study, computer simulation
models were considered that would resemble a wide variety of
aircraft shapes and yet could, also, be analyzed with reason-
able accuracy and economy. In this case, it is quite obvious
that the three-dimensional nature of the fuselage must be
modeled if one is to adequately determine volumetric patterns.

This resulted in the development of a general surface of
revolution model for the fuselage as presented in Reference
[2]. Through an extensive study of geodesic paths on a surface
of revolution, the number of dominant rays that contributed to
the radiation pattern were shown to be finite except for more
spherical shapes. Furthermore, the computer result showed that,
for a prolate spheroid, the dominant rays needed to be con-
sidered would not exceed four rays; in most cases, it is even
less than that. These four rays are illustrated in Fig. 30
in which two rays are propagating along the cross-section of
prolate spheroid; the other two are propagating along the profile.
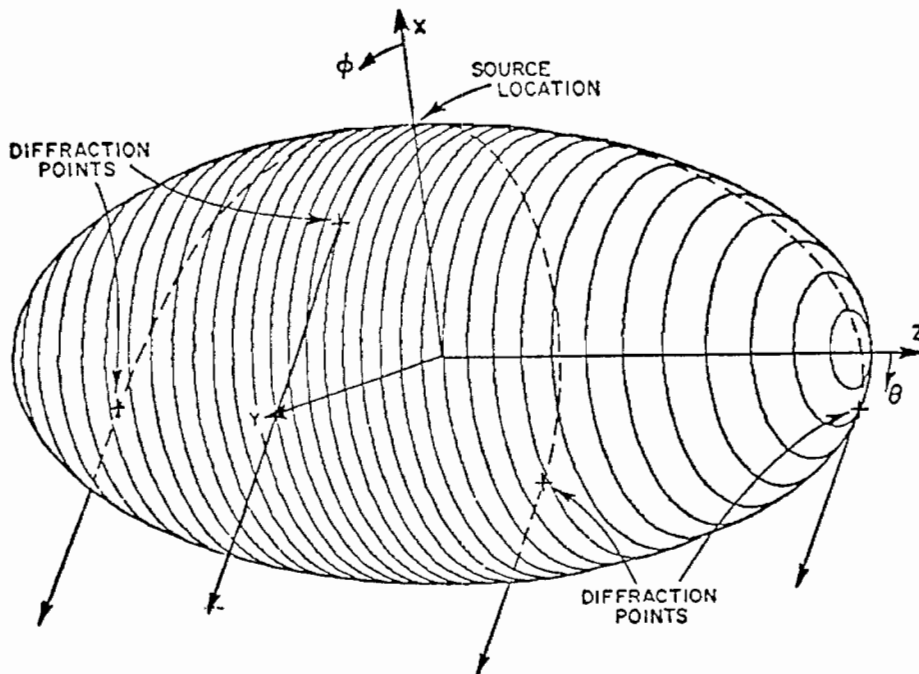
Figure 30. The four dominant GTD terms that radiate at
$\theta = 90°$, $\phi = 145°$).

68

To demonstrate the significance of the four-ray contribution, the elevation plane pattern of an axial slot mounted on a prolate spheroid was calculated using a two-dimensional (two rays) and three-dimensional (four rays) solution as shown in Fig. 31. Experimental results are also shown to verify the calculated three-dimensional result. It is immediately obvious that the back lobe region is not calculated with sufficient accuracy using the two-dimensional result. However, the three-dimensional solution is in good agreement with the measured pattern. This leads to a new approach to handle the volumetric patterns for fuselage mounted airborne antennas in a simplified and economical manner.

As determined previously, the roll plane model (infinite elliptic cylinder with flat plate wings) can be extended to cover most of the volumetric pattern except for the fore and aft sectors (about 15° conical sector as shown in Fig. 32). To cover these sectors, one must incorporate the elevation plane model analysis with some modifications such that the effects of wings and stabilizers are also included. In doing so, two different elliptic cylinders are required to analyze the volumetric patterns; one being the cross-section (roll) cylinder and the other being the profile (elevation) cylinder. This requirement is necessary since our solutions are based on an infinitely long elliptic cylinder, in which the z-axis coincides with the axis of the cylinder.

As discussed in the previous chapter, the most significant effects on the radiation pattern result from the surface geometry nearest to the antenna. The curvature of the surface in the vicinity of the antenna location plays a dominant role in predicting the radiation pattern. Thus, the elliptic cylinders used to represent the fuselage profile and cross-section need to model the aircraft structure as accurately as possible near the antenna location. Once these two elliptic cylinders are obtained, one is able to proceed to solve for the complete volumetric pattern.

To determine the elliptic cylinders necessary to simulate the fuselage profile and cross-section, one has to find some way to approximate the curved surface near the antenna location. One way to achieve this goal is to find an analytical function which can best approximate the known curved surface profile (either in elevation or roll plane) in a least mean square error sense. This leads to the development of a best fit routine to generate the necessary ellipses for the fuselage model through the use of a digital computer.
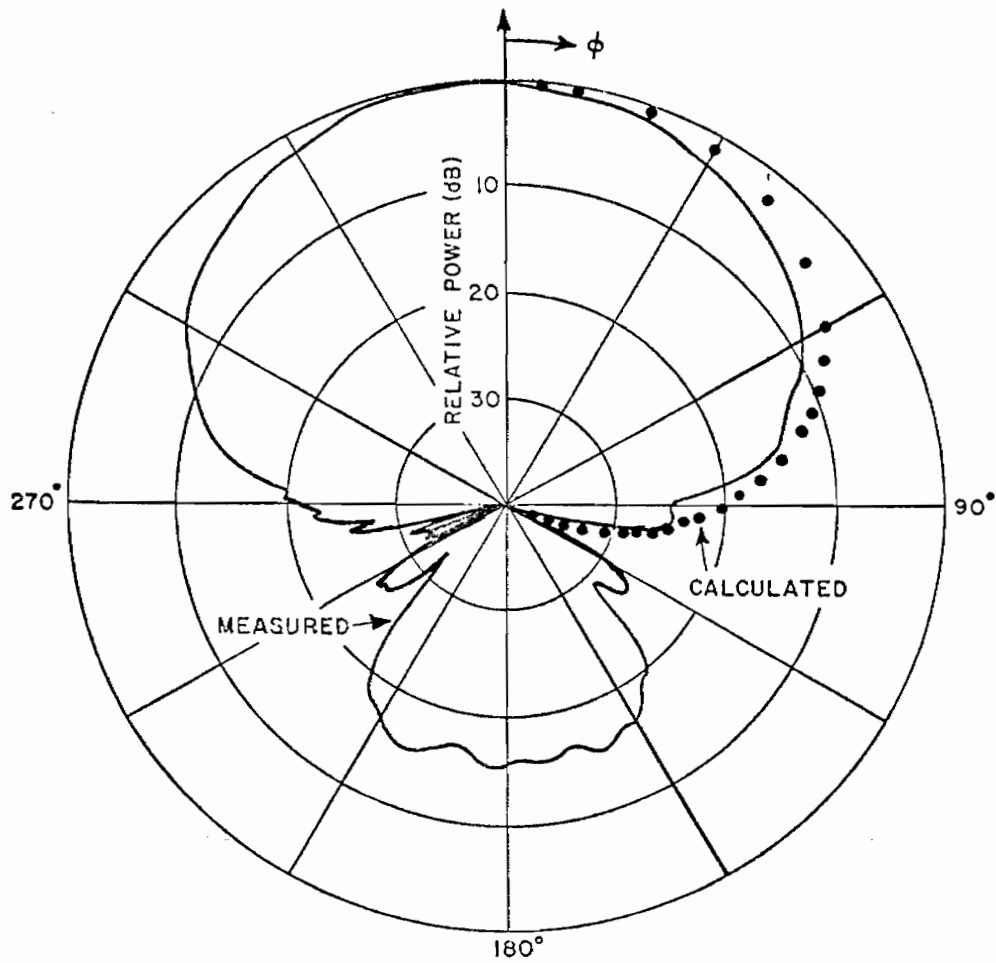
Figure 31a. Elevation plane pattern of an axial slot mounted
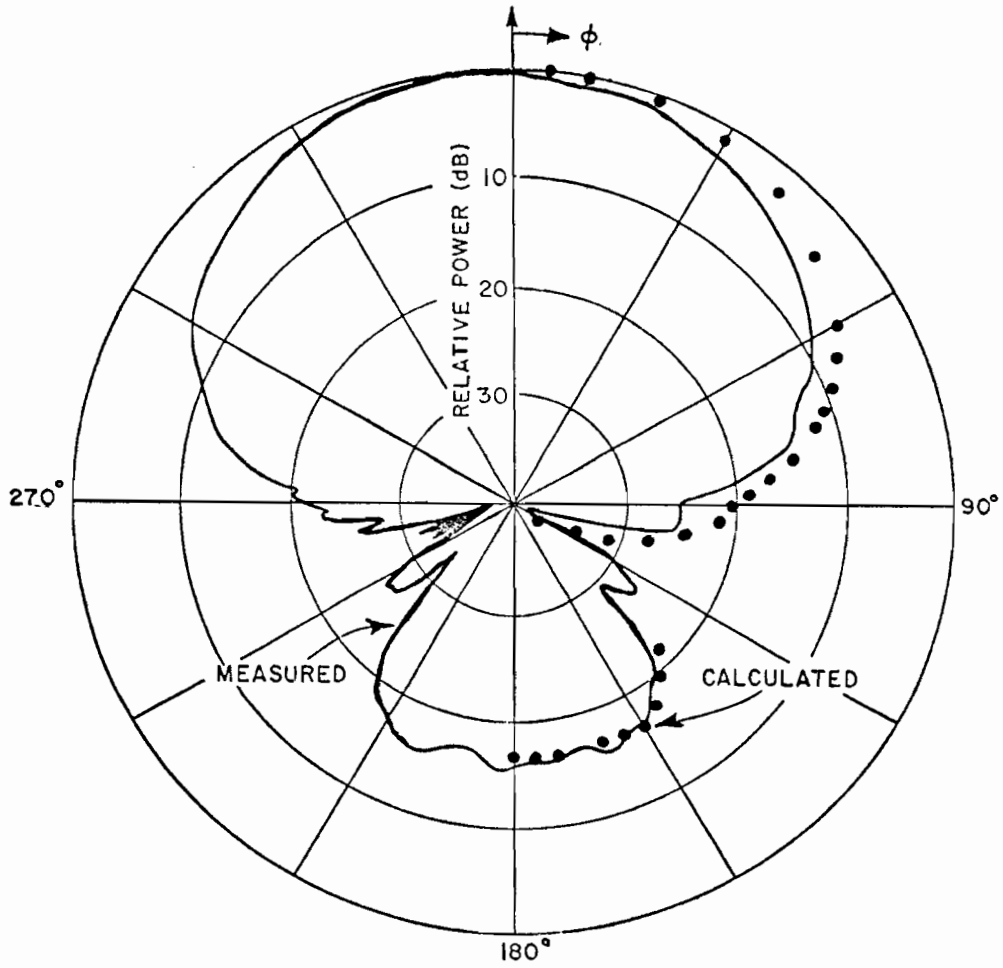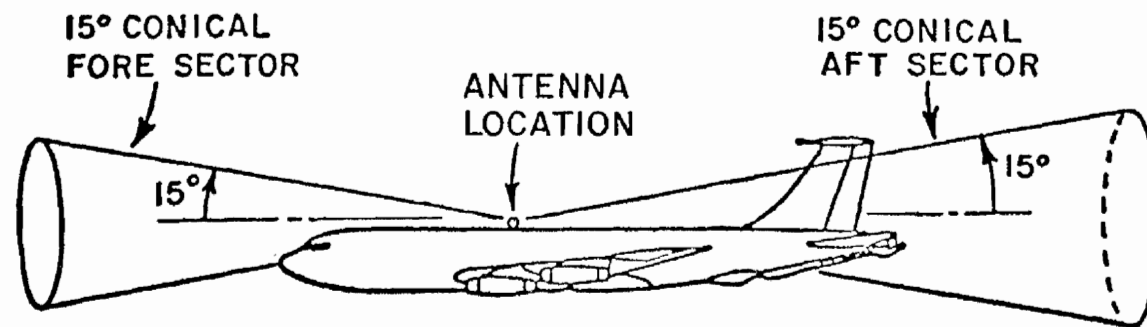on a 4λ x 2λ prolate spheroid with the two-
dimensional theoretical solution presented.

Figure 31b. Elevation plane pattern of an axial slot mounted on
a 4λ x 2λ prolate spheroid with the three-dimensional
theoretical solution presented.

Figure 32. Fore and aft sectors outside of which our "Roll Plane Model" is valid.

The theory behind the best fit routine is that a function is to be found to best approximate a set of points in a least mean square error sense. For the aircraft model, a best fit ellipse is desired. The mathematical expression for an ellipse is

$$\frac{x^2}{a^2} + \frac{y^2}{b^2} = 1 \tag{60}$$

for its origin located at $(x = 0, y = 0)$. The parameters a and b are semi major and minor axes of an ellipse, respectively. To simplify the mathematical expression, Eq. (60) can be written as

$$AX + BY = 1 \tag{61}$$

where $X = x^2$, $Y = y^2$, $A = \frac{1}{a^2}$, and $B = \frac{1}{b^2}$. Let (x_i, y_i), $i = 1, \cdots n$, be n points on which a best fit ellipse is to be generated. Substituting these points into Eq. (61), one obtains a set of n linear equations.

$$AX_1 + BY_1 = 1$$
$$AX_2 + BY_2 = 1$$
$$\vdots \qquad \vdots$$
$$AX_n + BY_n = 1$$

In matrix form, these n equations become

$$ZC = I \tag{62}$$

where

$$Z = \begin{bmatrix} X_1 & Y_1 \\ X_2 & Y_2 \\ \vdots & \\ X_n & Y_n \end{bmatrix} \qquad\qquad C = \begin{bmatrix} A \\ B \end{bmatrix}$$

DRI.

73

and

$$I = \begin{bmatrix} 1 \\ 1 \\ \vdots \\ 1 \end{bmatrix}$$

By multiplying both sides of Eq. (62) by $\tilde{Z}$, the transposed of Z, one obtains a simple 2x2 matrix as given by

$$\tilde{Z} \, ZC = \tilde{Z} \, I$$

or

$$\begin{bmatrix} \sum\limits_{m=1}^{n} X_m^2 & \sum\limits_{m=1}^{n} X_m Y_m \\ \sum\limits_{m=1}^{n} X_m Y_m & \sum\limits_{m=1}^{n} Y_m^2 \end{bmatrix} \begin{bmatrix} A \\ B \end{bmatrix} = \begin{bmatrix} \sum\limits_{m=1}^{n} X_m \\ \sum\limits_{m=1}^{n} Y_m \end{bmatrix} \tag{63}$$

which can be simply solved for A and B in the least mean square sense [56]. Thus, the ellipse parameters are defined.

Before the necessary ellipse or composite ellipse can be determined through the numerical process, the data points that described the surface of the profile or cross section of the actual aircraft fuselage must be generated. To do so, a reference Cartesian coordinates system is needed on a scale model drawing of the aircraft. These coordinates can be best located by aligning one of the axes with the center line of aircraft fuselage with the origin being arbitrarily chosen according to convenience. After the coordinate system is fixed, the positions of data points on the profile or cross-section can be measured from the scale model relative to the reference origin. The data points are taken in such a way that more points are needed around the antenna location and less points away from the source. This is due to the fact that the surface profile is dominant near the antenna location, as described earlier. Figure 33 illustrates the way data points are taken from a fuselage profile. By feeding these data points into the best fit routine and adjusting the
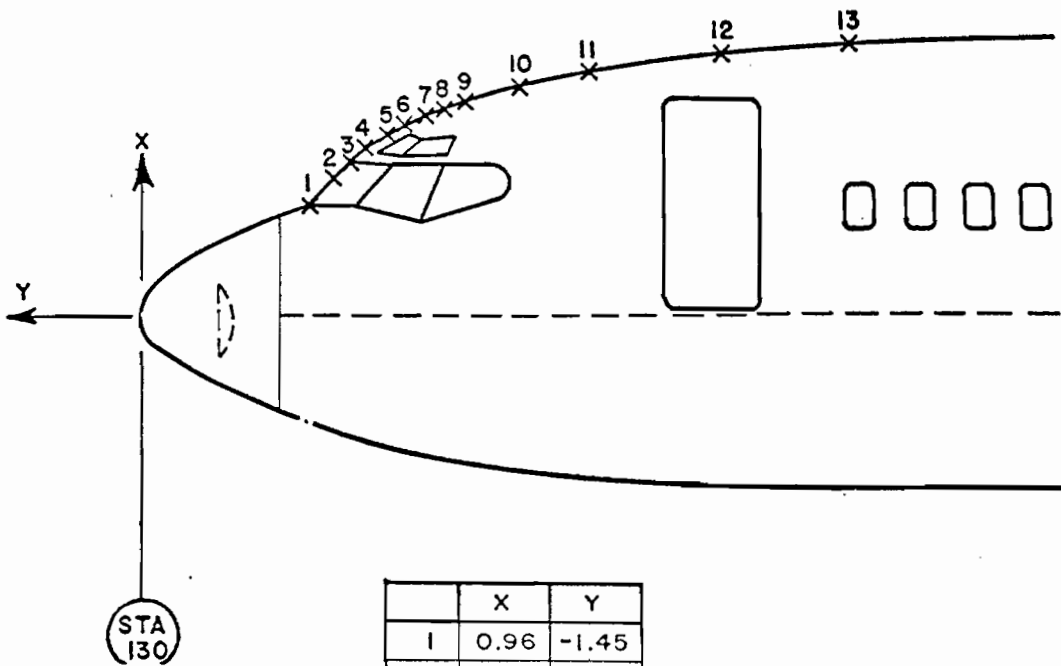
	X	Y
I	0.96	-1.45
2	1.20	-1.69
3	1.34	-1.82
4	1.45	-1.98
5	1.56	-2.16
6*	1.64	-2.30
7	1.69	-2.45
8	1.77	-2.60
9	1.84	-2.80
10	1.98	-3.28
11	2.08	-3.90
12	2.23	-5.01
13	2.30	-6.16
14	2.42	-10.14
15	2.44	-15.72
16	2.28	-24.10

* Antenna Location

Figure 33. Illustration of data points taken from the scale
model aircraft for the determination of best fit
elliptic cylinder using a digital computer.

origin of the coordinates in the routine, an ellipse is found to best fit these data points. In the same manner, the ellipse to approximate the cross-section of aircraft fuselage at the antenna location can be obtained. Thus, the elliptic cylinders necessary to simulate the fuselage profile and cross-section are determined.

Now let us consider how these two finite elliptic cylinders can be used to describe the volumetric pattern for fuselage mounted airborne antennas. First, a reference coordinate system is needed so that the solutions based on our two-dimensional analysis in two different coordinate systems can be incorporated into a complete solution. Since an aircraft fuselage is usually long and slender, its finite length effects are limited to the small sectors off the nose and tail. Consequently, the two rays which play the most significant role normally come from the cross-sectional elliptic cylinder. Thus, it seems more natural to have the reference coordinate system correspond to the roll plane model coordinate system, i.e., the Z_{ref} axis is pointed aft and the X_{ref} axis is pointed vertically upward as shown in Fig. 34. Notice that the origin of the composite ellipse in the elevation plane is chosen as the origin of the reference coordinate system for convenience.

Recall that the roll plane model is not valid in the two 15° conical sectors in the fore and aft directions. In order to overcome this handicap, a belt region around the antenna source is chosen such that in this region the solution is obtained using elevation plane model analysis. Everywhere outside the belt region, the roll plane model analysis is used to analyze the radiation pattern as done previously. Figure 35 shows the regions in which the elevation and roll plane cylinder solutions are used. The angle α is chosen such that the roll and elevation cylinder solutions blend smoothly together. In fact, α is a function of the size of elevation and roll plane cylinders used to simulate the aircraft fuselage. For most cases in our model, the angle α is set at 20°. This 20° belt has been tested and found to be satisfactory, based on comparisons with measured results, as will be shown later.

As seen in Fig. 34, the elevation plane model coordinate system is such that the Z_{elev} axis points in the Y_{ref} direction. In other words, the elevation plane model coordinate system is simply obtained by rotating the XYZ_{ref} coordinate system by a 90° angle about the X_{ref} axis. Notice that the antenna here is assumed to be mounted on the center line of the fuselage for simplicity, but this is not a basic limitation. In order to determine the electromagnetic fields in a given radiation direction ($\theta_{0\ ref}$, $\phi_{0\ ref}$) within the belt region, the solution obtained through the elevation plane model analysis is expressed in terms of the reference coordinate system such that it can be superimposed with the roll plane cylinder solution. This requires a coordinate transformation
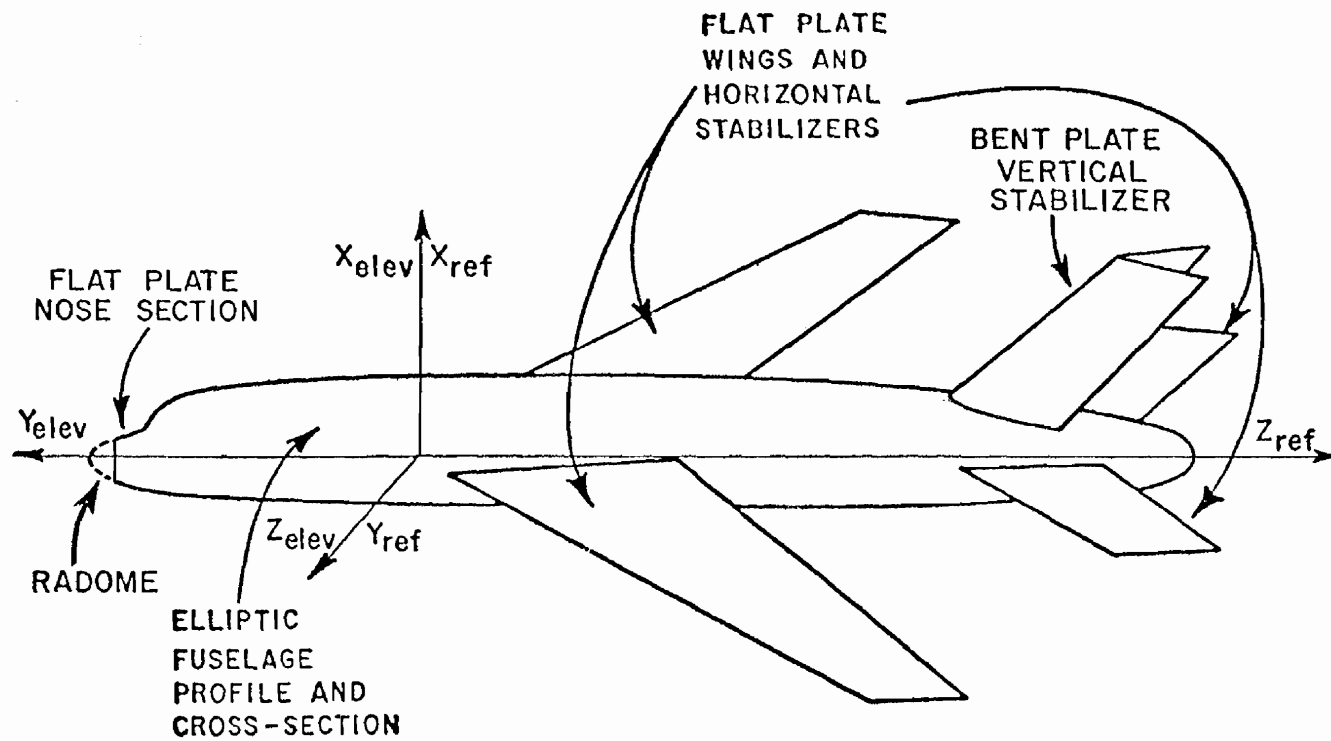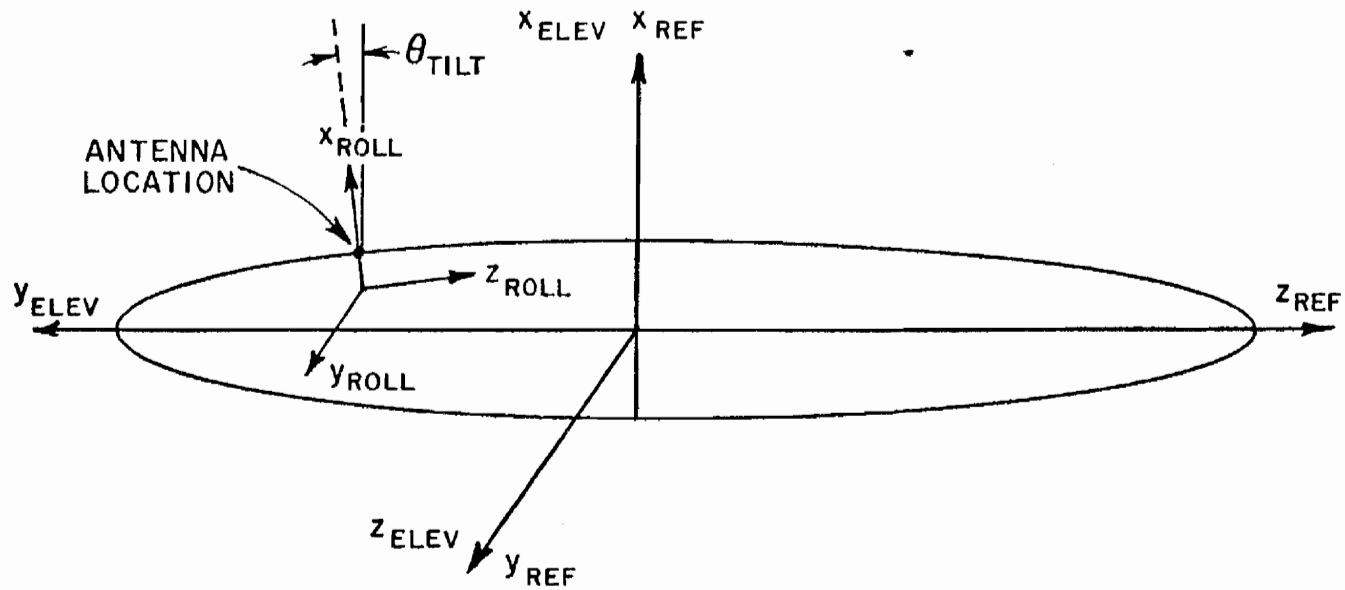
FLAT PLATE
WINGS AND
HORIZONTAL
STABILIZERS

BENT PLATE
VERTICAL
STABILIZER

FLAT PLATE
NOSE SECTION

X_{elev} X_{ref}

Y_{elev}

Z_{ref}

Z_{elev} Y_{ref}

RADOME

ELLIPTIC
FUSELAGE
PROFILE AND
CROSS-SECTION

Figure 34a. Composite aircraft model and coordinate systems illustration.

x_{ELEV} x_{REF}

θ_{TILT}

x_{ROLL}

ANTENNA
LOCATION

z_{ROLL}

y_{ELEV}

z_{REF}

y_{ROLL}

z_{ELEV}

y_{REF}

Figure 34b. Illustration of various coordinate systems used in our volumetric
pattern analysis for center-line mounted antennas.
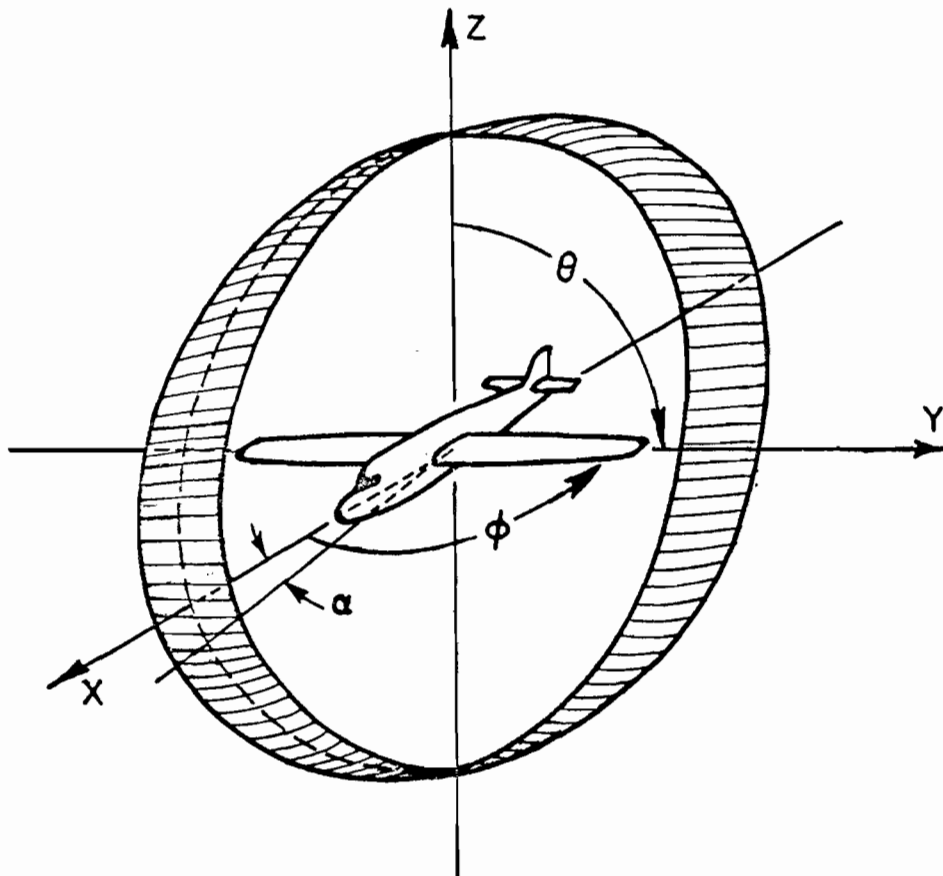
Figure 35. Illustration of belt region in which elevation plane model analysis is employed.

which relates the elevation plane model coordinates to the reference coordinate system. The transformation of coordinate systems is examined in Appendix A.

Notice that the coordinate transformations described in Appendix A are very important for the analysis. This is especially true when the antenna under consideration is mounted off the center line of the fuselage. Using these transformations not only can the electromagnetic field in the desired radiation direction in the reference coordinate system be determined through the two principal plane cylinder solutions, but the polarization problem associated with the two different solutions can also be easily resolved without any difficulty. In addition, these transformations are the foundation on which the volumetric pattern analysis is based. A detailed discussion on an off-center line mounted antenna is given in Appendix B.

To determine the radiation angle (θ_{re}, ϕ_{re}) in the elevation plane model coordinate system which corresponds to the desired radiation direction (θ_{ro}, ϕ_{ro}) in the reference coordinate system, Eqs. (80) and (83) are employed. The subscripts e and o refer to the elevation plane model and reference coordinate systems, respectively. By definition, the unit radial vector for a given direction (θ, ϕ) is given by

$$\hat{R} = \sin\theta \ \cos\phi \ \hat{x} + \sin\theta \ \sin\phi \ \hat{y} + \cos\theta \ \hat{z} \qquad (64)$$

Hence, the spherical coordinates (θ_{re}, ϕ_{re}) of the radiation vector are determined by

$$\phi_{re} = \tan^{-1} \frac{y_{re}}{x_{re}}$$

$$\theta_{re} = \tan^{-1} \frac{(x_{re}^2 + y_{re}^2)^{1/2}}{z_{re}} \qquad (65)$$

with the components X_{re}, Y_{re} and Z_{re} found through

$$\begin{bmatrix} X_{re} \\ Y_{re} \\ Z_{re} \end{bmatrix} = \begin{bmatrix} \cos\phi_o & \sin\phi_o & 0 \\ -\cos\theta_o\sin\phi_o & \cos\theta_o\cos\phi_o & \sin\theta_o \\ \sin\theta_o\sin\phi_o & -\sin\theta_o\cos\phi_o & \cos\theta_o \end{bmatrix}$$

$$\begin{bmatrix} \sin\theta_{ro}\cos\phi_{ro} \\ \sin\theta_{ro}\sin\phi_{ro} \\ \cos\theta_{ro} \end{bmatrix} \tag{66}$$

For the case where $\phi_o = 0°$ and $\theta_o = 90°$ as seen in Fig. 36, Eq. (66) reduces to

$$\begin{bmatrix} X_{re} \\ Y_{re} \\ Z_{re} \end{bmatrix} = \begin{bmatrix} 1 & 0 & 0 \\ 0 & 0 & 1 \\ 0 & -1 & 0 \end{bmatrix} \begin{bmatrix} \sin\theta_{ro}\cos\phi_{ro} \\ \sin\theta_{ro}\sin\phi_{ro} \\ \cos\theta_{ro} \end{bmatrix} \tag{67}$$

Finally, the radiated field in the desired radiation direction can be determined from the field found in the elevation plane model analysis with an appropriate polarization modification. Thus, the solution obtained can be incorporated into the roll plane cylinder solution to form a complete solution for the volumetric pattern.

Let us now consider the polarization effect due to the coordinate transformation, which is vital in achieving a complete solution. Recall that, in the far zone, the electric field can be written as

$$\overline{E} = E_\theta \hat{\theta} + E_\phi \hat{\phi} \tag{68}$$

or

$$\overline{E} = E_\theta' \hat{\theta}' + E_\phi' \hat{\phi}' \tag{69}$$

81
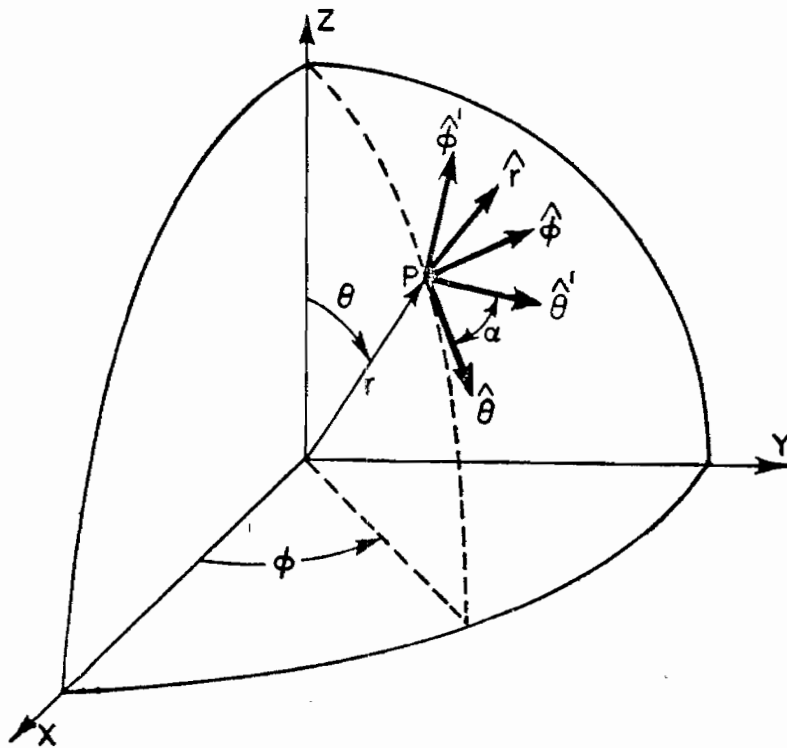
Figure 36. Illustration of the spherical
coordinate system.

where the prime system denotes the new coordinate system as seen
in Fig. 36. Since the components $E_\theta^!$ and $E_\phi^!$ are found from the
elevation plane solutions, the corresponding E_θ and E_ϕ in the
desired coordinate system are yet to be determined. If one
takes the dot product of Eq. (69) with the unit vector θ, the
θ component of the electric field results, i.e.

$$E_\theta = E_\theta^! \; (\hat{\theta}' \cdot \hat{\theta}) + E_\phi^! \; (\hat{\phi}' \cdot \hat{\theta}) \tag{70}$$

Similarly, the ϕ component can be found as

$$E_\phi = E_\theta^! \; (\hat{\theta}' \cdot \hat{\phi}) + E_\phi^! \; (\hat{\phi}' \cdot \hat{\phi}) \tag{71}$$

82

Thus, the polarization of the radiated field in terms of the reference coordinate system can be properly determined.

Before the roll and elevation plane model solutions can be combined together, one must be concerned with the alignment of the surface normal at the antenna location in the two analyses. For an antenna mounted centrally on the fuselage, the surface normal points vertically upwards in the roll plane model analysis; whereas, in the elevation plane model it points in a direction normal to the profile surface at the antenna location. If the normals do not align properly, the two solutions would not match to give a complete and continuous solution. Consequently, the roll plane elliptic cylinder needs a tilt such that the normal direction is common to both solutions. It is noted that a radial monopole is mounted parallel to the surface normal at the antenna location on the aircraft fuselage.

To accomplish this alignment, the X_{roll} axis of the roll plane model coordinate system is chosen to line up parallel with the normal to the surface at the antenna location on the elevation composite elliptic cylinder as shown in Fig. 34. The tilt angle θ_{tilt} is found to be

$$
\theta_{tilt} = \begin{cases}
\tan^{-1}\left(\dfrac{a_e^2 \, Z_{s \, ref}}{b_e^2 \, X_{s \, ref}} \right) & \text{if } Z_{s \, ref} \text{ is negative} \\[2em]
\tan^{-1}\left(\dfrac{a_e^2 \, Z_{s \, ref}}{b_e'^2 \, X_{s \, ref}} \right) & \text{if } Z_{s \, ref} \text{ is positive}
\end{cases}
\tag{72}
$$

where $X_{s \, ref}$ and $Z_{s \, ref}$ are the coordinates of the antenna source relative to the reference coordinate system. The quantities a_e, b_e, and b_e' are the necessary parameters for the composite elliptic cylinder model for the elevation plane model analysis. Notice that the origin of the roll plane cylinders is located a distance a_r directly under the antenna. Again, the quantity a_r represents an axis of the roll plane cylinder.

It is also noted that, the parameter a_r is not equal to $X_{s \, ref}$ which is the height of the antenna on the elevation composite cylinder model. This is due to the fact that the two elliptic cylinders used to approximate the fuselage profile and cross section do not match to give the true representation

83

of a three-dimensional aircraft fuselage. Hence, to obtain the
necessary roll plane model solution, a coordinate transformation
similar to that of the elevation plane model analysis described
above is needed. The required rotation angle (θ_0, ϕ_0) of the roll
plane model coordinate system is found to be

$$\theta_0 = \theta_{tilt}$$

$$\phi_0 = 0 \tag{73}$$

for a centrally mounted antenna. Since the θ_{tilt} angle is
rotated about the y'-axis, Eqs. (80) and (85) shall be used.

One last note for the completion of our solution is the
phase reference problem. For both elevation and roll plane model
analyses, the origin of the individual coordinate system is
chosen to be the phase reference point. Hence, the result
obtained through these two principal plane model analyses needs to
be modified so that a common phase center can be utilized. For
convenience, the origin of the reference coordinate system is
selected as the phase reference point for both models. In this
way, the solutions blend smoothly together to form a complete
result for the three-dimensional geometry under consideration.

For each of the two solutions just described, only two
rays are considered. This is due to the fact that there are
only two dominant rays which propagate around an electrically
large elliptic cylinder. Recall that four dominant rays
contribute to the radiation pattern in the shadow region for an
antenna mounted on a prolate spheriod. To account for these
four rays necessary for the radiation pattern in the shadow
region, both elevation and roll plane model results are needed
in the pattern calculation.

In addition, the three-dimensional effects of wings and
stabilizers are considered by including the rays reflected and
diffracted from these scatterers. The contribution of wings
and horizontal stabilizers are handled in the same way as done
previously.

The effect of the cockpit/radome section is determined
using flat plates attached to the fuselage just as the wings.
Since computation time in analyzing a real cockpit radome
section is so great, it is apparent that a simple model is needed.
Originally, a finite bent plate approximation of the cockpit and
nose section was considered because of an experimental investigation
of the radome. This resulted in a truncated fuselage model as

discussed in Reference [31]. However, the radiation pattern cal-
culated using a flat plate model compared very favorably with the
bent plate model. Hence, the flat plate model was adopted not
only for its simplicity in analysis but, also, for its reduced
computer running time. Notice that the plate is mounted at
arbitrary angles relative to the cylinder to simulate the cockpit/
radome section as seen in Fig. 34 (a). This is an improvement
over the previous roll plane model where the wings are restricted
to be horizontal.

Similar considerations were made in studying the vertical
stabilizer which resulted in the selection of a bent plate
model. Thus, the scattering effects of the cockpit and vertical
stabilizer can be taken into account very simply. The theoretical
model as shown in Fig. 34 (a) is an illustration of the analytical
simulation of an actual aircraft. With all the necessary mechanisms
being completed, the radiation and scattering by the fuselage, wings,
cockpit, and stabilizers can now be calculated. Finally, the
volumetric pattern of a fuselage mounted antenna is obtained
by summing the direct field from the source and the reflected
and diffracted field from the various scatters.

Before it can be used to determine the volumetric pattern
for an airborne antenna, this newly developed solution must be
tested and verified. The elevation pattern of an axial slot
mounted on a prolate spheroid, thus, was calculated and is
presented in Fig. 37. The comparison between the measured and
calculated results is very persuasive. This particular problem
is an effective test in that it illustrates the accuracy for
the limiting case of a small nearly spherical object as opposed
to the large cylindrical aircraft model.

To illustrate the validity of the new solution, the principal
plane radiation patterns of antennas mounted on the KC135 aircraft
that was previously computed are now computed with the improved
solution. With the cockpit/radome and vertical stabilizer being
taken into account, the new computer model, consisting of an 80"
by 3.75" right semi-ellipse and an 8" by 3.75" left semi-ellipse,
is shown in Fig. 38. The cockpit/radome section is simulated
by a flat plate and the vertical stabilizer is approximated by a
bent plate model for better simulation. The elevation plane
patterns for a short monopole mounted forward and over the wings
are shown in Figs. 39 (a) and (b), respectively. The patterns
for a circumferential KA-band waveguide are shown in Figs. 40 (a)
and (b). The results for an axial KA-band waveguid are depicted
in Figs. 41 (a) and (b). It is observed that the comparison
between the calculated and measured results is very favorable.
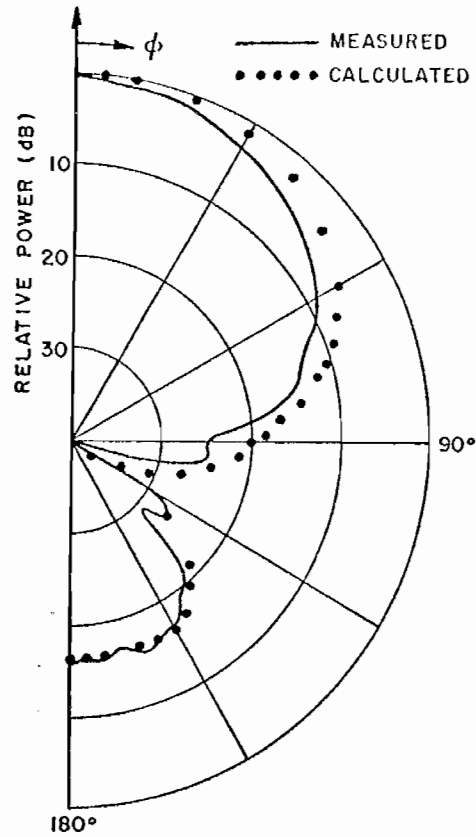
Figure 37a. Elevation plane pattern of an axial slot mounted on a 4λ x 2λ prolate spheroid using the surface of revolution approach. (Geometry illustrated in Fig. 30).
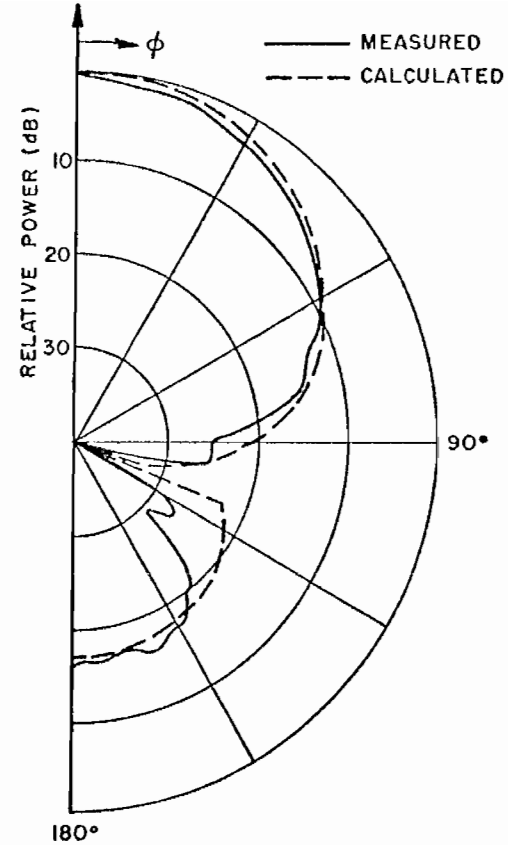
Figure 37b. Elevation plane pattern of an axial slot mounted on a 4λ x 2λ prolate spheroid using newly developed volumetric solution. (Geometry illustrated in Fig. 30).

BENT PLATE
VERTICAL
STABILIZER

ANTENNA

O

FLAT PLATE
NOSE
SECTION

FLAT
WING
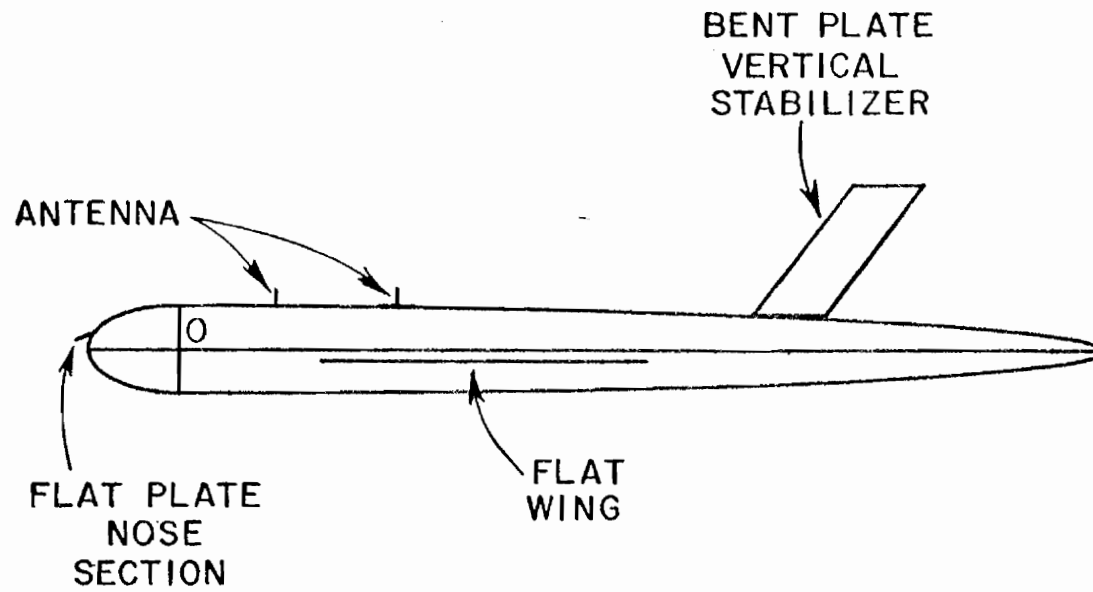
Figure 38a. Computer simulated model for the fuselage profile of a KC-135
aircraft (side view).
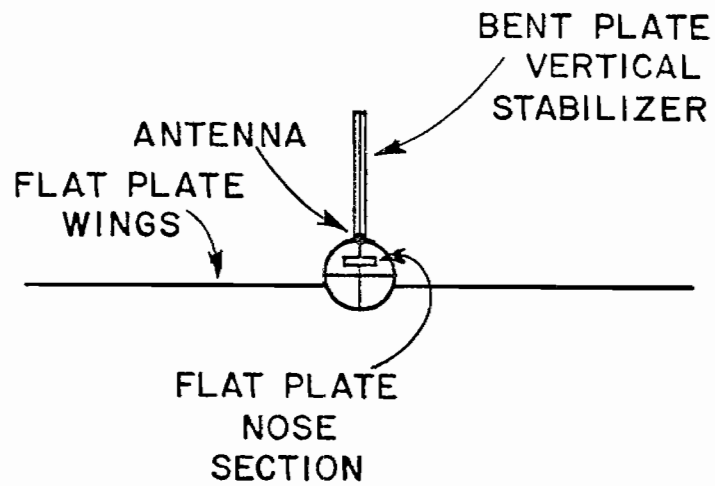
Figure 38b. Computer simulated model for the cross-section (at antenna location) of a KC-135 aircraft (front view).

ANTENNA

BENT PLATE
VERTICAL
STABILIZER

FLAT PLATE
NOSE
SECTION

ROLL PLANE
CYLINDER
CROSS SECTION

FLAT PLATE
WING
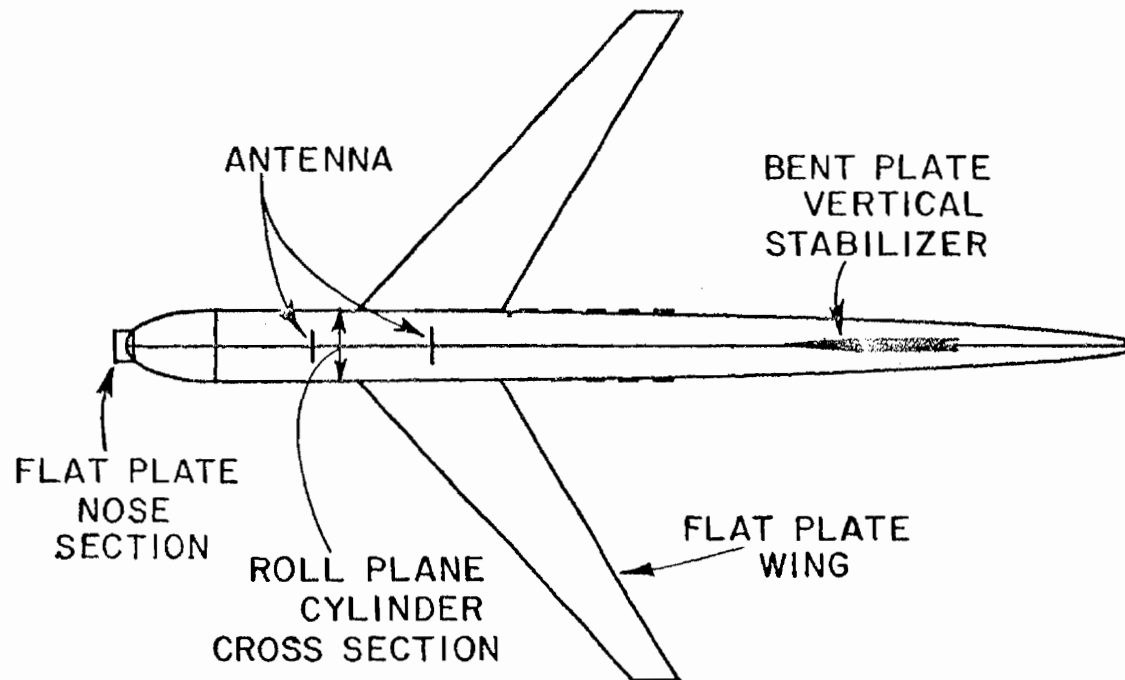
Figure 38c.   Computer simulated model for a KC-135 aircraft (top view).
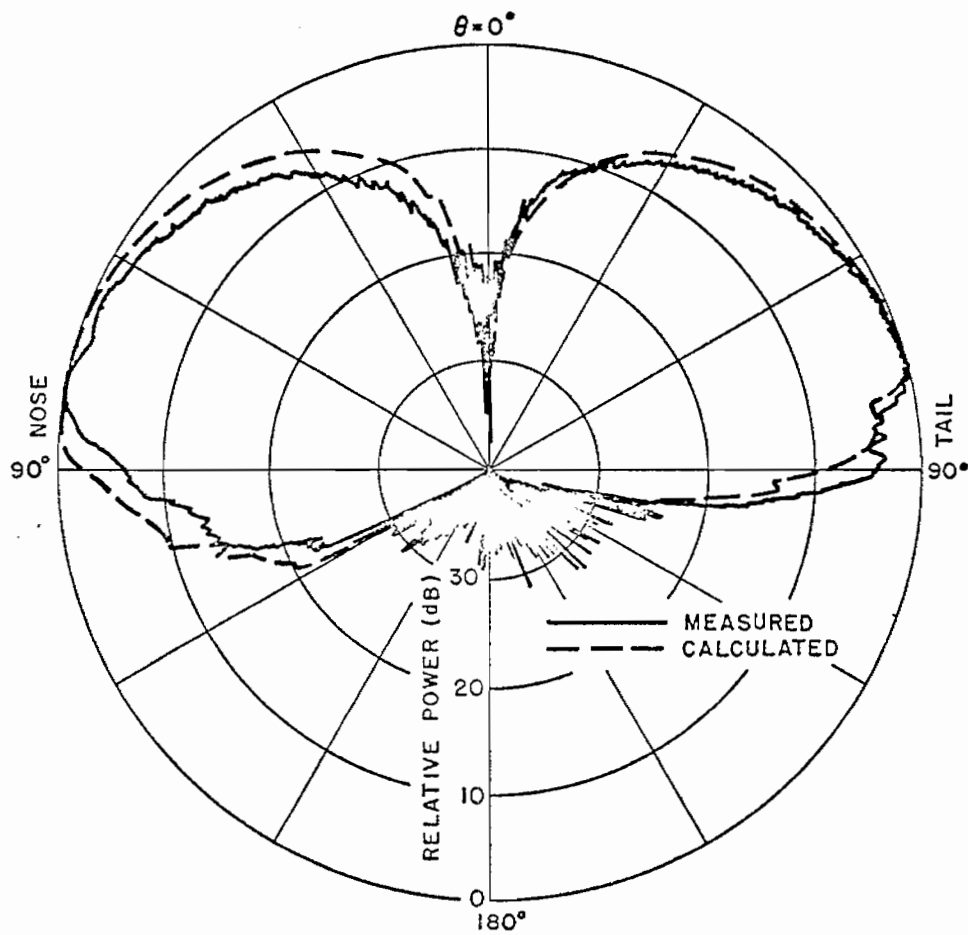
Figure 39a. Elevation plane pattern for a λ/4 monopole
mounted forward of the wings on a KC-135
aircraft (with radome and vertical stabilizer
included).

90

Figure 39b. Elevation plane pattern for a $\lambda/4$ monopole
mounted above the wings on a KC-135 aircraft
(with radome and vertical stabilizer included).
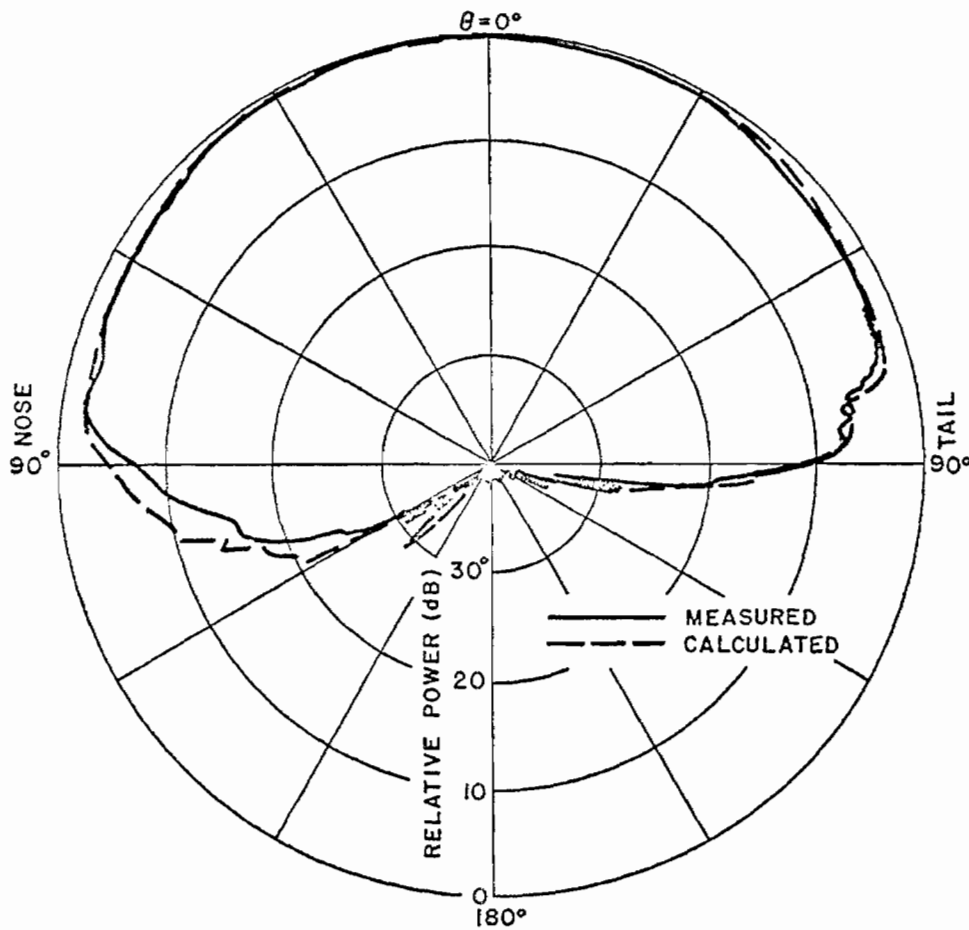
Figure 40a. Elevation plane pattern for a circumferential KA-band waveguide mounted <u>forward</u> of the wings on a KC-135 aircraft (with radome and vertical stabilizer included).
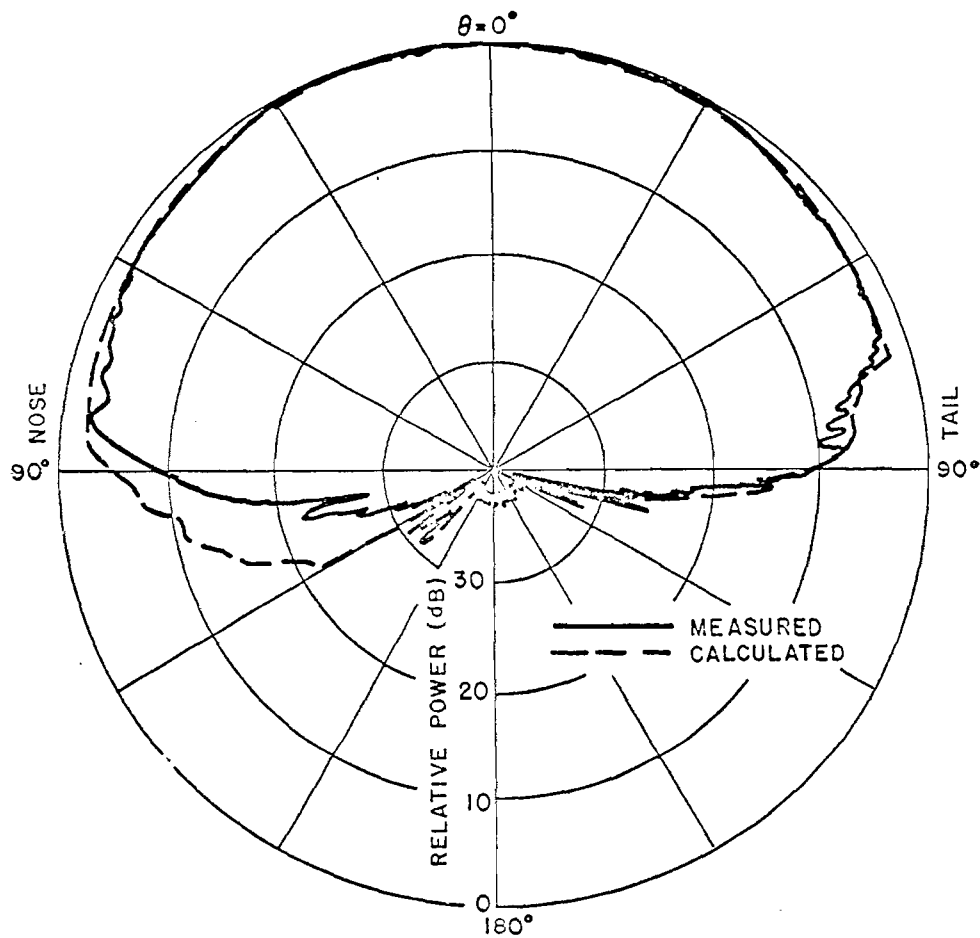
Figure 40b. Elevation plane pattern for a circumferential KA-band waveguide mounted above the wings on a KC-135 aircraft (with radome and vertical stabilizer included).
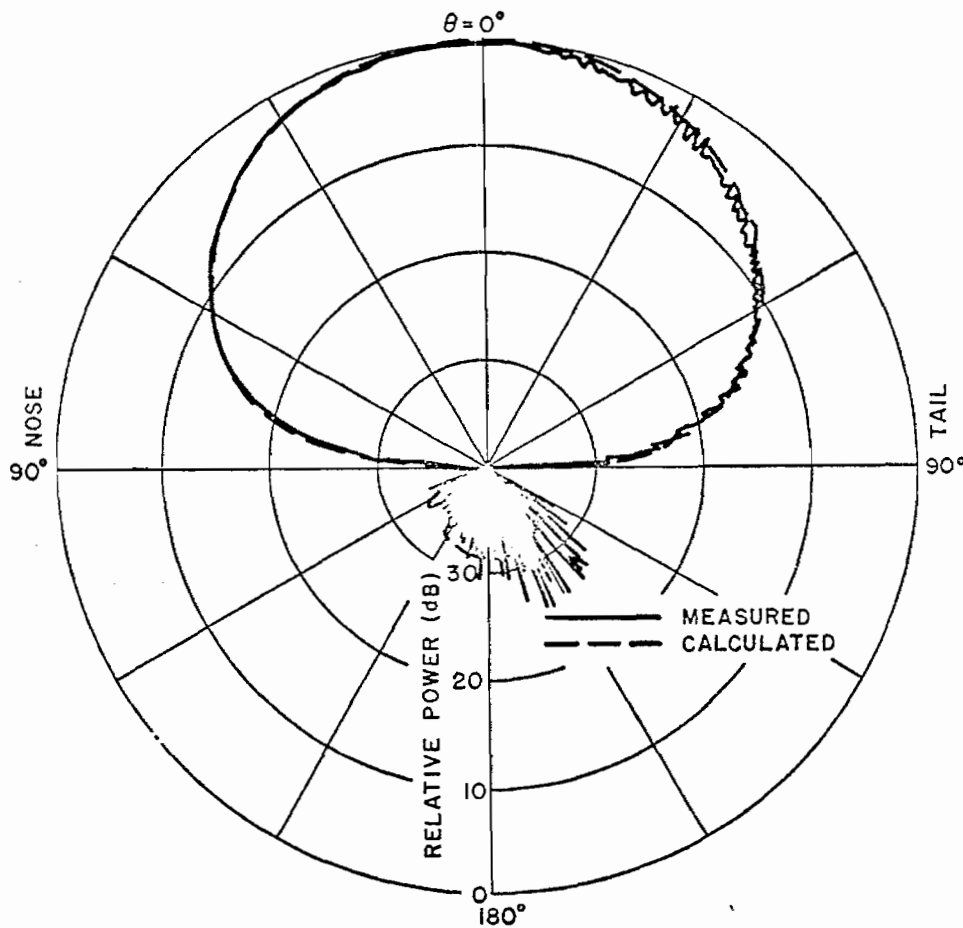
Figure 41a. Elevation plane pattern for an axial KA-band
waveguide mounted forward of the wings on a
KC-135 aircraft (with radome and vertical
stabilizer included).
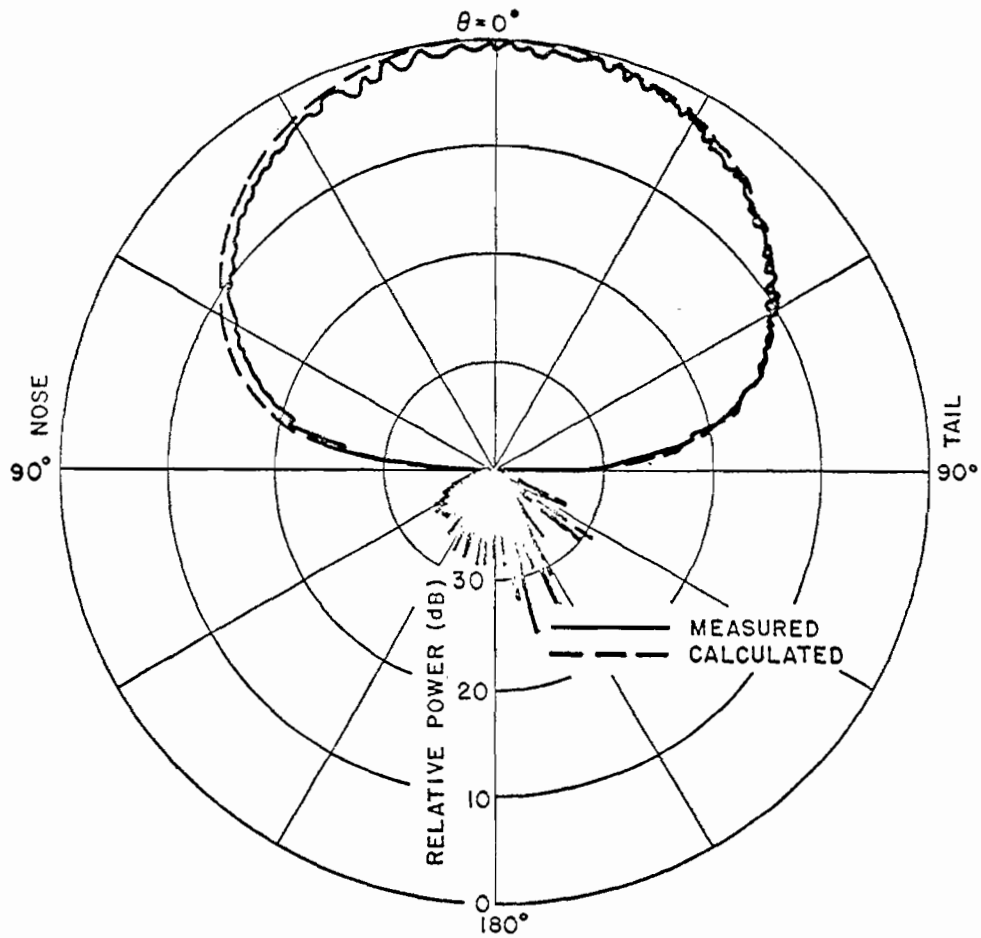
Figure 41b. Elevation plane pattern for an axial KA-band waveguide mounted <u>above</u> the wings on a KC-135 aircraft (with radome and vertical stabilizer included).

The discrepancy displayed in aft sectors in Figs. 14 and 15 no longer exist in Figs. 39 and 40. For axial slot cases, the back lobe is picked up as compared with previous results. Notice that the nulls of the monopole for the theory and measurement do not align together as one can see in Figs. 39 (a) and (b). This can be attributed to some extent to the misalignment of the monopole and surface normal in the experimental work.

Finally, the roll plane radiation patterns for the new model are calculated. In each case, the pattern is only slightly improved over previously calculated results as shown in Figs. 27 and 29. This is attributed to the fact that the surface rays contribution from the elevation plane model is negligible in the plane of interest. In any event, these results demonstrate the validity and applicability of the new solution in determining the radiation patterns for general fuselage mounted antennas.

To further demonstrate the versatility of this solution, the radiation pattern for an infinitesimal monopole mounted on the bottom of the fuselage of a Boeing 737 with a dielectric radome is calculated. The model for this case is shown in Fig. 42 where the radome effect is simulated by a flat plate mounted vertically upward. This model is adopted because of the similar consideration as discussed previously. Even though double diffractions are not included in the calculation, the resultant pattern is still in very good agreement with the measured result as shown in Fig. 43. This, again, illustrates the capability of the solution in predicting the radiation pattern of fuselage mounted aircraft antennas.

FLAT
PLATE

RADOME

X_{ref}

$a = 64.66"$
$b = 232.52"$
$b' = 1200"$
$Z_s = 144.6"$

a

Z_{ref}

b

b'

Z_s

186.97"

ANTENNA
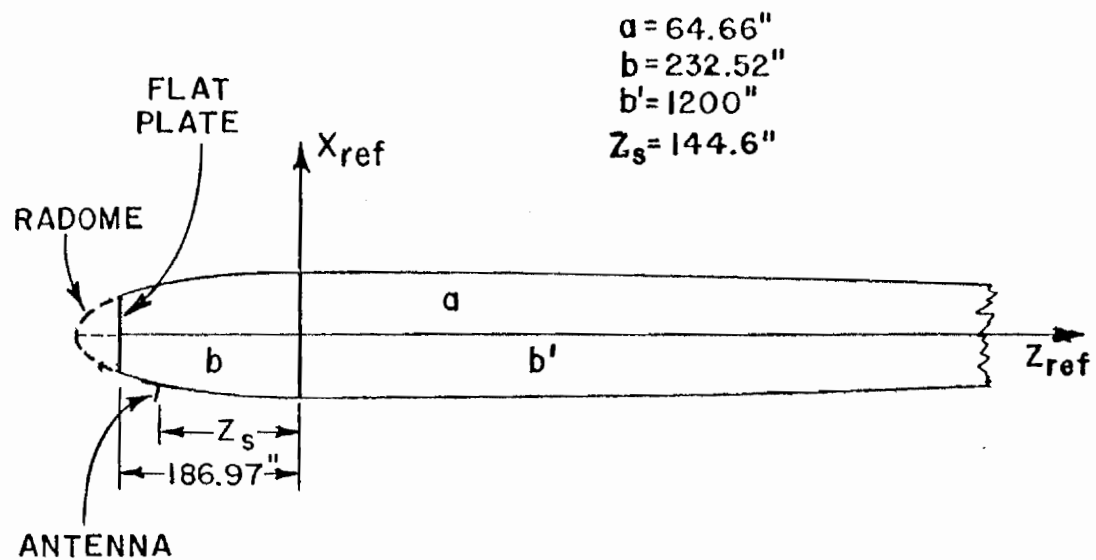
Figure 42. Computer simulated model for a $\lambda/4$ monopole mounted at station 222 on the bottom of the fuselage of a Boeing 737 aircraft (with radome/ nose section being modelled by a flat plate).
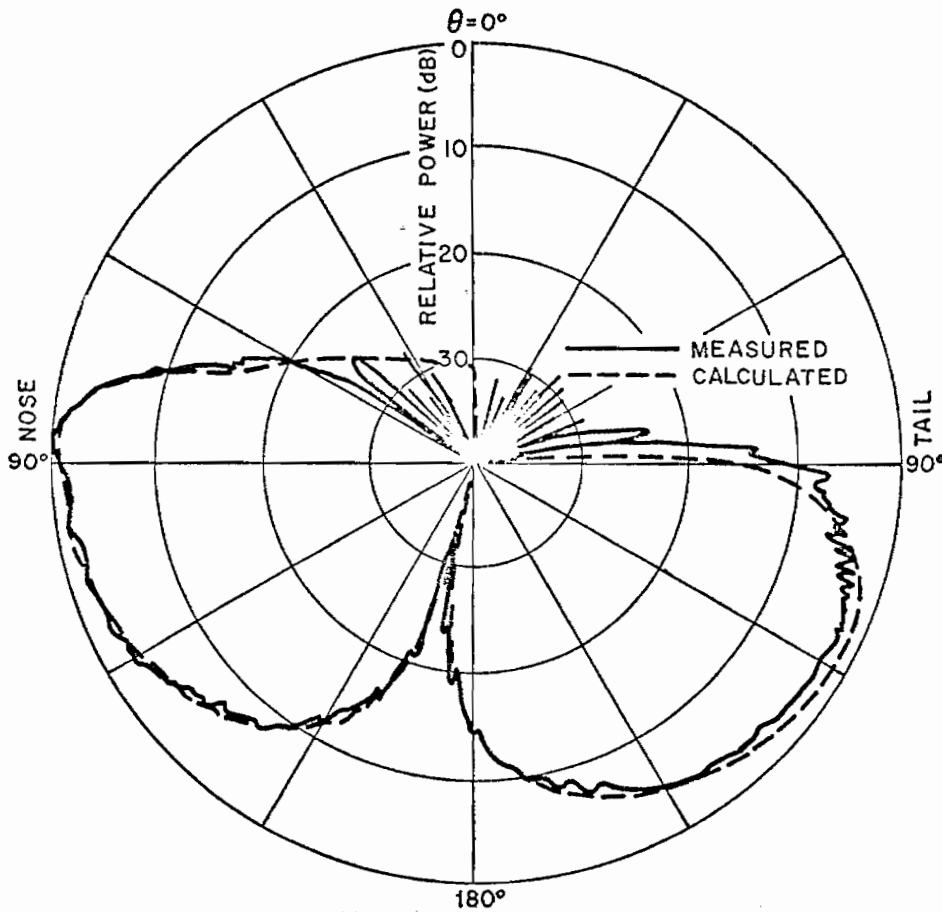
Figure 43. Elevation plane pattern of a λ/4 monopole mounted at station 222 on the bottom of a Boeing 737 aircraft. (φ = 0° at the left; φ = 180° at the right).

98

SECTION IV

VOLUMETRIC PATTERNS OF AIRBORNE ANTENNAS

The theoretical approach to analyze the complete volumetric radiation pattern of fuselage mounted antennas was developed in the last section. This theoretical solution was based on the two ·principal plane analyses presented earlier and it has been verified by applying it to various cases previously calculated using principal plane analyses. The results show great improvement over previous calculations based on comparisons with experimental measurements. Hence, the new volumetric solution is now applied to analyze the volumetric patterns of fuselage mounted airborne antennas.

The aircraft model of most interest in our study is the Boeing 737 aircraft in that extensive experimental work is available. The volumetric patterns of this aircraft model is examined in this section.

The models used to simulate a Boeing 737 aircraft are shown in Fig. 44, where the roll plane cross-section of the fuselage is approximated by a 65.86" by 43.3" elliptic cylinder for an antenna mounted at Station 220 on the top of the fuselage. The elevation profile is modeled by a composite elliptic cylinder with a = 48.72", b = 308.56", and b' = 1307.04". Notice that the cockpit nose section and vertical stabilizer are approximated by finite flat and bent plates mounted obliquely on the fuselage which results in a simple model for our aircraft as shown in Fig. 44.

In Fig. 44(c), the top view of our model is shown to illustrate the finite three-dimensional effect of an aircraft. The dotted line indicates the width of the cross-sectional (roll plane) cylinder used in the calculations. The models of the wings, cockpit nose section, and stabilizers are also presented. The geometry is taken directly from the three principal views of the aircraft scale model. As presented earlier, the coordinate systems used for both the elevation and roll plane geometries are depicted in Fig. 44.

The radiation patterns for a λ/4 monopole mounted at Station 220 above the cockpit on a Boeing 737 aircraft are, then, calculated using the model just described with the analysis presented in the last section. The three principal plane results are shown in Figs. 45 to 47 and found to be in
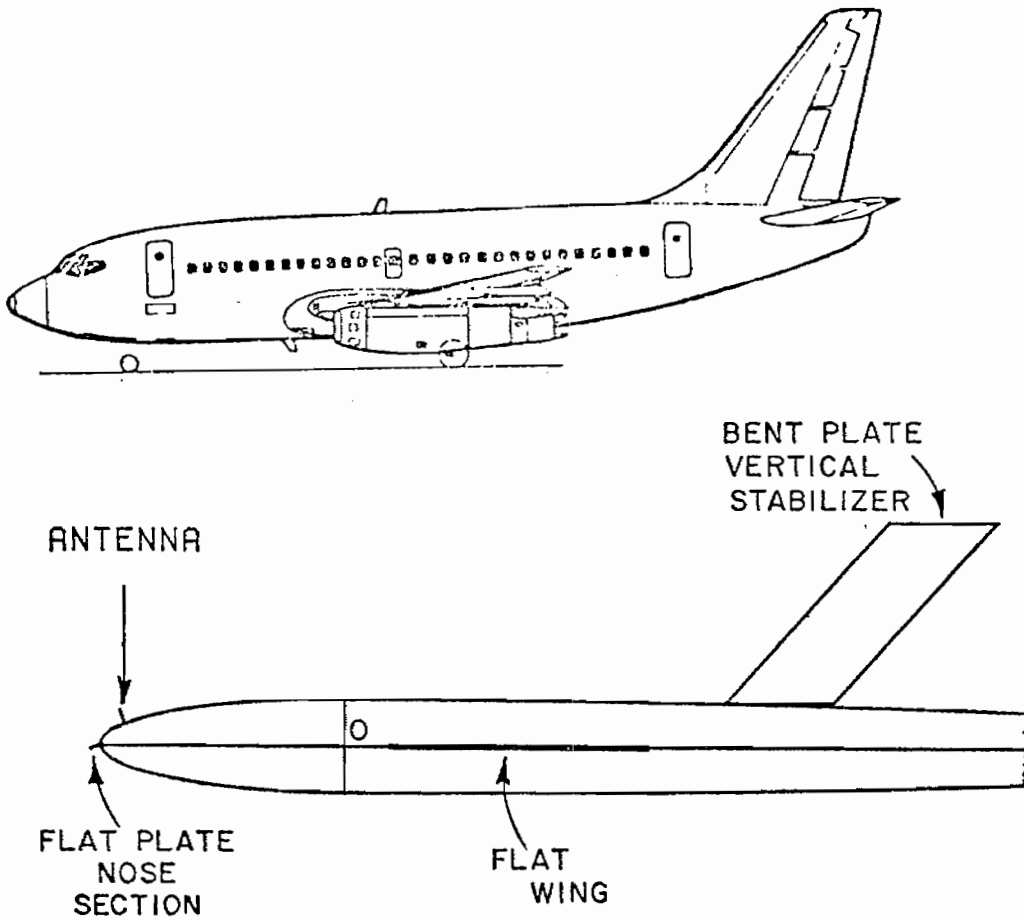
Figure 44a. Computer simulated model for the fuselage profile
of a Boeing 737 aircraft (side view). The antenna
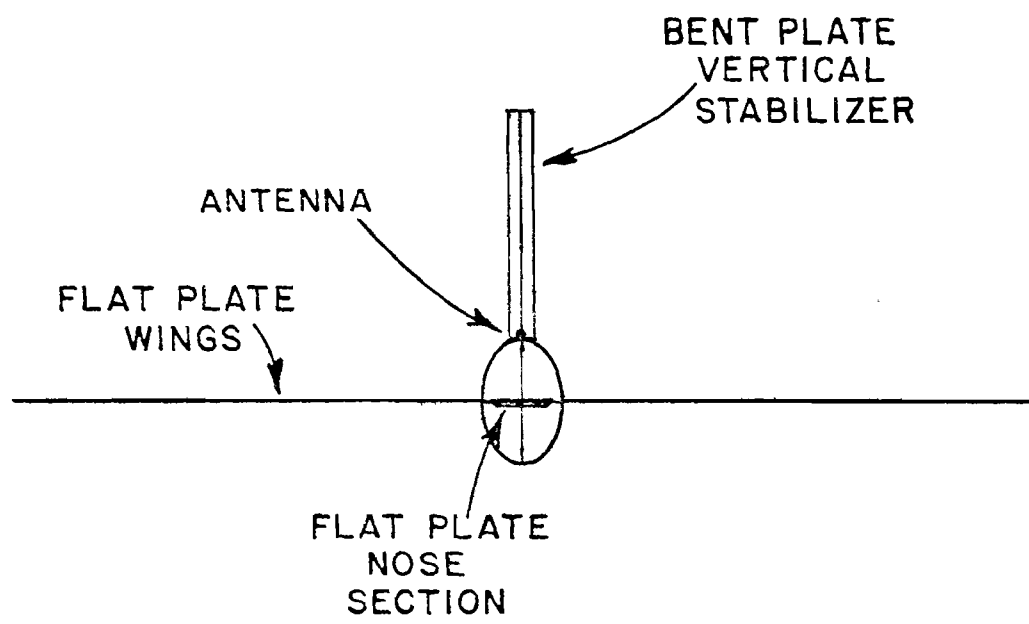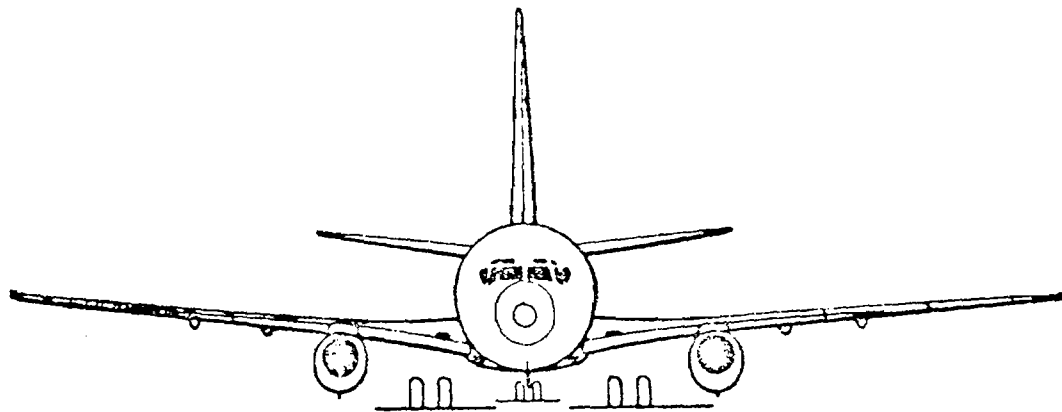is located at station 220 on top of the fuselage.

Figure 44b. Computer simulated model for the cross section (at antenna location) of a Boeing 737 aircraft (front view). The antenna is located at station 220 on top of the fuselage.
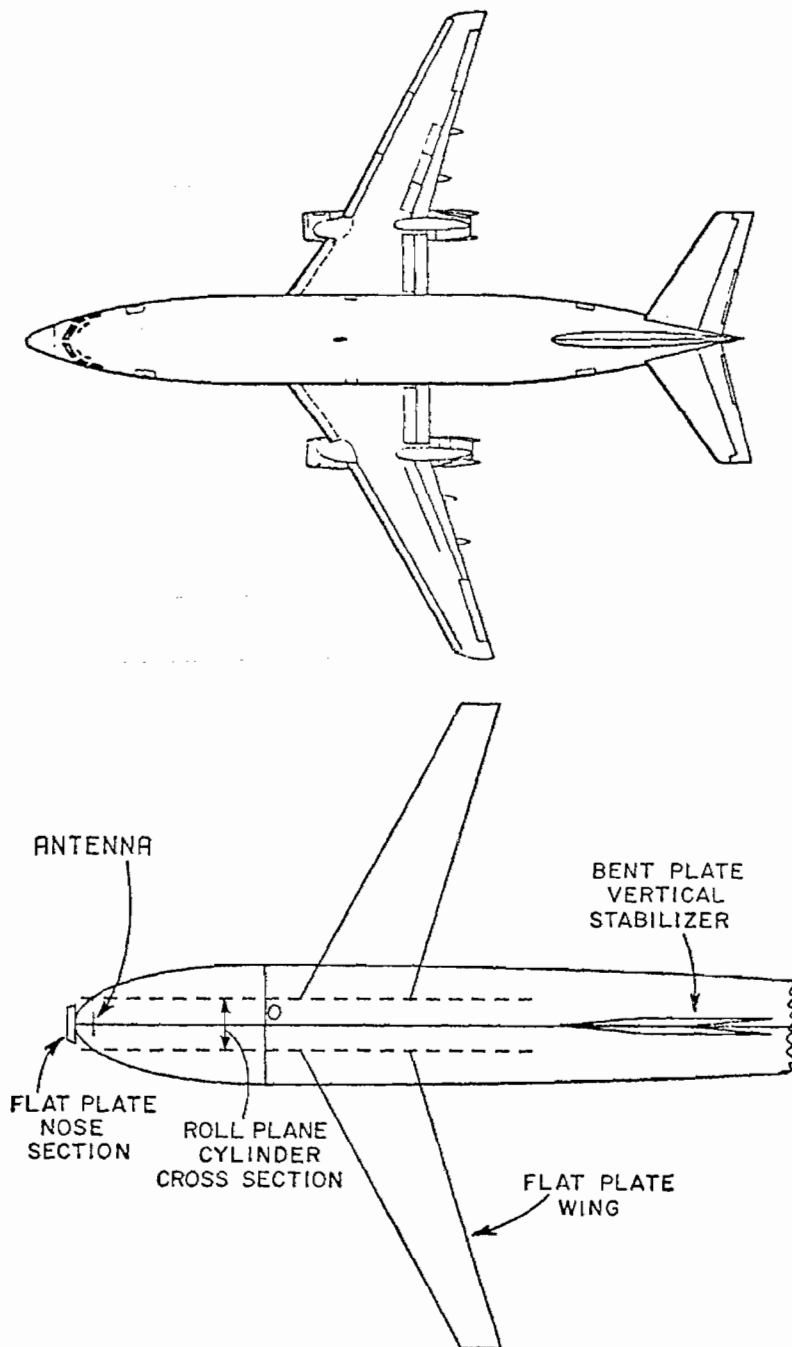
Figure 44c. Computer simulated model for a Boeing 737 aircraft
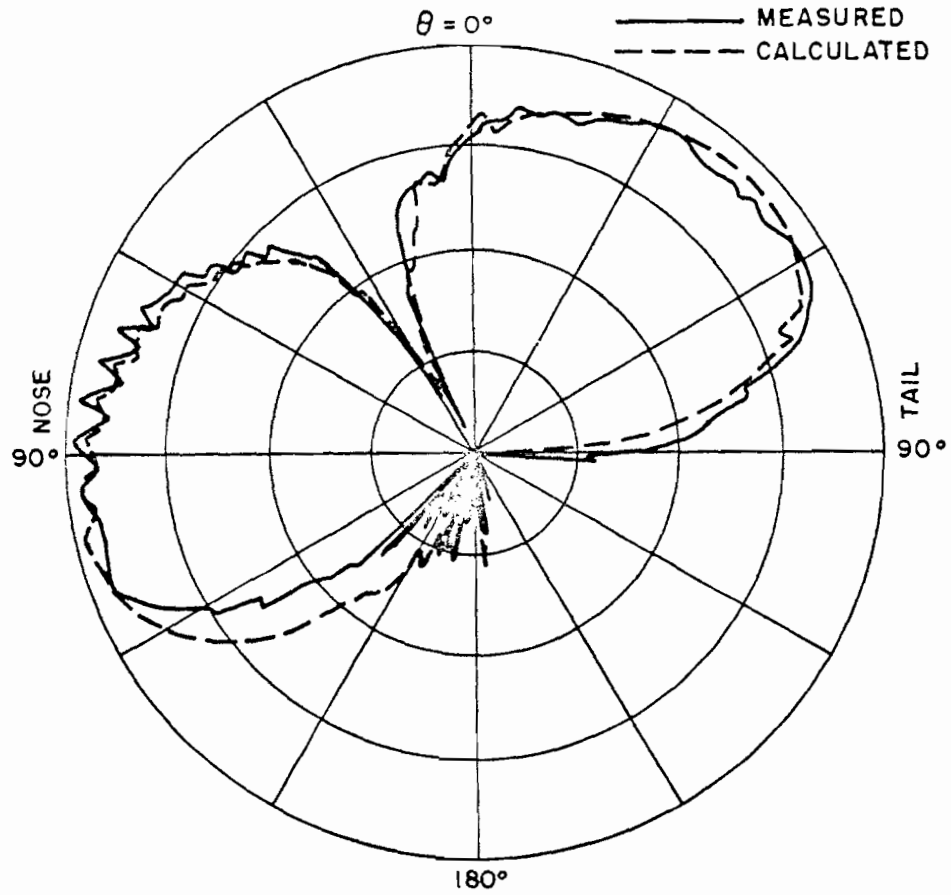(top view). The antenna is located at station 220
on top of the fuselage.

102

Figure 45. Elevation plane pattern of a $\lambda/4$ monopole mounted at station 220 on top of a Boeing 737 aircraft. ($\phi = 0°$ at the left; $\phi = 180°$ at the right).
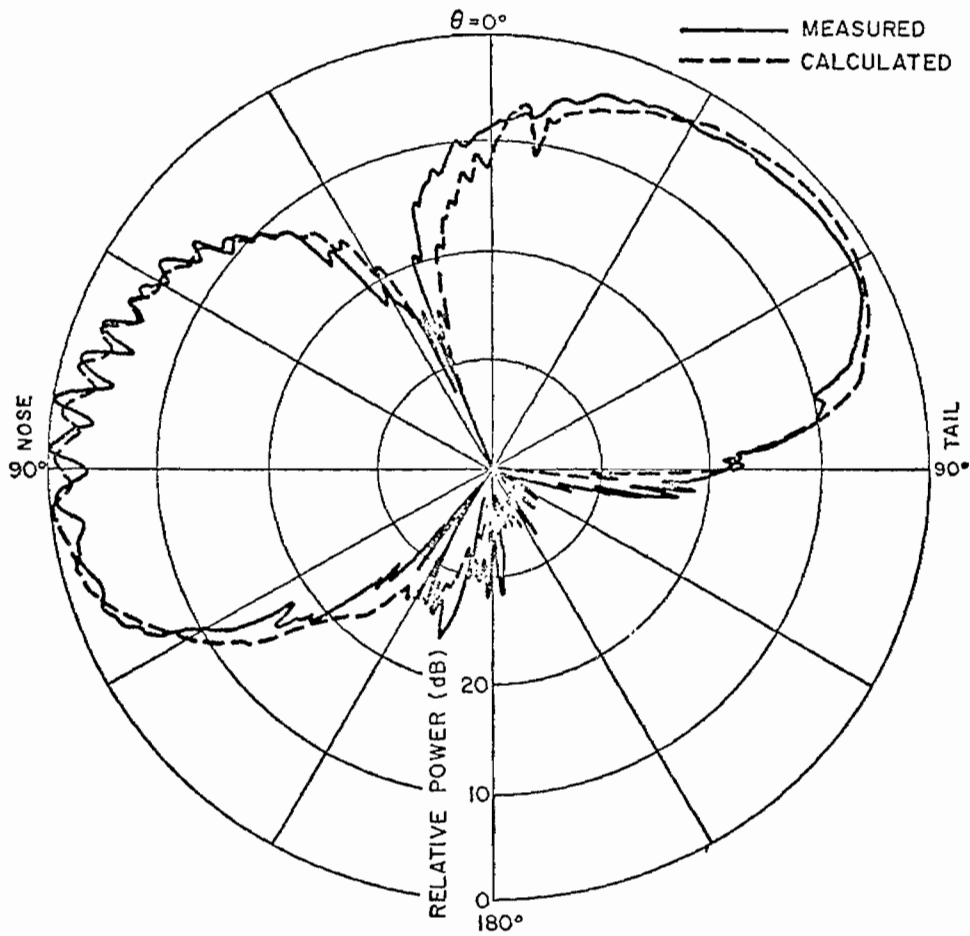
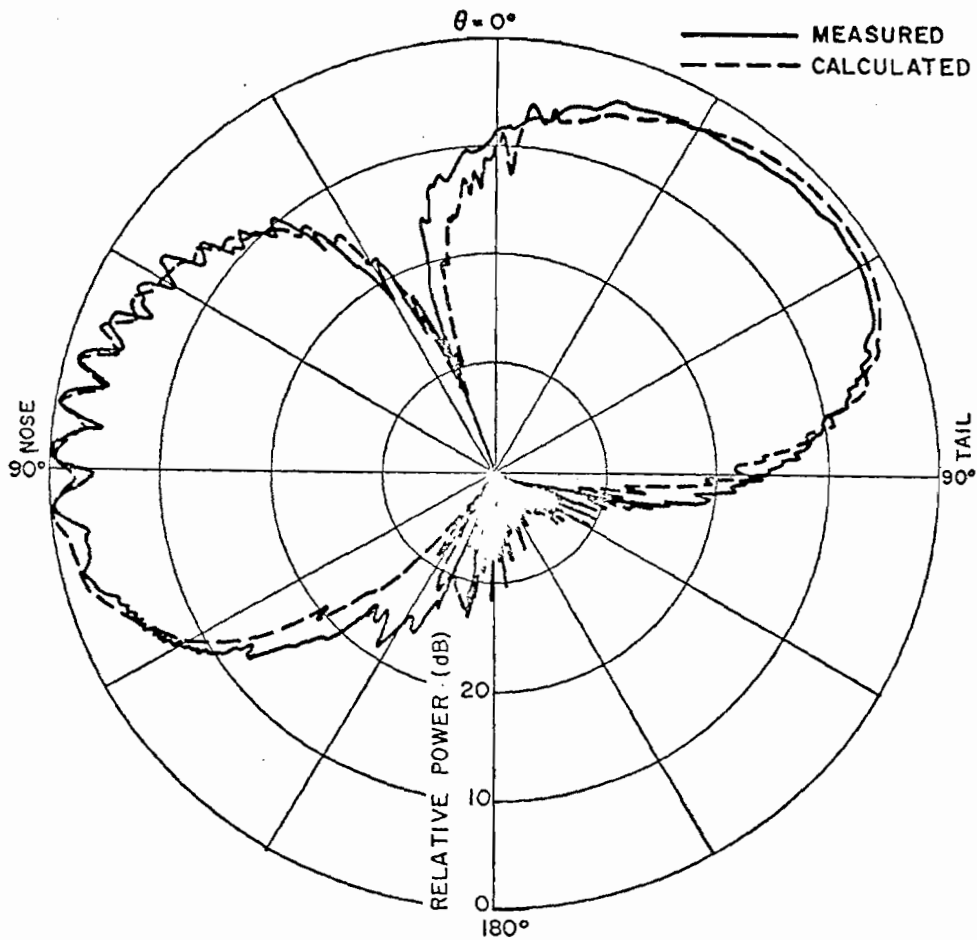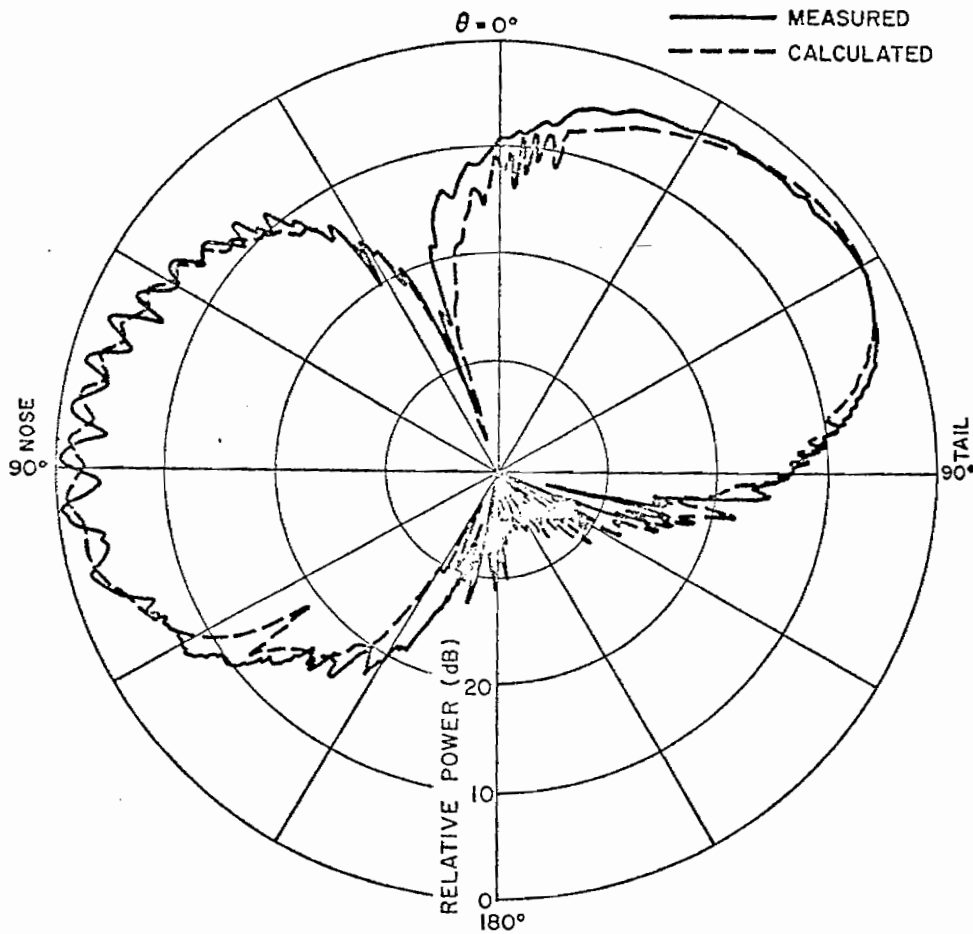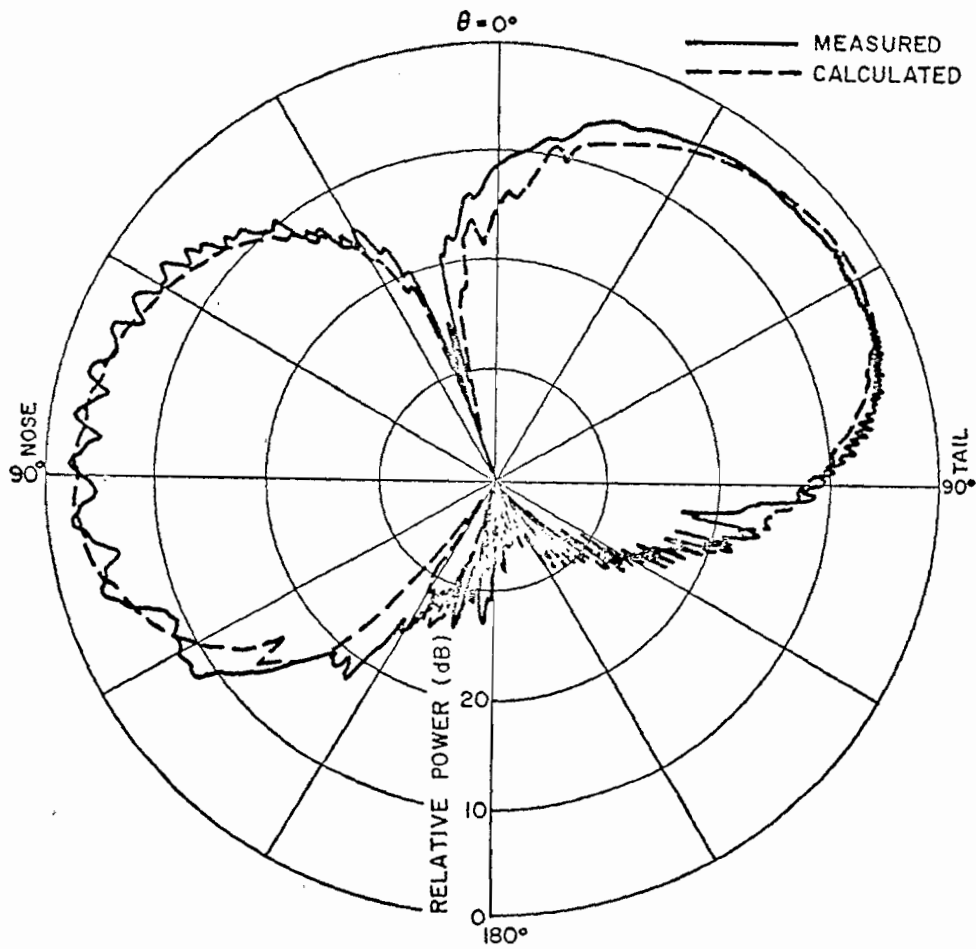Figure 46. Roll plane pattern of a λ/4 monopole mounted at
station 220 on top of a Boeing 737 aircraft.
(φ = 90° at the left; φ = 270° at the right).
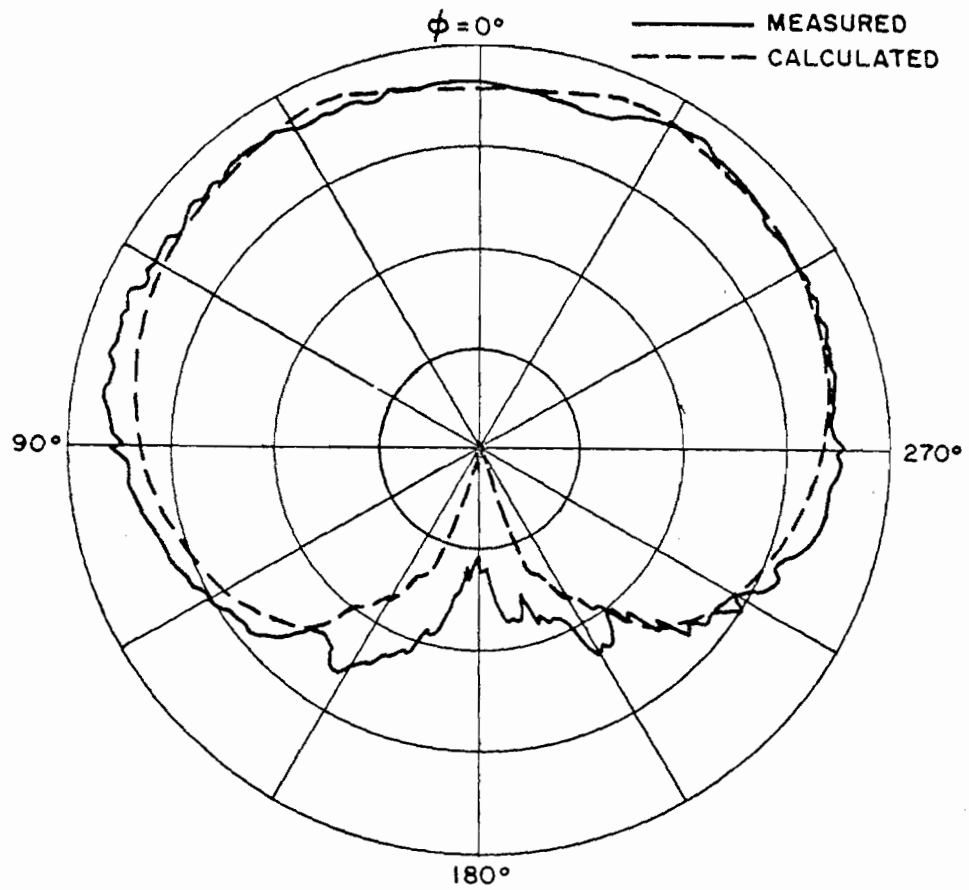
Figure 47. Azimuth plane pattern of a λ/4 monopole mounted at station on top of a Boeing 737 aircraft. (θ = 92°).

very good agreement with measurements. The experimental work
was performed with a great deal of patience and precision by
the technical staff at NASA (Hampton, Va.), using a 1/11th
scale model of Boeing 737 aircraft.

The coordinate system used for the experimental measurements
is shown in Fig. 48, in which the z-axis is vertically upward.
In order to calculate a radiation pattern in terms of this
experimental coordinate system, a transformation of coordinates
is necessary so that the corresponding radiation direction in
the analytical aircraft reference coordinate system can be
determined. This is accomplished by considering the z-axis of
the experimental coordinate system as a radial vector in the
reference coordinate system. By inputting its spherical coordin-
ates ($\theta_{Z_{ref}}$ = 90°, $\phi_{Z_{ref}}$ = 0°) as the rotation angles θ_c and ϕ_c
required in the computer program, the corresponding radiation
direction, in terms of the reference coordinate system, is
obtained.
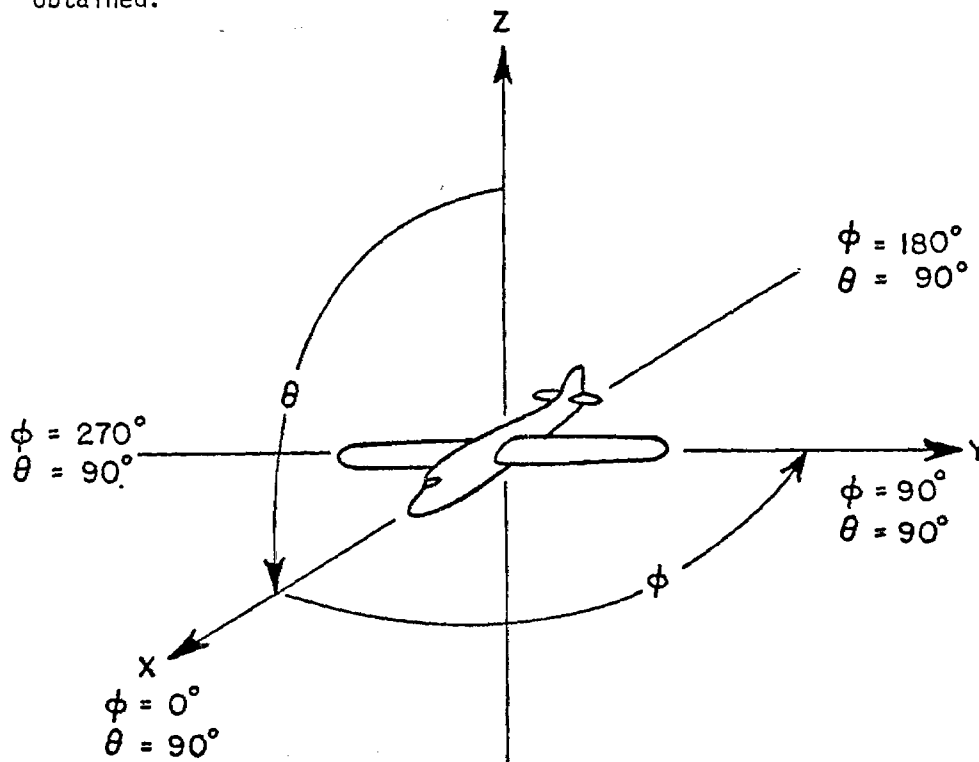
Figure 48. Illustration of the coordinate system used for
experimental measurements.

106

The complete volumetric pattern for a λ/4 monopole located
at Station 220 on top of a Boeing 737 aircraft is calculated.
The off-principal plane elevation patterns are shown in Figs.
49 to 52. The azimuth plane patterns are shown in Figs. 53 to
60. In each case, the calculated results compare very favorably
with the measurement. It is noted that the measurement results
have some asymmetry in the patterns. This could be attributed to
misalignment of the monopole with respect to the surface normal
or the movement of the model due to shifting weight during the
measurement.

Figure 49. Elevation plane pattern of a λ/4 monopole mounted at station 220 on top of a Boeing 737 aircraft. (φ = 10° at the left; φ = 190° at the right).

Figure 50. Elevation plane pattern of a λ/4 monopole mounted at station 220 on top of a Boeing 737 aircraft. (φ = 20° at the left; φ = 200° at the right).

Figure 51. Elevation plane pattern of a λ/4 monopole mounted
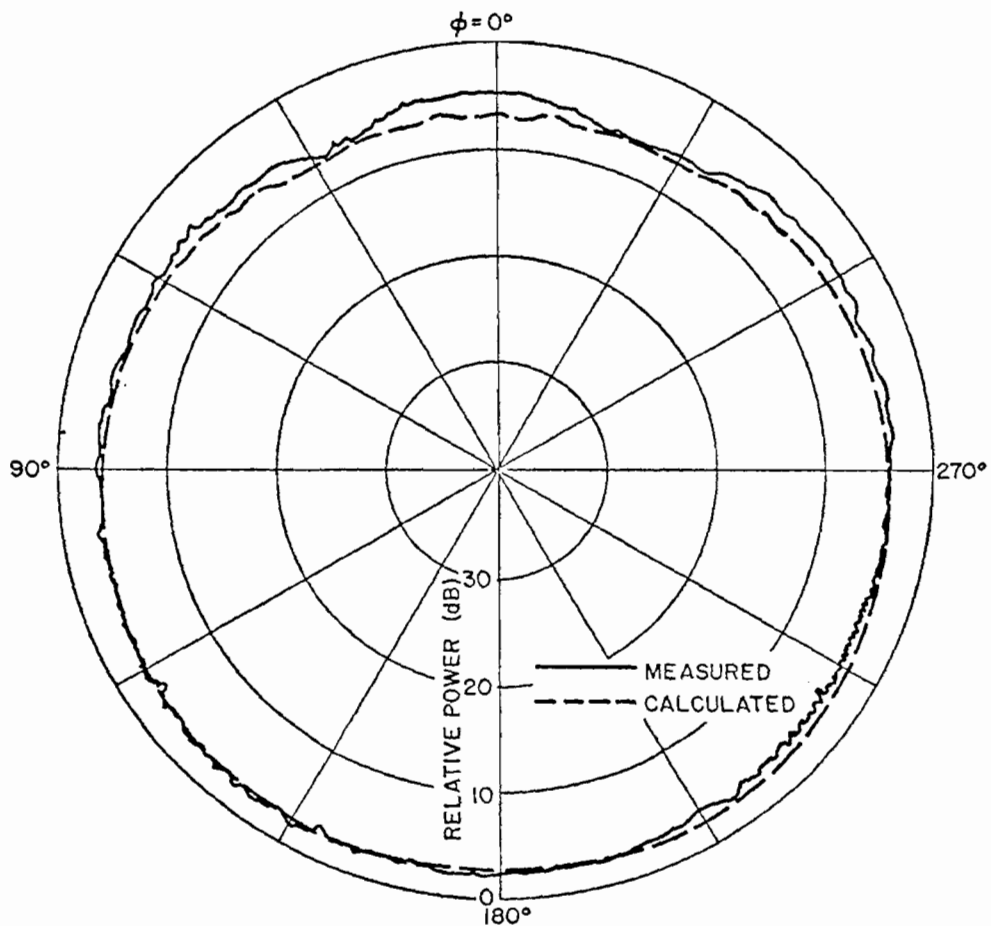at station 220 on top of a Boeing 737 aircraft.
(φ = 30° at the left; φ = 210° at the right).

110

Figure 52. Elevation plane pattern of a λ/4 monopole mounted
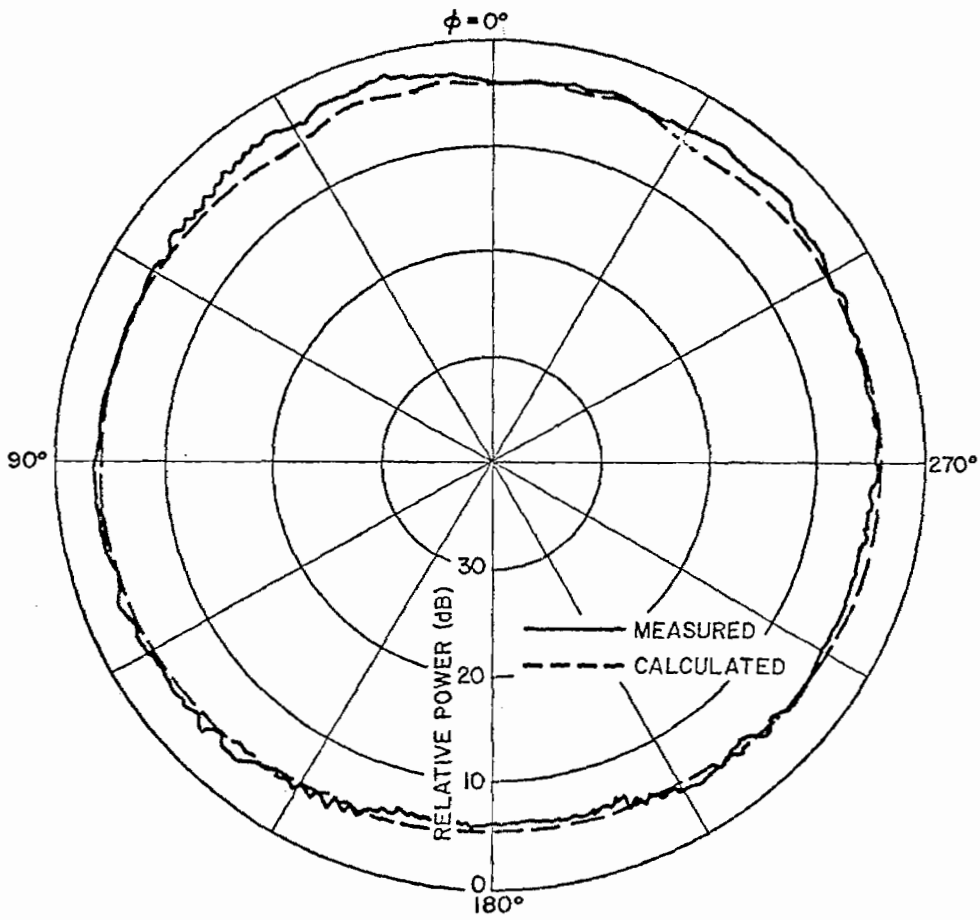at station 220 on top of a Boeing 737 aircraft.
(φ = 40° at the left; φ = 220° at the right).

111
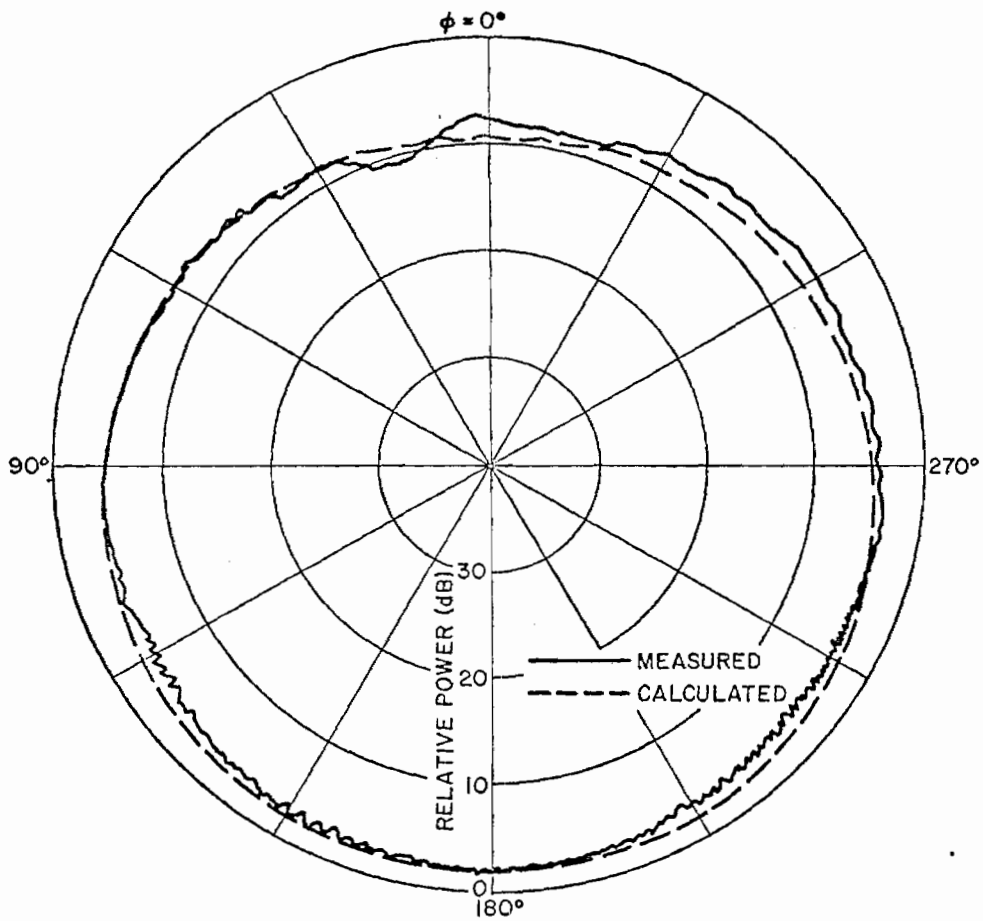
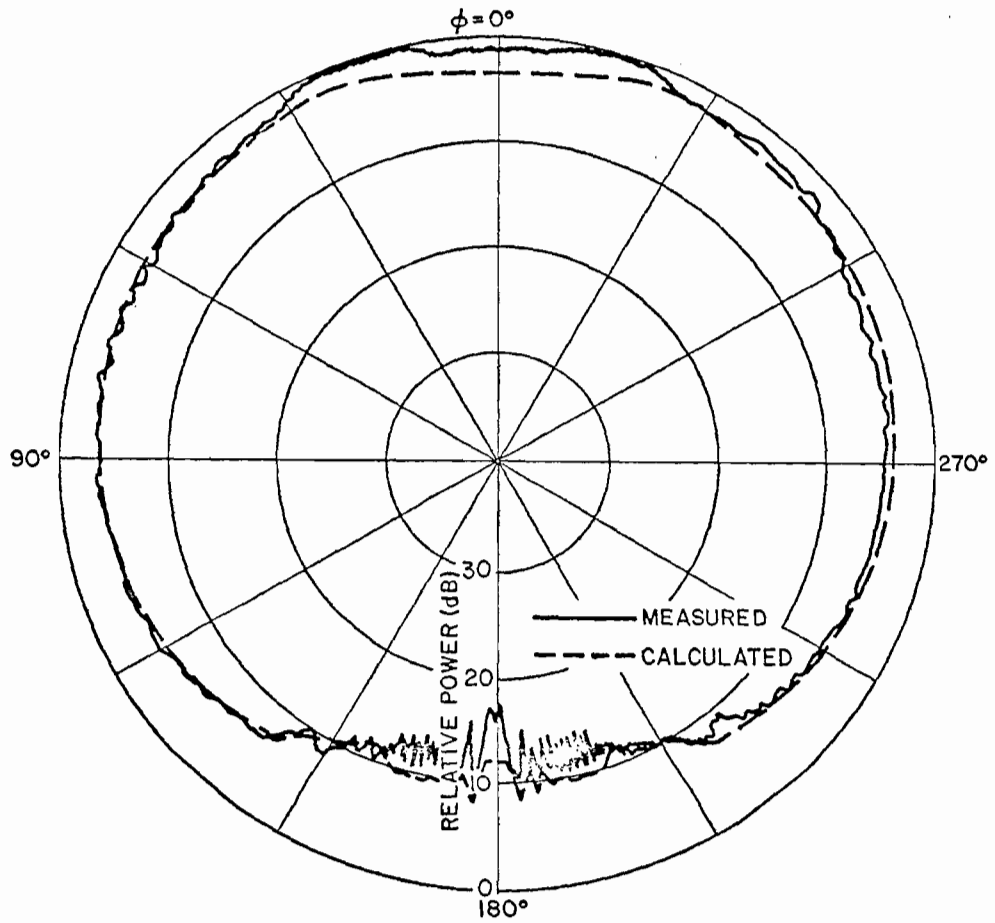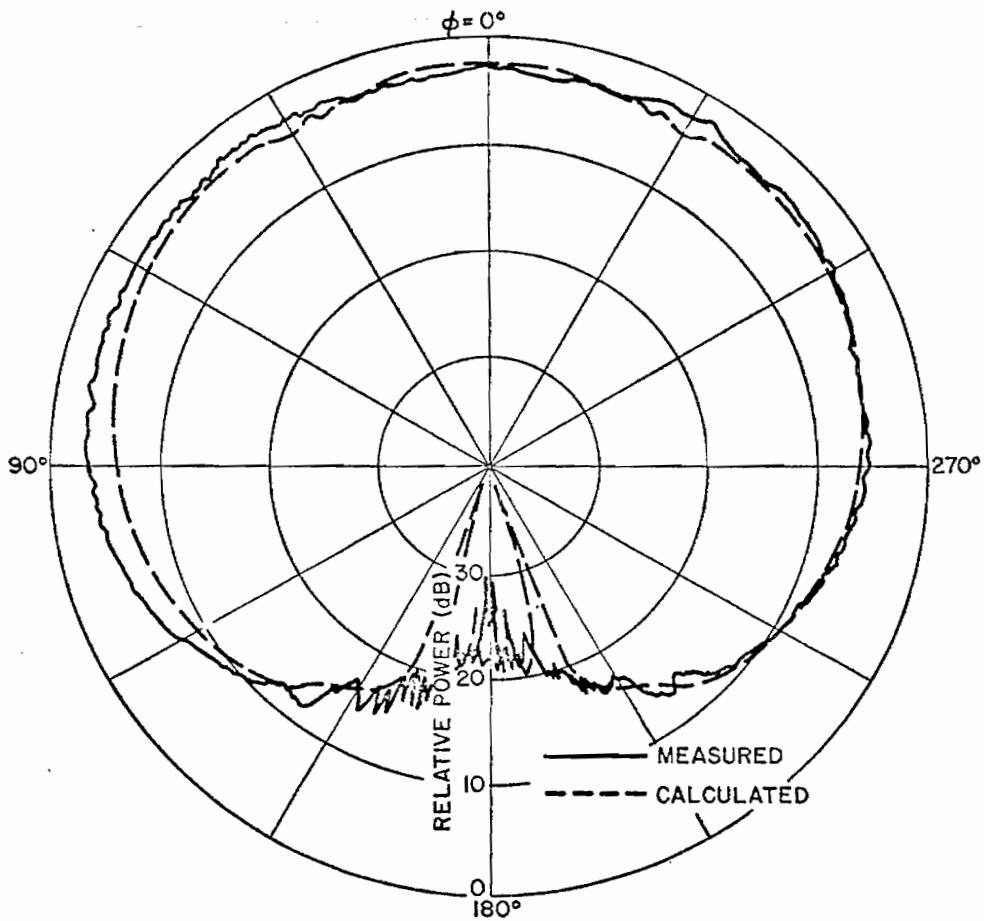Figure 53. Azimuth plane pattern of a λ/4 monopole mounted at station 220 on top of a Boeing 737 aircraft. (θ = 50°)
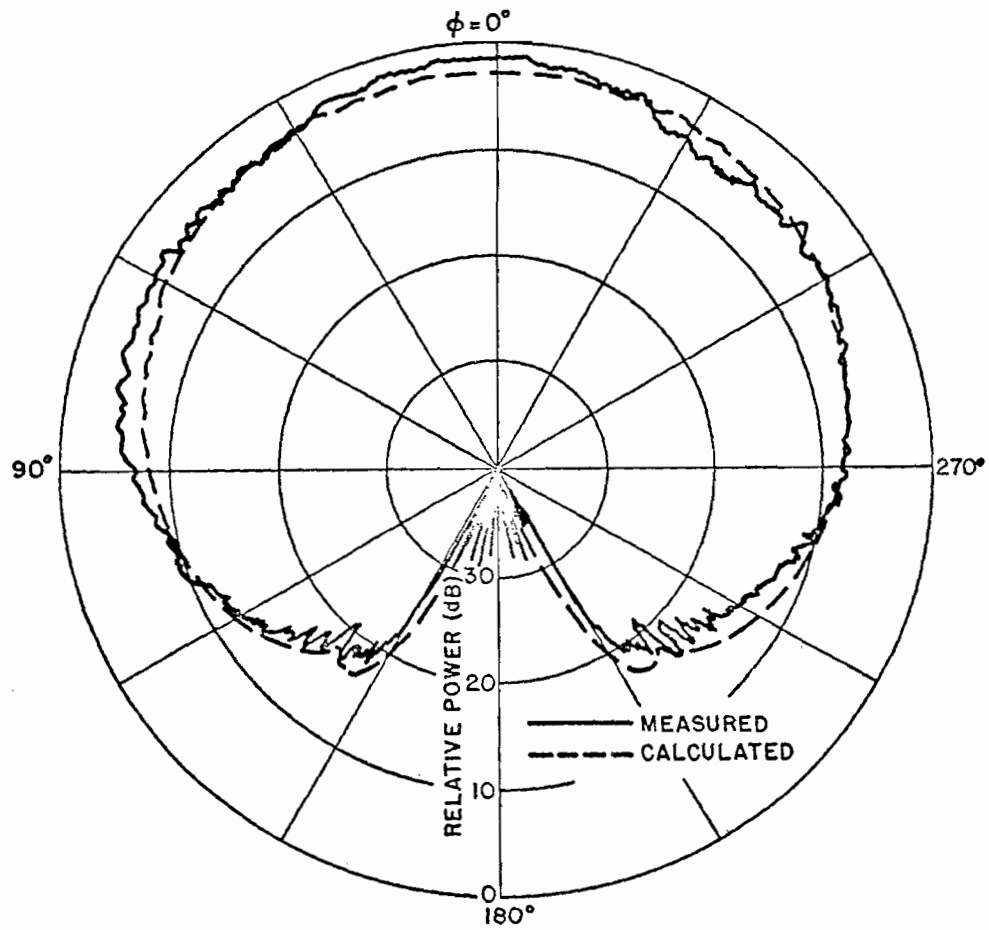
Figure 54. Azimuth plane pattern of a $\lambda/4$ monopole mounted
at station 220 on top of a Boeing 737 aircraft.
($\theta = 60°$)

Figure 55. Azimuth plane pattern of a λ/4 monopole mounted
at station 220 on top of a Boeing 737 aircraft.
(θ = 70°)

Figure 56. Azimuth plane pattern of a λ/4 monopole mounted
at station 220 on top of a Boeing 737 aircraft.
(θ = 80°)

Figure 57. Azimuth plane pattern of a λ/4 monopole mounted
at station 220 on top of a Boeing 737 aircraft.
(θ = 90°)

Figure 58. Azimuth plane pattern of a λ/4 monopole mounted at station 220 on top of a Boeing 737 aircraft. (θ = 100°)
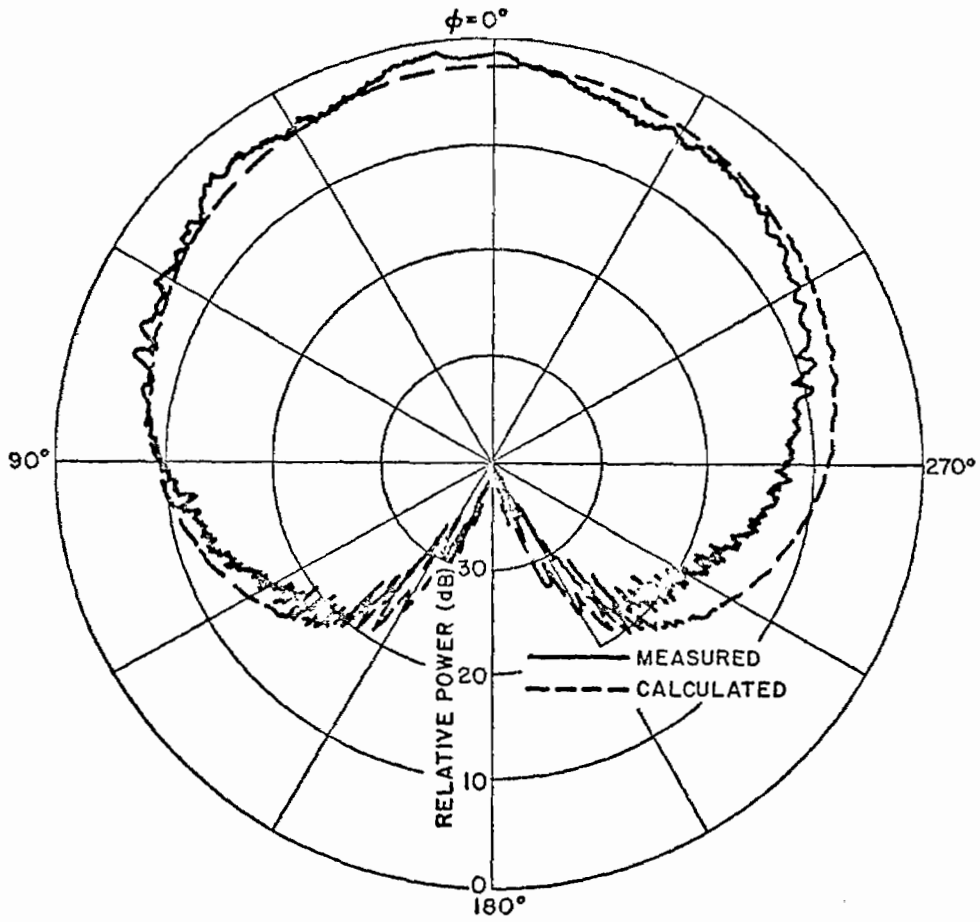
Figure 59. Azimuth plane pattern of a λ/4 monopole mounted
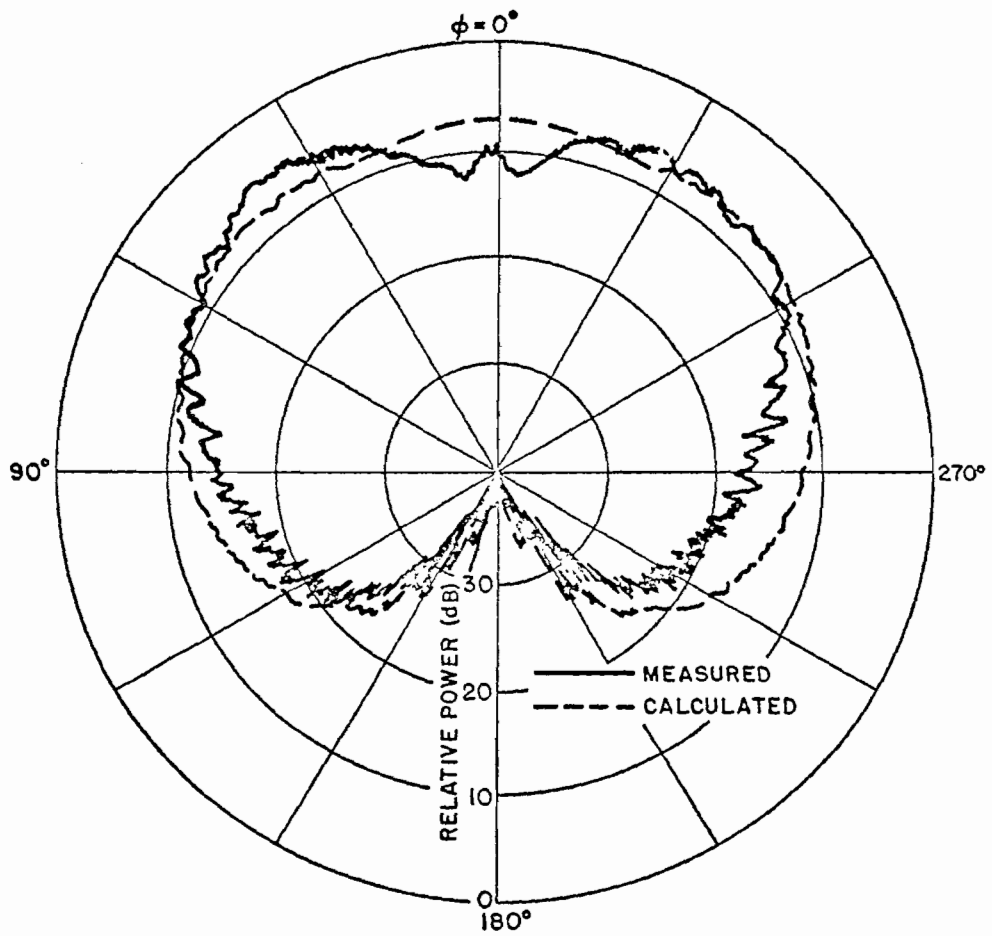at station 220 on top of a Boeing 737 aircraft.
(θ = 110°)

Figure 60. Azimuth plane pattern of a λ/4 monopole mounted at station 220 on top of a Boeing 737 aircraft. (θ = 120°)

SECTION V

SURFACE CURRENT AND CHARGE DENSITY INDUCED ON AIRCRAFT MODELS

Based on the GTD analyses for the airborne antenna problems, this chapter is devoted to calculate the surface current and charge density induced on various aircraft models using the reciprocity theorem. Recall that in Chapter I the relation between the antenna radiation patterns and the induced surface current and charge density has been discussed. For convenience, these relations are rewritten as follows:

$$|\rho_S^{\theta^i}| = 2\ \epsilon_0 |E_m^{\theta}|$$

$$|\rho_S^{\phi^i}| = 2\ \epsilon_0 |E_m^{\phi}|$$

$$|J_\phi^{\theta^i}| = \frac{2}{\eta}\ |E_a^{\theta}|$$

$$|J_\phi^{\phi^i}| = \frac{2}{\eta}\ |E_a^{\phi}|$$

$$|J_z^{\theta^i}| = \frac{2}{\eta}\ |E_c^{\theta}|$$

$$|J_z^{\phi^i}| = \frac{2}{\eta}\ |E_c^{\phi}|$$

(74)

Using Eq. (74) and the GTD analyses, numerical results of induced surface current and charge density are presented for various aircraft models.

Consider a Boeing 747 illuminated by a plane wave with broadside incidence. The geometry of the aircraft and its computer model are shown in Fig. 61 with observation point located on the top of the fuselage denoted by letter P in the figure. Note that the fuselage axis is assumed to be the z-axis. The magnitude and phase of induced current and charge densities for two different polarizations are presented in Figs. 62-65. The THETA MODE and PHI MODE appearing in these figures indicate that the electric field intensities associated with the incident plane wave are θ-polarized and φ-polarized, respectively.

The computed model of a KC-135 is shown in Fig. 66. A plane wave is incident at θ=45° and φ=45°. The surface current and charge densities induced on a KC-135 aircraft are shown in Figs. 67-70.

120

Finally, a Boeing 737 aircraft is investigated. The geometry and its computer model are shown in Fig. 71. The observation point is located at station 220 on top of the fuselage. The coordinate system used for the calculation is illustrated in Fig. 72. The complete volumetric pattern for the charge density induced at station 220 on top of a Boeing 737 is shown in Fig. 73.
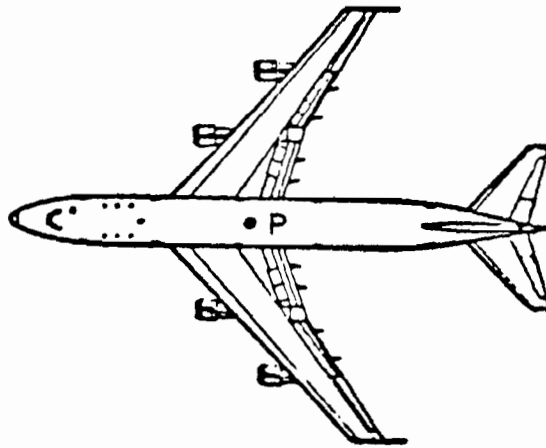

Figure 61a. Boeing 747 heavy transport aircraft.

Figure 61b. Computer model of a 747 aircraft.

Figure 62. The surface current and charge densities
induced on a 747 aircraft.

PLANE WAVE INCIDENT AT PHI= 0.00   DEGREES
                       THI= 90.00 DEGREES

MAGNITUDE

PHI MODE

Figure 63. The surface current and charge densities
induced on a 747 aircraft.

124

PHASE

THETA MODE

Figure 64. The surface current and charge densities
            induced on a 747 aircraft.

PLANE WAVE INCIDENT AT PHI= 0.00 DEGREES
                       THI= 90.00 DEGREES

PHASE

PHI MODE
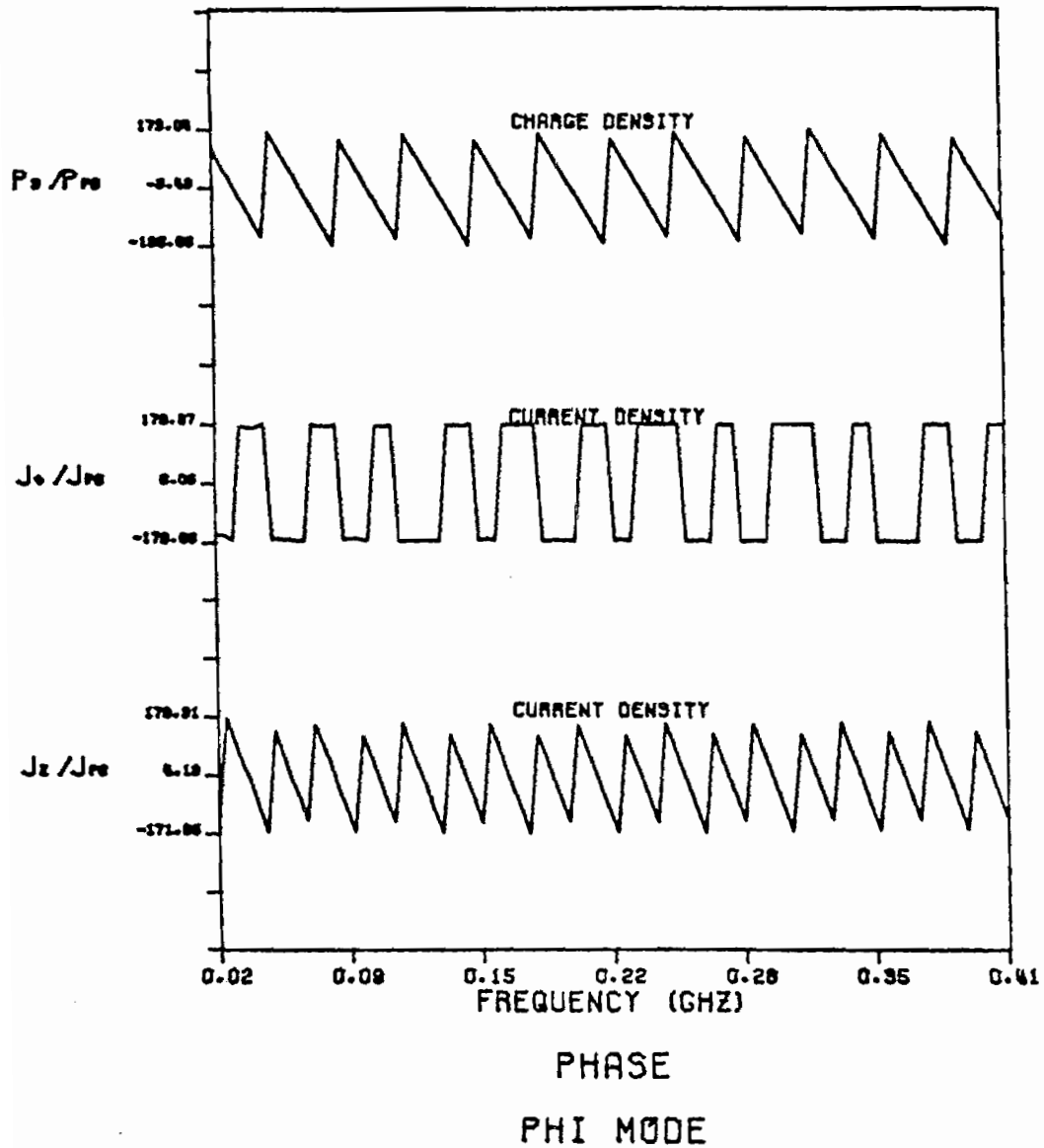
Figure 65. The surface current and charge densities
induced on a 747 aircraft.

126
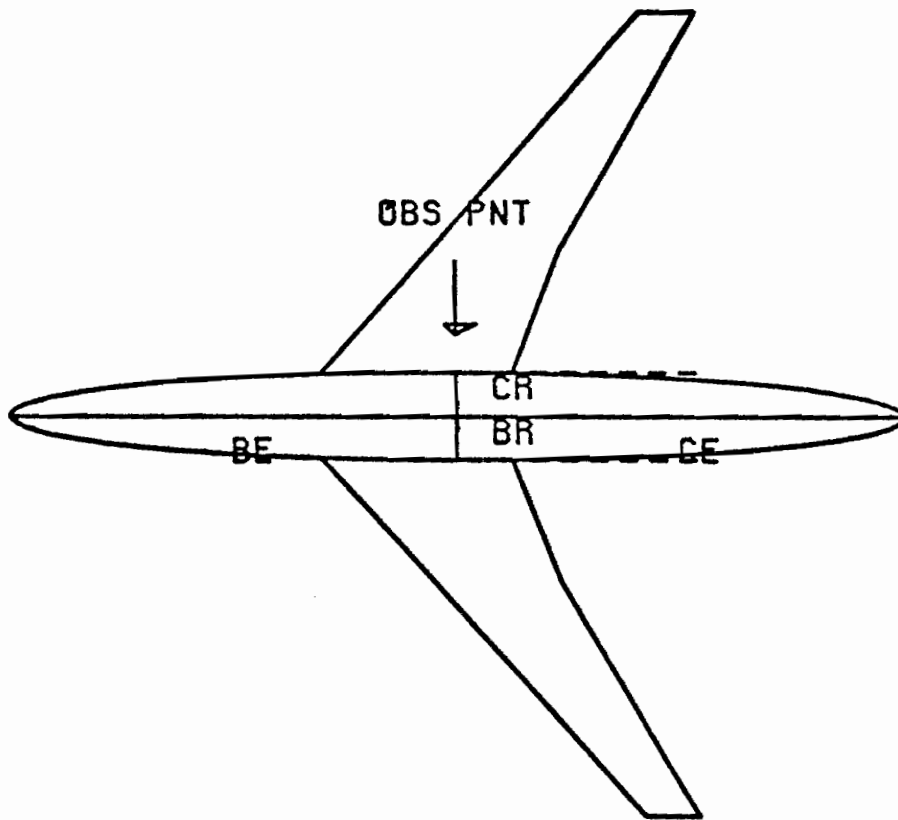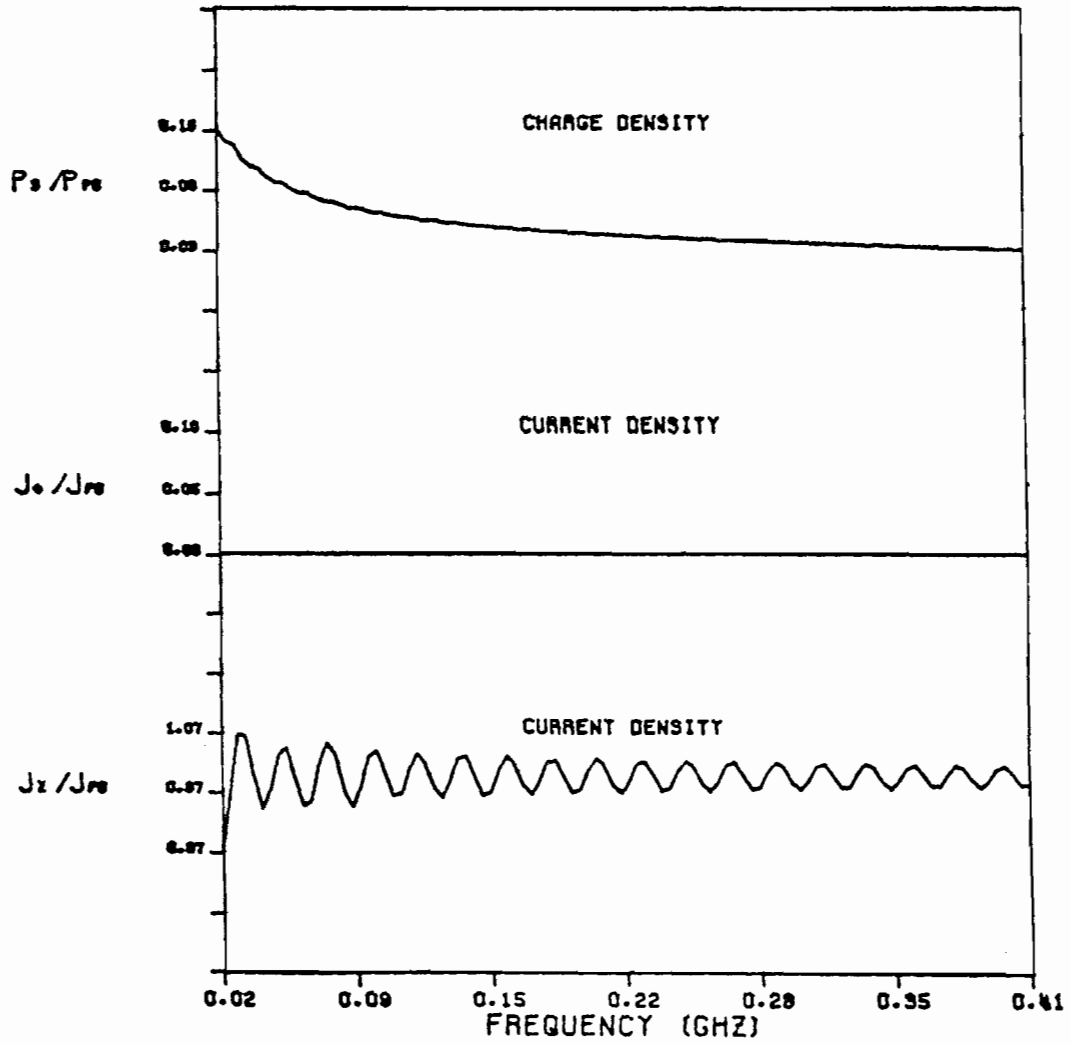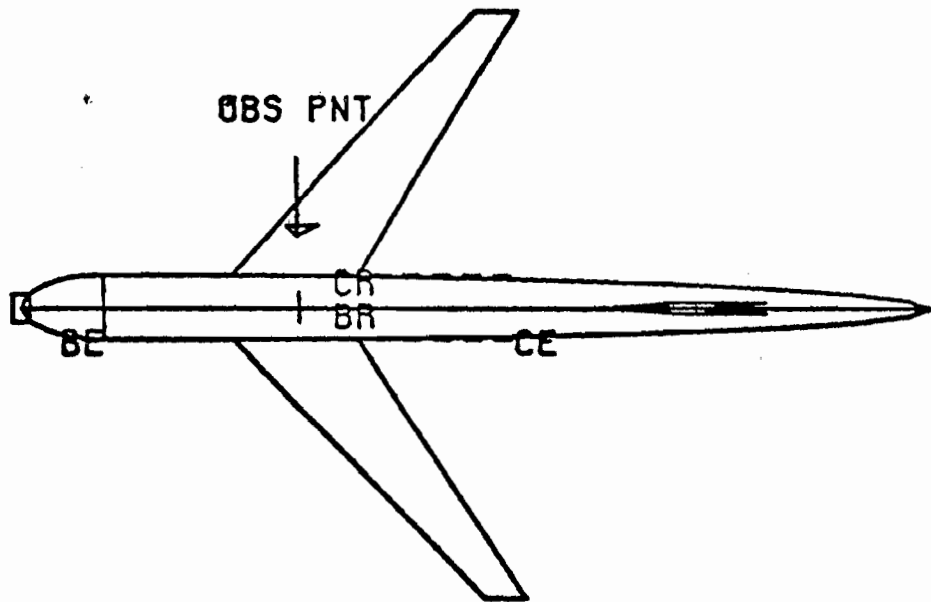
Figure 66. Computer model of a KC-135 aircraft.

OBSERVATION POINT PHS= 0.00   DEGREES
                ZS= 18.81   INCHES

PLANE WAVE INCIDENT AT PHI= 45.00 DEGREES
                     THI= 45.00 DEGREES
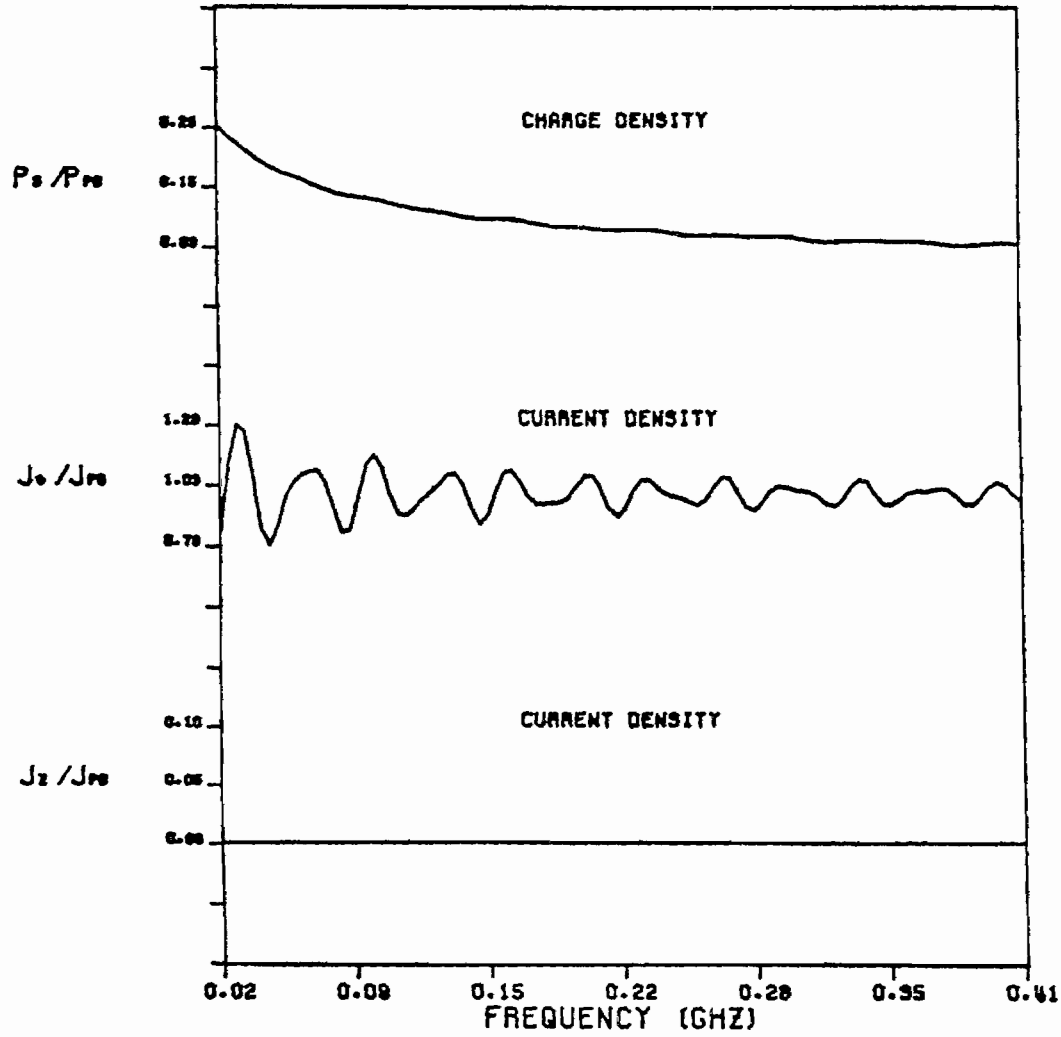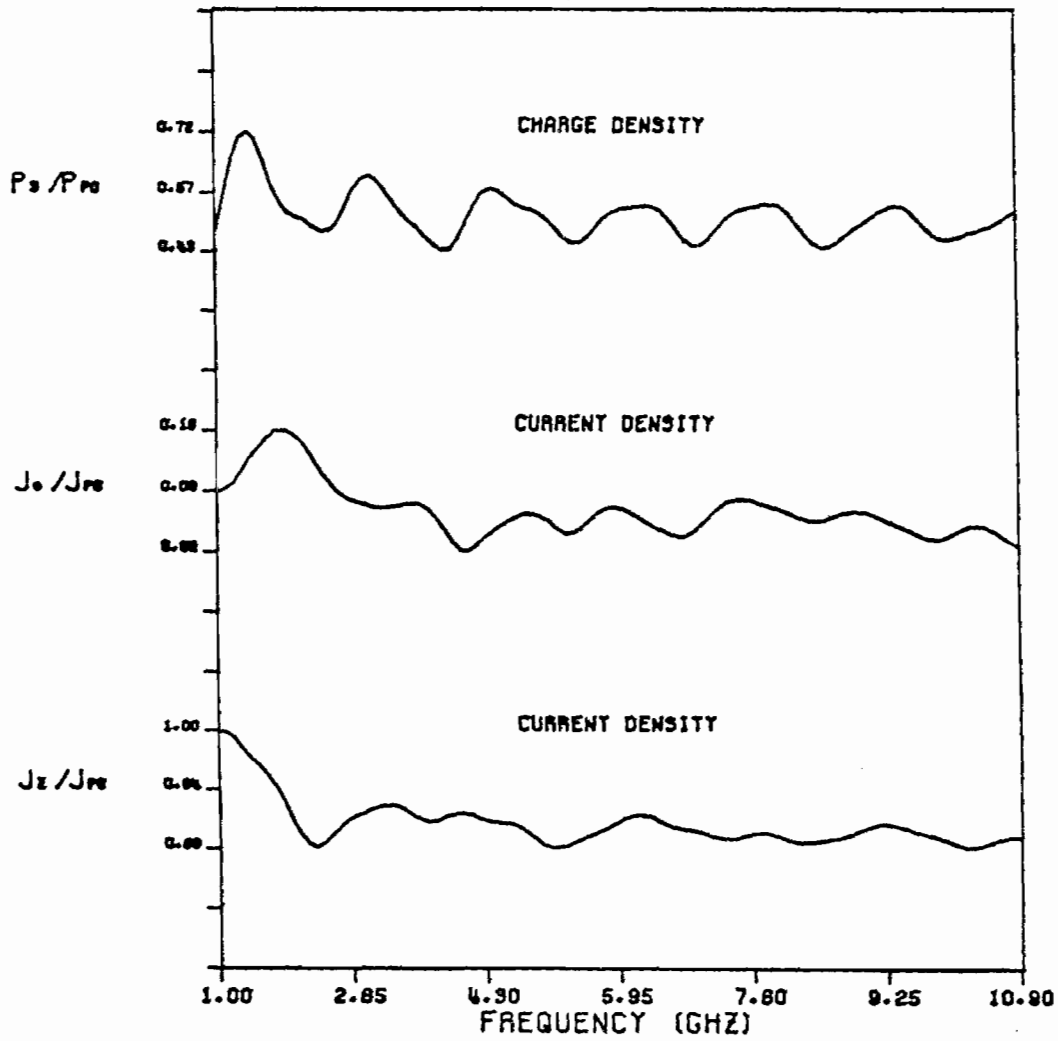
MAGNITUDE

THETA MODE

Figure 67.   The surface current and charge densities
             induced on a KC-135 aircraft.

OBSERVATION POINT PHS= 0.00   DEGREES
                        ZS= 18.81   INCHES

PLANE WAVE INCIDENT AT PHI= 45.00 DEGREES
                        THI= 45.00 DEGREES

CHARGE DENSITY

P_s / P_{rs}

CURRENT DENSITY

J_ϕ / J_{rs}

CURRENT DENSITY

J_z / J_{rs}

FREQUENCY (GHZ)

MAGNITUDE

PHI MODE
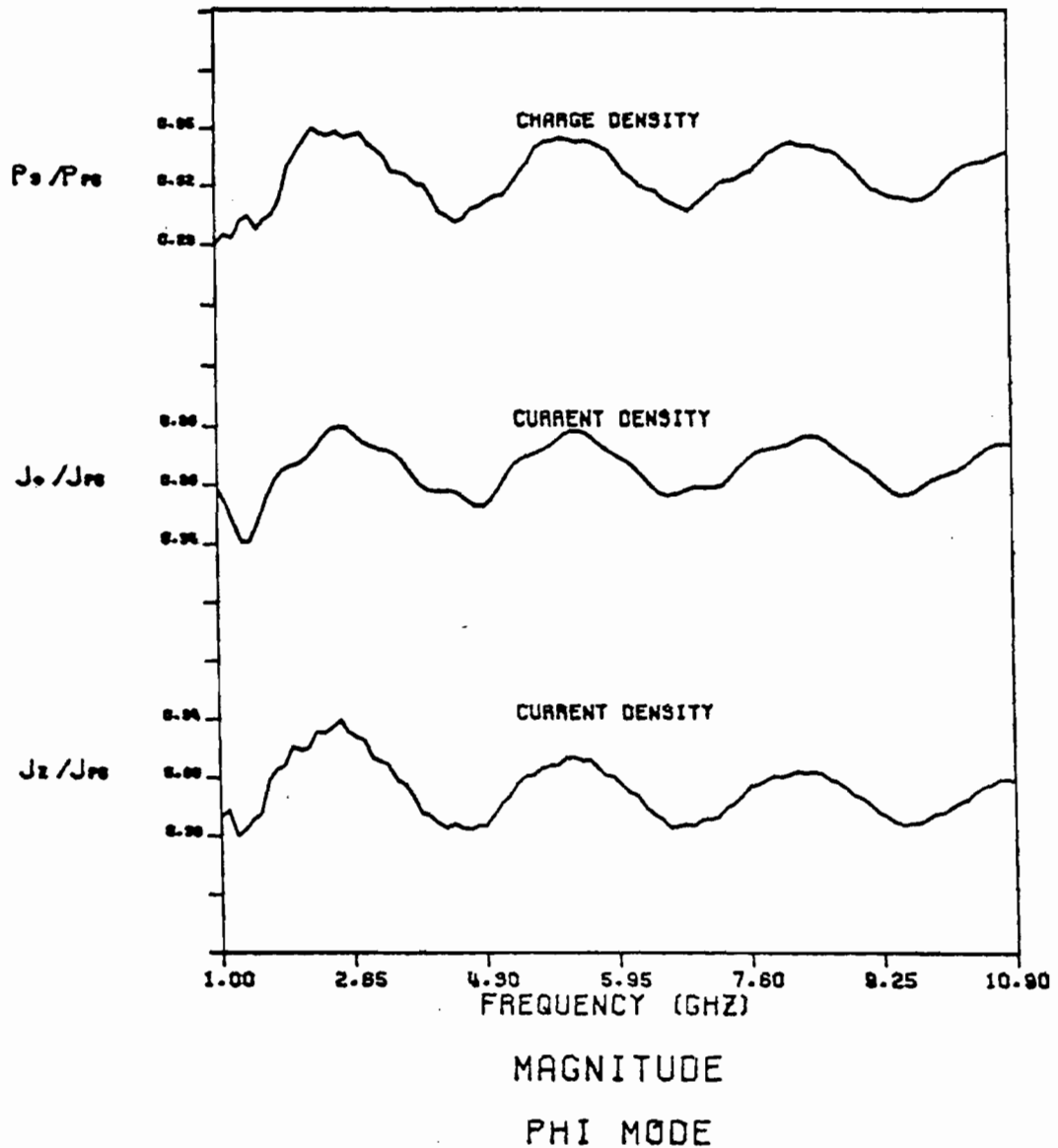
Figure 68. The surface current and charge densities
            induced on a KC-135 aircraft.

PLANE WAVE INCIDENT AT PHI= 45.00 DEGREES
                        THI= 45.00 DEGREES
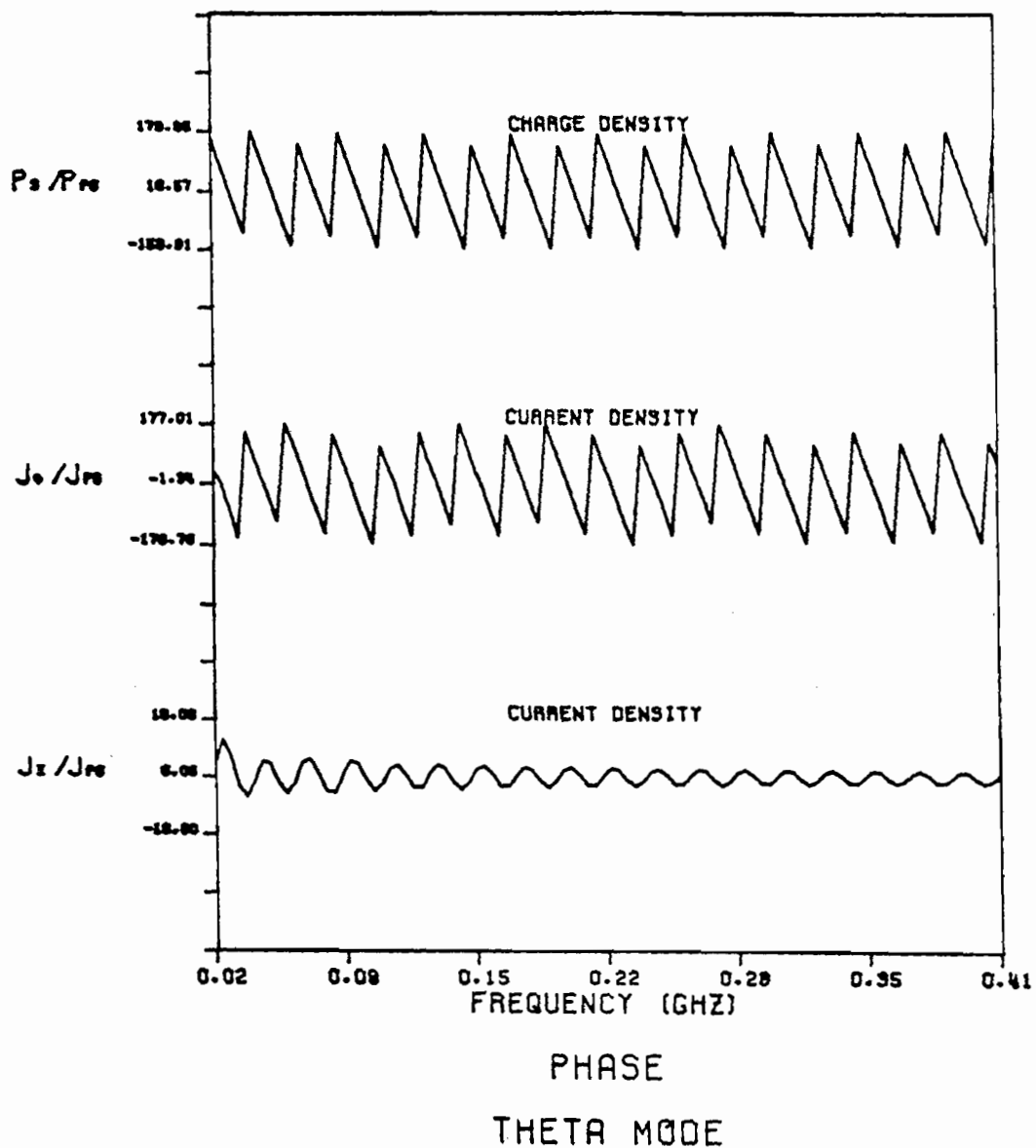

PHASE

THETA MODE
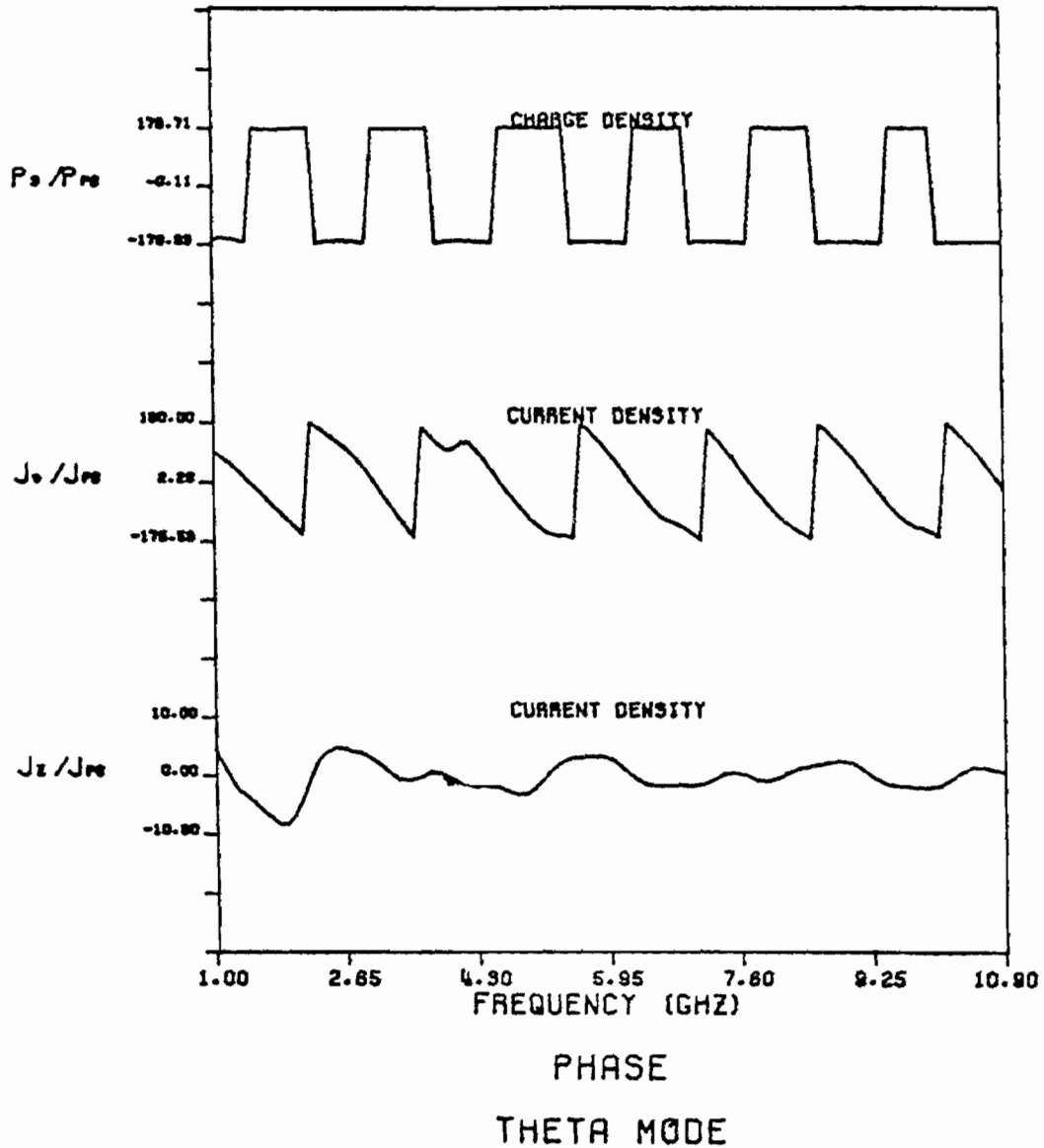
Figure 69. The surface current and charge densities
            induced on a KC-135 aircraft.

OBSERVATION POINT PHS= 0.00   DEGREES
                  ZS= 18.81   INCHES

PLANE WAVE INCIDENT AT PHI= 45.00 DEGREES
                  THI= 45.00 DEGREES
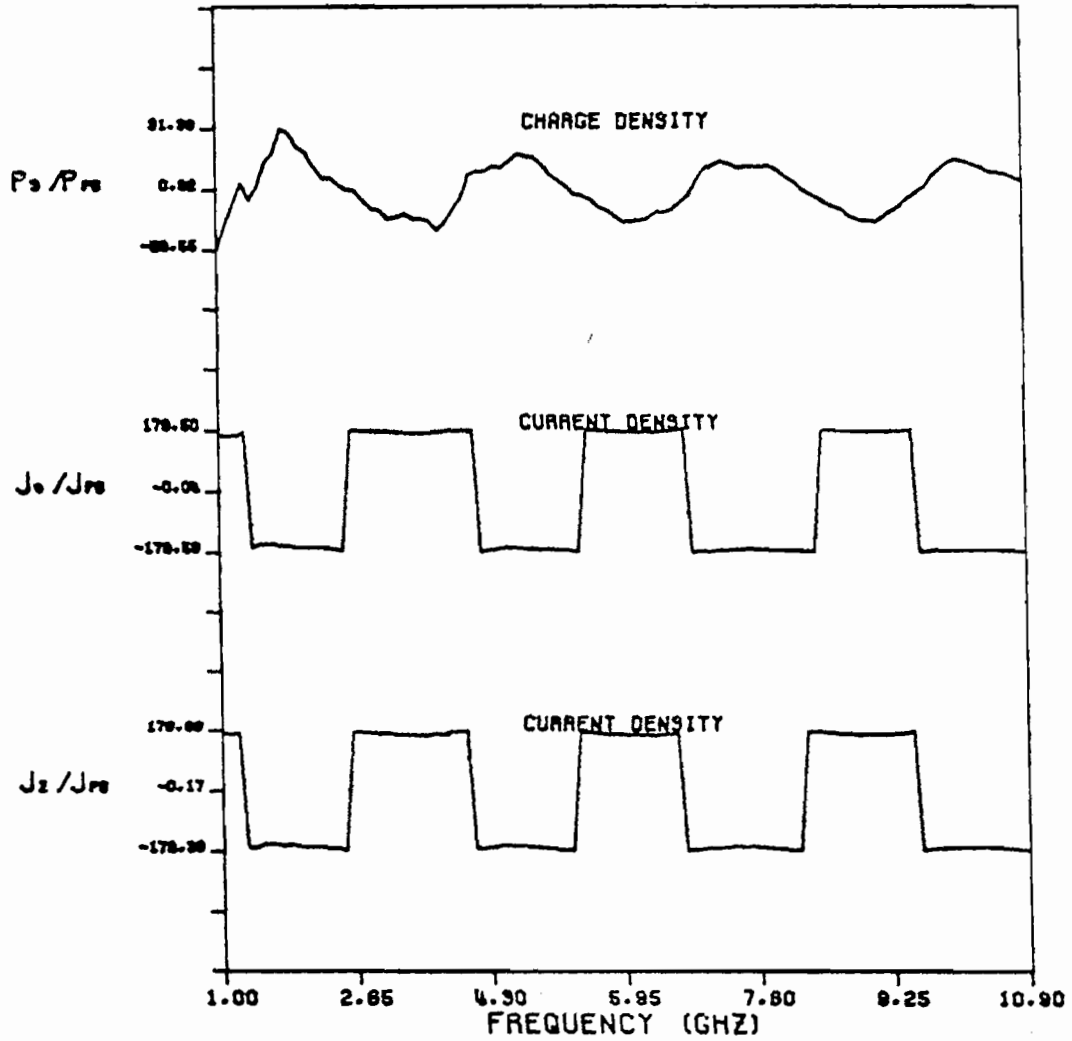

PHASE

PHI MODE

Figure 70.   The surface current and charge densities
             induced on a KC-135 aircraft.

131
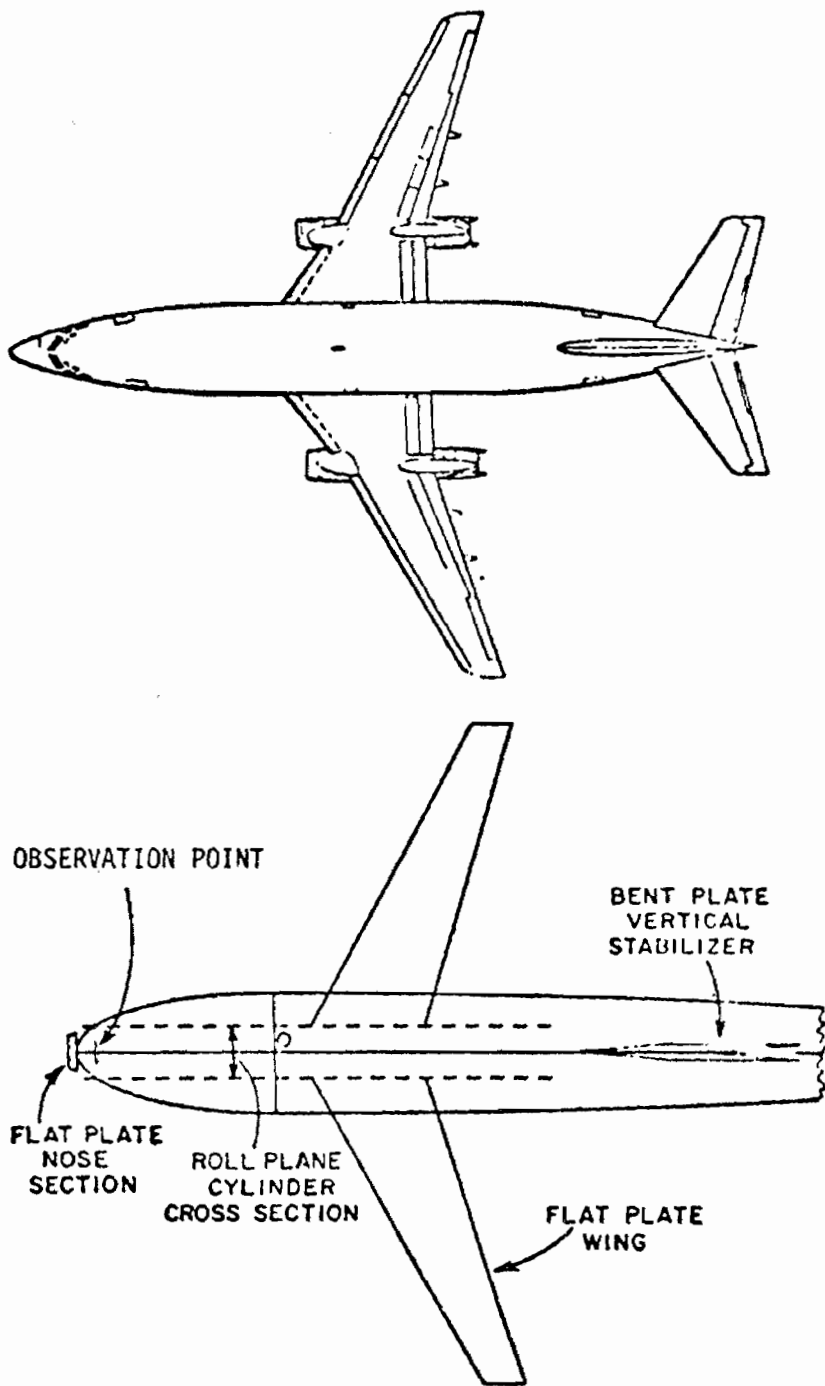
Figure 71.   Computer simulated model for a Boeing 737 aircraft
             (top view). The observation point is located at
             station 220 on the top of the fuselage.
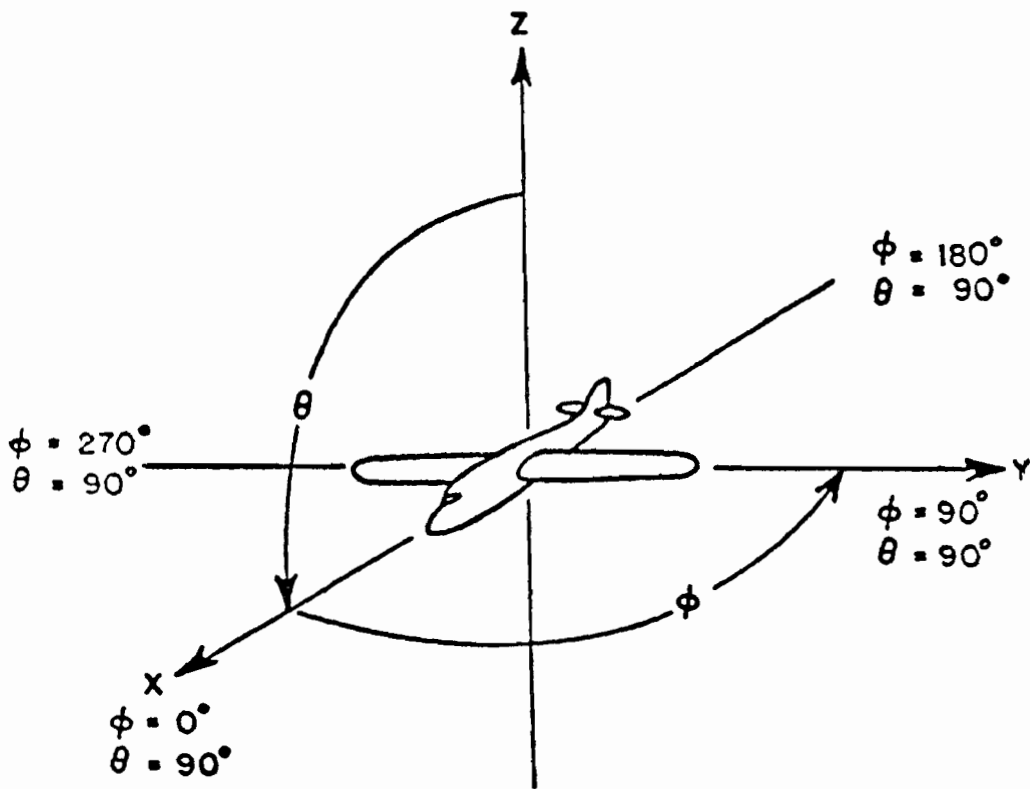
Figure 72. Illustration of the coordinate system
used for calculations.
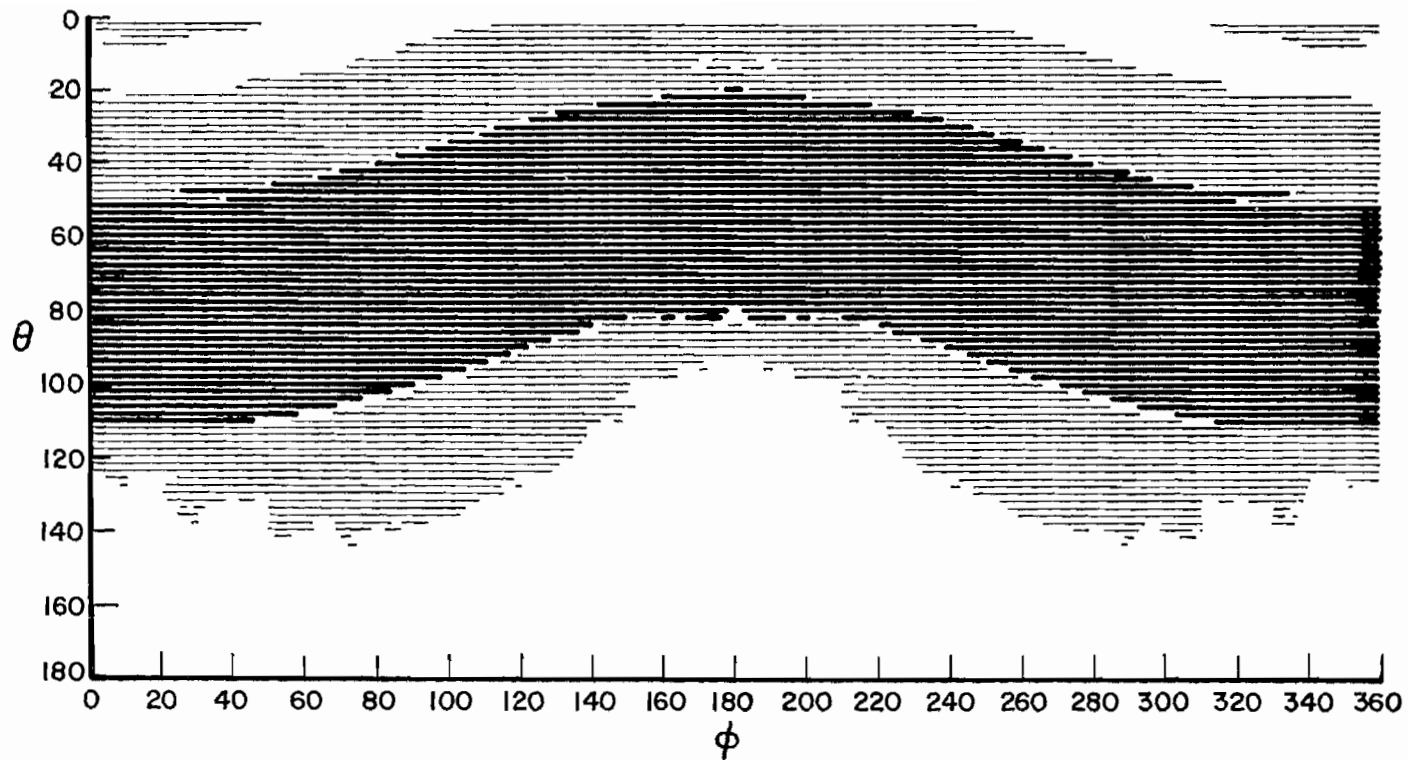
Figure 73. Induced charge density for any arbitrarily incident E_θ plane wave on a 737 aircraft.

Black: $\frac{\rho}{2\varepsilon_0 E_0} \geq 1/2$

Gray: $1/10 < \frac{\rho}{2\varepsilon_0 E} < 1/2$

White: $\frac{\rho}{2\varepsilon_0 E_0} \leq 1/10$

SECTION VI

SUMMARY AND CONCLUSIONS

High frequency solutions for the three-dimensional surface current and charge density induced on the aircraft fuselage for arbitrarily-incident plane wave has been the object of this research. It is well known that the induced surface current and charge density due to plane wave incidence are related to the radiation pattern due to infinitesmal monopole and slot antennas. Since extensive experimental scale-model measurements for flush-mounted antennas on aircraft are available for comparison, the analyses for the induced surface current and charge density is carried out in terms of antenna problems. This report presents an accurate and efficient solution for the problem using the geometrical theory of diffraction (GTD).

The basic approach applied here is to break up the aircraft into its simplest structural forms. Due to the high frequency requirements of airborne antennas, these structures may be analyzed using ray optics techniques with numerical values obtained using GTD. Once the scattering from these various structures is found, it is then adapted to the aircraft model simply by adjusting the field incident on the structural scatterer. The only limitation of the GTD solution is that the source and various scattering centers be separated by at least a wavelength. In some cases, even this requirement can be relaxed.

A theoretical solution was developed in Chapter IV to analyze complicated three-dimensional volumetric radiation patterns for fuselage mounted airborne antennas. This solution utilizes roll and elevation plane model analyses developed earlier. The procedure to combine these two solutions into a complete solution that can handle the volumetric pattern is based on a previous study of antennas mounted on prolate spheriods. The belt concept of blending these two solutions together is the key to the success of the complete solution. The use of flat or bent plates to approximate an aircraft cockpit nose section and vertical stabilizer is also new and quite useful, not only because of its simplicity in analysis but also due to its practicality in computation.

A numerical procedure that can be used to model a practical aircraft fuselage has also been presented. The three-dimensional fuselage in the numerical model is simulated by two composite elliptic cylinders; one approximates the aircraft profile and the other its cross-section. These ellipses are numerically obtained through a best-fit ellipse routine. The description of the wings, cockpit, and stabilizers are measured directly from the three principal views of the aircraft.

To demonstrate the validity and applicability of the theoretical solutions, the radiation patterns in the principal planes for antennas mounted on various locations on a KC-135 aircraft and a Boeing 737 aircraft have been calculated and compared with measurements taken at NASA (Hampton, Va.). The results show good agreement between the analytical and experimental work and obvious improvement over previous analses. To illustrate the versatility of the new solution, the radiation patterns for antennas mounted on a space shuttle with the radome taken into account have been calculated. Again, the result is very encouraging. The off-principal plane radiation patterns of a λ/4 monopole mounted above the cockpit of a Boeing 737 aircraft have been calculated. The patterns obtained were shown to compare well with measurements taken at NASA (Hampton, Va.), which verify the assumptions made in the theoretical solutions.

Finally, some numerical results for the surface current and charge density induced on various aircraft models are calculated and presented in Section V. The solutions developed in this research provide a useful, accurate, economical, and efficient means for determining the surface current and charge density induced on aircraft fuselage due to arbitrary plane wave incidence. For example, the program developed in this study has now been delivered to NASA (Hampton, Va.), and it typically runs a pattern in 30 seconds or less on a CDC 6600 digital computer.

It should be noted that in the present study, the effect of the engines is negligible and they have been ignored in the model. However, the engines appear to have some effect on the radiation patterns when an antenna is mounted on the bottom of the fuselage. When necessary, the engine effect can be included in the solution by using a finite elliptic cylinder as presented in Reference [55].

APPENDIX A

COORDINATE SYSTEMS TRANSFORMATION

Consider that a vector R (x, y, z) in an xyz coordinate system as shown in Fig. A-la. A second coordinate system, (x'y'z') is also depicted, which is formed by first rotating the x-axis of the original coordinate system through an angle of ϕ_0 about z-axis and then, the z-axis through an angle of θ_0 about the rotated x'-axis. Recall that in a vector space, the coordinates x_i of a vector $\overline{X}$ representing a point in n-dimensional space can also be regarded as the coefficients of the unit vectors $\overline{e}_i$ if $\overline{X}$ is represented as a sum of multiples of the unit vectors

$$X = \begin{bmatrix} x_i \\ \cdot \\ \cdot \\ \cdot \\ x_n \end{bmatrix} = x_1 \overline{e}_1 + \cdots + x_n \overline{e}_n \qquad (A-1)$$

These unit vectors form a vector basis which span the n-dimensional vector space. In the three-dimensional geometry, where n = 3, let $\{\hat{x}, \hat{y}, \hat{z}\}$ be a basis of the vector space under consideration. Thus, the vector $\overline{R}$ can be written in terms of these unit vectors as

$$\overline{R} = x \hat{x} + y \hat{y} + z \hat{z} \qquad (A-2)$$

Let $\{\hat{x}', \hat{y}', \hat{z}'\}$ be another basis of the same space such that the vector $\overline{R}$ is expressed as

$$\overline{R} = x'\hat{x}' + y'\hat{y}' + z'\hat{z}' \qquad (A-3)$$

Then, by a linear transformation, the coordinates of the vector $\overline{R}$ relative to the $\{\hat{x}, \hat{y}, \hat{z}\}$ basis can be determined from the coordinates relative to the $\{\hat{x}', \hat{y}', \hat{z}'\}$ basis through a matrix relation as
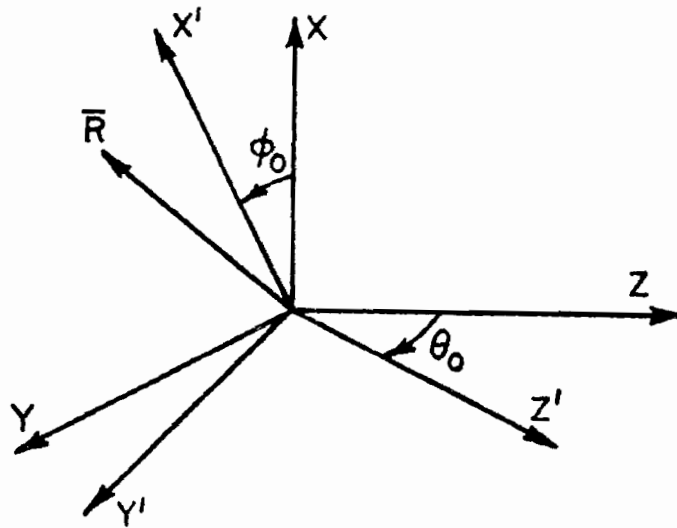
$$X = PX' \qquad (A-4)$$

137

Figure A-1a. Illustration of coordinate system rotation.
(Rotate ϕ_0 angle about z axis and then rotate
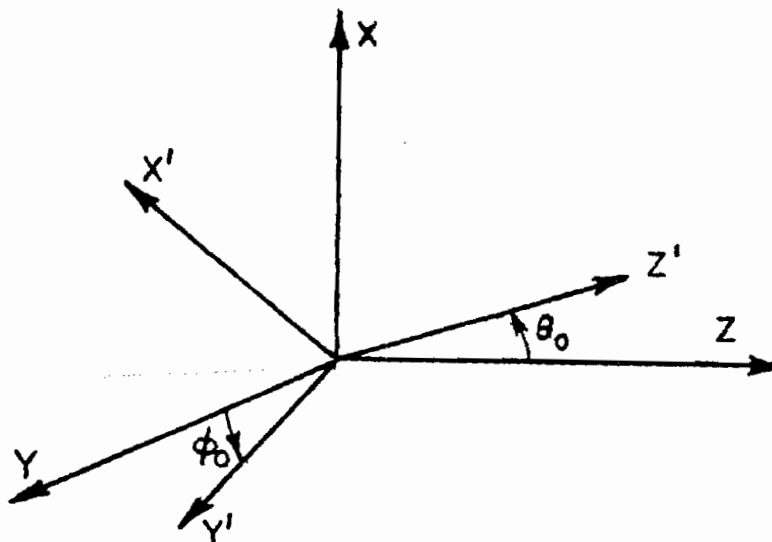θ_0 angle about x' axis).

Figure A-1b. Illustration of coordinate system rotation.
(Rotate ϕ_0 angle about z axis and then rotate
θ_0 angle about y' axis).

Where X and X' are column vectors given by

$$X = \begin{bmatrix} x \\ y \\ z \end{bmatrix} \quad \text{and} \quad X' = \begin{bmatrix} x' \\ y' \\ z' \end{bmatrix} \tag{A-5}$$

and P is a 3x3 transformation matrix from the $\{\hat{x}, \hat{y}, \hat{z}\}$ basis to $\{\hat{x}', \hat{y}', \hat{z}'\}$ basis. By multiplying Eq. (A-6) by P^{-1}, the inverse of P, the coordinates of $\bar{R}$ in $\{\hat{x}', \hat{y}', \hat{z}'\}$ basis can be found in terms of the coordinates in $\{\hat{x}, \hat{y}, \hat{z}\}$ basis, i.e.,

$$X' = P^{-1}X \tag{A-6}$$

Eqs. (A-4) and (A-6) describe the relation on which the coordinates of a vector in one coordinate system can be determined from its coordinates relative to another coordinate system.

Since the unit vectors $\hat{x}'$, $\hat{y}'$, and $\hat{z}'$ are related to the unit vectors, $\hat{x}$, $\hat{y}$, and $\hat{z}$ in the following manner, i.e.,

$$\hat{x}' = \cos \phi_0 \, \hat{x} + \sin \phi_0 \, \hat{y}$$

$$\hat{y}' = -\cos \theta_0 \sin \phi_0 \hat{x} + \cos \theta_0 \cos \phi_0 \hat{y} + \sin \theta_0 \hat{z} \tag{A-7}$$

$$\hat{z}' = \sin \theta_0 \sin \phi_0 \, \hat{x} - \sin \theta_0 \cos \phi_0 \, \hat{y} + \cos \theta_0 \, \hat{z}$$

the transition matrix P_x, which is defined as the transpose of the above matrix of coefficients, can be obtained as

$$P_x = \begin{bmatrix} \cos \phi_0 & -\cos \theta_0 \sin \phi_0 & \sin \theta_0 \sin \phi_0 \\ \sin \phi_0 & \cos \theta_0 \cos \phi_0 & -\sin \theta_0 \cos \phi_0 \\ 0 & \sin \theta_0 & \cos \theta_0 \end{bmatrix} \tag{A-8}$$

where subscript x indicates the θ angle rotation is about the rotated x'-axis. By inverting the matrix P_x, the inverse matrix P_x^{-1} of P_x can be easily determined and is given by

$$P_x^{-1} = \begin{bmatrix} \cos \phi_0 & \sin \phi_0 & 0 \\ -\cos \theta_0 \sin \phi_0 & \cos \theta_0 \cos \phi_0 & \sin \theta_0 \\ \sin \theta_0 \sin \phi_0 & -\sin \theta_0 \cos \phi_0 & \cos \theta_0 \end{bmatrix} \qquad (A-9)$$

Similarly, if a new coordinate system, x'y'z' system, is set up by first rotating the x-axis of an angle of ϕ_0 about z-axis and then the z-axis an angle of θ_0 about the y'-axis in a counter-clockwise sense as seen in Fig. A-1b, the transformation matrices P_y and P_y^{-1} can be determined as

$$P_y = \begin{bmatrix} \cos \theta_0 \cos \phi_0 & -\sin \phi_0 & \sin \theta_0 \cos \phi_0 \\ \cos \theta_0 \sin \phi_0 & \cos \phi_0 & \sin \theta_0 \sin \phi_0 \\ -\sin \theta_0 & 0 & \cos \theta_0 \end{bmatrix} \qquad (A-10)$$

and

$$P_y^{-1} = \begin{bmatrix} \cos \theta_0 \cos \phi_0 & \cos \theta_0 \sin \phi_0 & -\sin \theta_0 \\ -\sin \phi_0 & \cos \phi_0 & 0 \\ \sin \theta_0 \cos \phi_0 & \sin \theta_0 \sin \phi_0 & \cos \theta_0 \end{bmatrix} \qquad (A-11)$$

where the subscript y indicates the rotation of θ_0 angle is about the rotated y'-axis in distinction with that of the x'-axis in Fig. A-1a.

APPENDIX B

GEOMETRICAL CONFIGURATION FOR OFF-CENTER LINE
MOUNTED ANTENNAS

Consider a source which is located at some angle off the center
line of an aircraft fuselage as shown in Fig. B-1. This source can be
an infinitesimal monopole or arbitrarily oriented slot element. As
discussed in Section III, the surface geometry nearest to the antenna
has the most significant effect on the radiation patterns. For this
case, the longitudinal surface curvature in the plane which is parallel
to both the Z_{ref} axis and the surface normal at the source location,
and the transverse surface curvation in the other plane which is
orthogonal to the longitudinal plane, as shown in Fig. B-1, play a
dominant role in predicting the radiation patterns of airborne antennas.
However, the transverse surface profile which cuts obliquely across
the fuselage is not easily obtained from a scale model drawing of an
aircraft (usually, only the elevation profile and cross section are
given). Thus, to obtain the necessary elliptic cylinders for the
volumetric pattern analysis, the aircraft cross section which cuts
orthogonally through the source location is used to approximate the
required transverse surface profile cylinder. This approximation is
reasonable since the transverse surface profile of an actual aircraft
does not change drastically for a small angle deviation. For the other
elliptic cylinder which approximates the longitudinal surface profile
at the source location, the following approach can be employed.

First, let us approximate the elevation profile of the aircraft
of interest by a composite elliptic cylinder as done previously
in Section III. Its necessary parameters are given by a_0, semi-
major axis, b_0 and b_0', semi-minor axis for left and right half
elliptic cylinder respectively, as shown in Fig. B-2. Recall that
the source location in our volumetric analysis is defined by
(ϕ_s, z_s), as seen in Figs. B-2 and B-3, relative to the aircraft
fuselage cross section where the source is located. Since the
position of the source is given in terms of an elliptic cylinder
approximating the fuselage cross section at the source location,
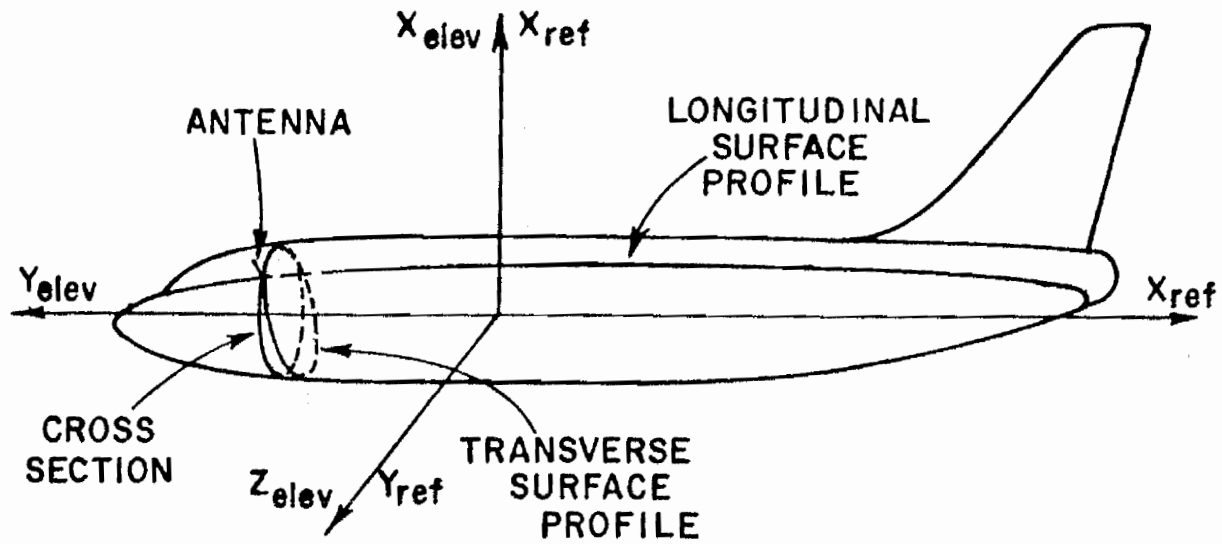its Cartesian coordinates can be easily determined as

Figure B-1. Geometrical configuration of the longitudinal and transverse surface profile at the antenna location.
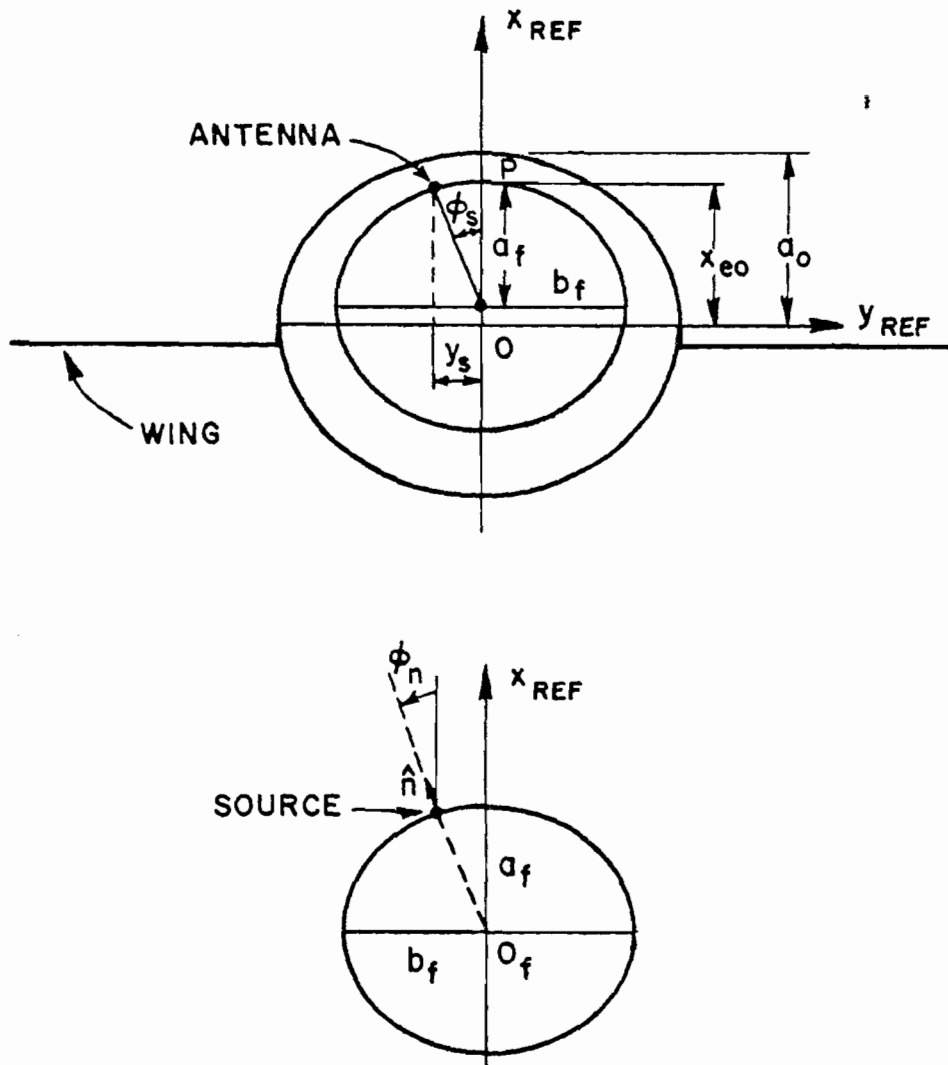
Figure B-2. Front view of the roll plane (transverse) cylinder
showing the antenna location and its surface normal.
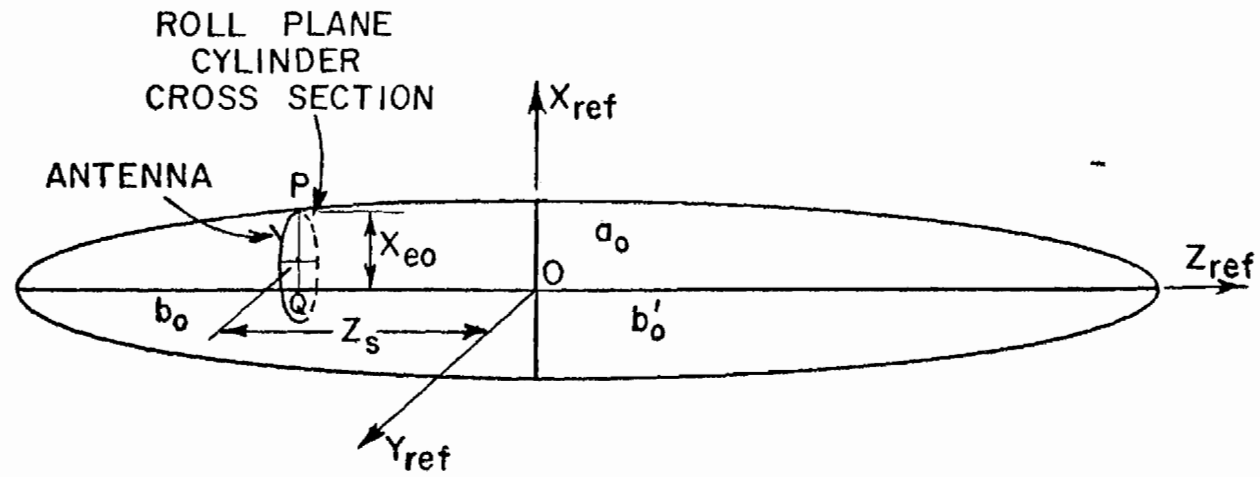
Figure B-3. Geometrical configuration of the antenna location.

$$x_s{}' = \rho_s \cos \phi_s$$

$$\text{(B-1)}$$

$$y_s{}' = \rho_s \sin \phi_s$$

where

$$\rho_s = \frac{a_f\, b_f}{\sqrt{b_f^2 \cos^2 \phi_s + a_f^2 \sin^2 \phi_s}}$$

The quantities a_r and b_r are the semimajor and semiminor axes of the cross sectional elliptic cylinder. In terms of the elliptic cylinder coordinate system as discussed in Chapter V, $x_s{}'$ and $y_s{}'$ are given by

$$x_s{}' = a_f \cos v_s$$

$$\text{(B-2)}$$

$$y_s{}' = b_f \sin v_s$$

where

$$v_s = \frac{a_f}{b_f} \tan \phi_s$$

From Fig. B-3, the distance x_{eo} between points P and Q is found via the ellipse equation as

$$x_{eo} = \begin{cases} \dfrac{a_0}{b_0} \sqrt{b_0^2 - z_s^2} & \text{if } z_s \text{ is negative} \\[2em] \dfrac{a_0}{b_0'} \sqrt{b_0'^2 - z_s^2} & \text{if } z_s \text{ is positive} \end{cases} \qquad \text{(B-3)}$$

where a_0, b_0, and b_0' have been defined earlier. Since the origin of the cross sectional cylinder is defined at a_f from point P along

145

line PQ, the source position in terms of the reference coordiante system can be easily determined from Figs.

$$x_s = (x_{eo} - a_f) + a_f \cos v_s$$

$$(B-4)$$

$$y_s = b_f \sin v_s$$

Once the source location is determined in the reference coordinate system, the actual composite elliptic cylinder to simulate the longitudinal surface profile at the antenna location is given as

$$a_e = \begin{cases} b_0 \sqrt{\dfrac{x_s^2 + y_s^2}{b_0^2 - z_s^2}} & \text{if } z_s \text{ is positive} \\ \\ b_0' \sqrt{\dfrac{x_s^2 + y_s^2}{b_0'^2 - z_s^2}} & \text{if } z_s \text{ is negative} \end{cases}$$

$$(B-5)$$

$$b_e = b_0$$
$$b_e' = b_0'$$

As described earlier, the elliptic cylinder which simulates the fuselage cross section at the source location is used to arroximate the transverse surface profile. Consequently, the necessary axes of the transverse elliptic cylinder are given by

$$a_r = a_f$$

$$(B-6)$$

$$b_r = b_f$$

Note that the transverse surface profile discussed previously lies in a plane which is parallel to the surface normal at the source location. Hence, the transverse or roll plane elliptic cylinder needs a tilt such that the cylinder surface normal aligns with the original surface normal as seen in Fig. B-4.
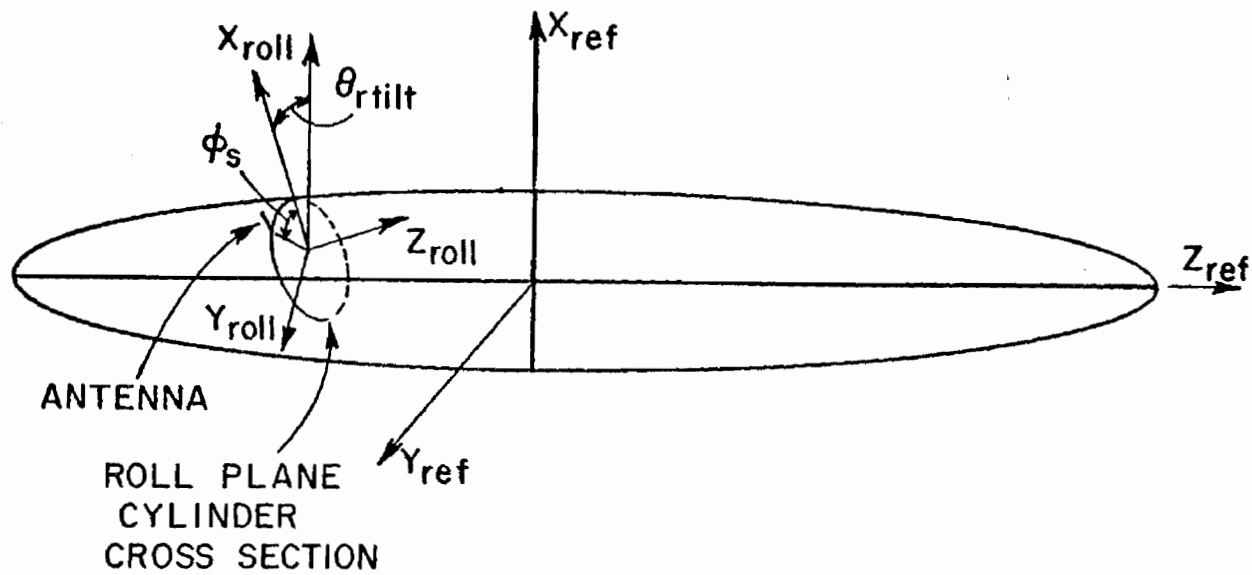
146

Figure B-4. Illustration of the coordinate systems used in the roll plane model relative to the reference coordinate system for off center line mounted antennas.

The required tilt or rotation $(\theta_{r\ tilt}, \phi_{r\ tilt})$ is given by

$$
\theta_{r\ tilt} = \begin{cases} \tan^{-1} \dfrac{a_e^2\, z_s}{b_e^2 \sqrt{x_s^2 + y_s^2}} & \text{if } z_s \text{ is positive} \\[2em] \tan^{-1} \dfrac{a_e^2\, z_s}{b_e'^2 \sqrt{x_s^2 + y_s^2}} & \text{if } z_s \text{ is negative} \end{cases}
$$

(B-7)

$$\phi_{r\ tilt} = 0$$

with respect to the reference coordinate system. It is noted that the rotation described here is about y_{ref} axis and not x_{ref} axis.

Notice also that the coordinate system of the elevation plane (longitudinal) model is rotated an angle (ϕ_n) which is the angle between the surface normal and x_{ref} axis as shown in Fig. B-2 relative to the reference coordinate system. In other words, the elevation model coordinate system shown in Fig. B-7 is obtained through a rotation $(\theta_{tilt}, \phi_{tilt})$ of the reference coordinate system as discussed in Appendix I. The rotation angles are given by

$$\theta_{e\ tilt} = 90°$$

(B-8)

$$\phi_{e\ tilt} = \phi_n$$

where

$$\phi_n = \tan^{-1} \frac{a_f \sin v_s}{b_f \cos v_s}$$

with respect to the reference coordinate system. The geometry of the coordinates is shown in Fig. B-5.

With the necessary elliptic cylinders being determined, the procedure to combine these two models to simulate the actual aircraft is the same as discussed in Section III. Thus, the volumetric patterns for off-center fuselage mounted airborne antennas can be determined.
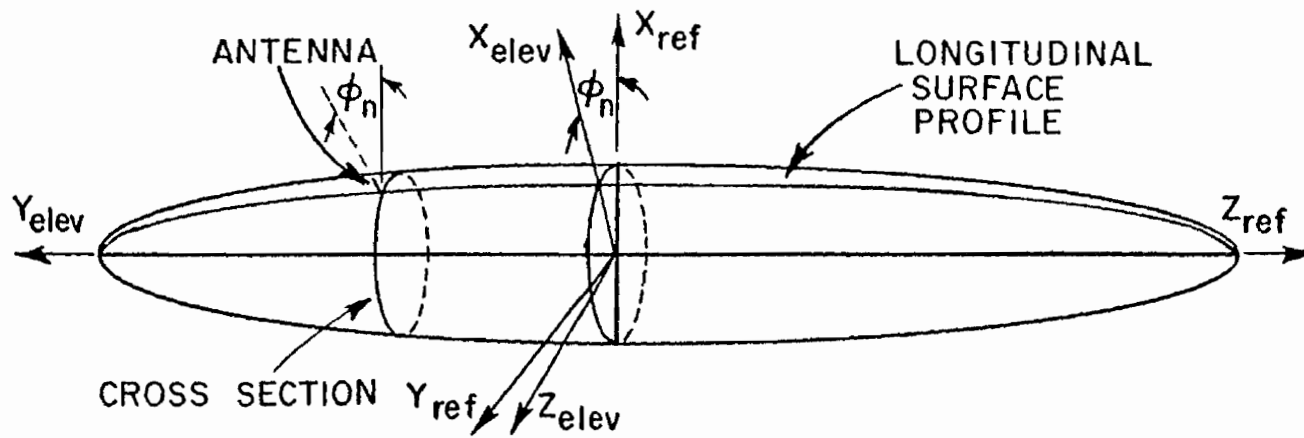
Figure B-5. Illustration of the coordinate system used in the elevation plane model relative to the reference coordinate system for off center line mounted antennas.

REFERENCES

1. Burnside, W. D., Gilreath, M. C., Marhefka, R. J., and Yu, C. L., "A Study of KC-135 Aircraft Antenna Patterns," IEEE Trans. on Antennas and Propagation, Vol. AP-23, No. 3, May 1975, pp. 309-16.

2. Burnside, W. D., "Analysis of On-Aircraft Antenna Patterns," Report 3390-1, August 1972, The Ohio State University Electro-Science Laboratory, Department of Electrical Engineering; prepared under Contract N62269-72-C-0354 for Naval Air Development Center. (AD 777 989)

3. Walter, C. H., Traveling Wave Antennas, Dover Publications, Inc., New York, 1970, pp. 15-16.

4. Carter, P. S., "Antenna Arrays Around Cylinders," Proc. IRE, Vol. 31, December 1943, pp. 671-693.

5. Carter, P. S., "Antenna on Cylindrical Fuselage," Report No. 895-11, RCA Laboratories, Rocky Point, N.Y.; December 24, 1943.

6. Sinclair, G., "The Patterns of Antennas Located Near Cylinders of Elliptical Cross Section," Proc. IRE, Vol. 39, No. 6, June 1951.

7. Richmond, J. H., "A Wire-Grid Model for Scattering by Conducting Bodies," IEEE Trans. Antennas and Propagation, Vol. AP-14, pp. 782-786, November 1966.

8. Richards, G. A., "A Boundary-Value Technique for Computing the Patterns of Antenna Near a Conducting Body of Arbitrary Shape," Report 2235-2, 11 September 1967, The Ohio State University ElectroScience Laboratory, Department of Electrical Engineering; prepared under Contract N10019-67-C-0063 for Naval Air Systems Command.

9. Richmond, J. R., "Computer Analysis of Three-Dimensional Wire Antennas," Report 2708-4, 22 December 1969, The Ohio State University ElectroScience Laboratory, Department of Electrical Engineering; prepared under Contract DAAD 05-69-C-0031 for Ballistic Research Laboratory.

10. Wang, N. N., Richmond, J. H., and Gilreath, M. C., "Sinusoidal Reaction Formulation for Radiation and Scattering from Conducting Surfaces," IEEE Trans. on Antennas and Propagation, Vol. AP-23, No. 3 (May 1975), pp. 376-382.

11. Ryan, C. E., Jr., and Rudduck, R. C., "Calculation of the Radiation Pattern of a General Parallel-Plate Waveguide Aperture for the TEM and TE_{01} Waveguide Modes," Report 1693-4, 10 September 1964, The Ohio State University ElectroScience Laboratory, Department of Electrical Engineering; prepared under Contract N62269-2183 for U. S. Naval Air Development Center, Johnsville, Pennsylvania.

12. Ryan, C. E., Jr., and Rudduck, R. C., "A Wedge Diffraction Analysis of the Radiation Patterns of Parallel-Plate Waveguides," IEEE Trans. on Antennas and Propagation Comm., Vol. AP-16, No. 4, July 1968.

13. Wu, D. C. F., Rudduck, R. C., and Pelton, E. L., "Application of a Surface Integration Technique to Parallel-Plate Waveguide Radiation Pattern Analysis," IEEE Trans. Antennas and Propagation, Vol. AP-17 (May 1969), pp. 280-285.

14. Burnside, W. D., and Pelton, E. L., "Wedge Diffraction Theory Analysis of Parallel-Plate Waveguide Arrays," Report 2382-14, 25 September 1969, The Ohio State University ElectroScience Laboratory, Department of Electrical Engineering; prepared under Contract F33615-67-C-1507 for the Air Force Avionics Laboratory at Wright-Patterson Air Force Base, Ohio.

15. Burnside, W. D., Pelton, E. L., and Peters, L., Jr., "Analysis of Finite Parallel-Plate Waveguide Arrays," to be published as a Communication in IEEE Trans. on Antennas and Propagation.

16. Yu, J. S., Rudduck, R. C., and Peters, L., Jr., "Comprehensive Analysis for E-Plane of Horn Antennas for Edge Diffraction Theory," IEEE Trans. on Antennas and Propagation, Vol. AP-14 (March 1966), pp. 138-149.

17. Yu, J. S., and Rudduck, R. C., "H-Plane Pattern of a Pyramidal Horn," IEEE Trans. on Antennas and Propagation Comm., Vol. AP-17, No. 5, September 1969.

18. Ratnasiri, P. A. J., Kouyoumjian, R. G., and Pathak, P. H., "The Wide Angle Side Lobes of Reflector Antennas," Report 2183-1, 23 March 1970, The Ohio State University Electro-Science Laboratory, Department of Electrical Engineering; prepared under Contract AF 19(628)-5929 for Air Force Cambridge Research Laboratories.

19. Mentzer, C. A., Pathak, P. H., and Peters, L., Jr., "Pattern Analysis of an Offset Fed Parabolic Reflector Antenna," Report 3220-2, June 1972, The Ohio State University ElectroScience Laboratory, Department of Electrical Engineering; prepared under Contract N00178-71-C-0264 for U. S. Naval Weapons Laboratory.

20. Ryan, C. E., Jr., and Rudduck, R. C., "Radiation Patterns of Rectangular Waveguides," IEEE Trans. on Antennas and Propagation Comm., Vol. AP-16 (July 1968), pp. 488-489.

21. Balanis, C. A., and Peters, L., Jr., "Analysis of Aperture Radiation from an Axially Slotted Circular Conducting Cylinder Using Geometrical Theory of Diffraction," IEEE T-AP-17, January 1969, pp. 93-97.

22. Balanis, C. A., and Peters, L., Jr., "Aperture Radiation from an Axially Slotted Elliptical Conducting Cylinder Using Geometrical Theory of Diffraction," IEEE T-AP-17, July 1969, pp. 507-513.

23. Balanis, C. A., and Peters, L., Jr., "Radiation from TE_{10} Mode Slots on Circular and Elliptical Cylinders," IEEE T-AP-18, No. 3, May 1970, pp. 400-403.

24. Ryan, C. E., Jr., "Analysis of Radiation Patterns of Antennas on Finite Circular Cylinders and Conically-Capped Cylinders," Report 2805-2, 25 September 1970, The Ohio State University ElectroScience Laboratory, Department of Electrical Engineering; prepared under Contract DAA21-69-C-0535 for Picatinny Arsenal.

25. "Low-Profile Scanned-Beam IFF Antenna System Development Study," Final Report 2836-4, 11 August 1970, The Ohio State University ElectroScience Laboratory, Department of Electrical Engineering; prepared under Contract N62269-69-C-0533 for Naval Air Development Center.

26. Burnside, W. D. and Marhefka, R. J., "Pattern Optimization of Wing-Mounted Array Antennas at UHF," Report 3884-1, January 1976, The Ohio State University ElectroScience Laboratory, Department of Electrical Engineering; prepared under Contract N00163-74-C-1580 for Naval Regional Procurement Office. Long Beach, California.

27. Marhefka, R. J., "Roll Plane Analysis of On-Aircraft Antennas," Report 3188-1, December 1971, The Ohio State University ElectroScience Laboratory, Department of Electrical Engineering; prepared under Contract N62269-71-C-0296 for Naval Air Development Center.

28. Yu, C. L., and Burnside, W. D., "Elevation Plane Analysis of On-Aircraft Antennas," Report 3188-2, January 1972, The Ohio State University ElectroScience Laboratory, Department of Electrical Engineering; prepared under Contract N62269-71-C-0296 for Naval Air Development Center.

29. Burnside, W. D., Marhefka, R. J., and Yu, C. L., "Roll Plane Analysis of On-Aircraft Antennas," IEEE Trans. on Antennas and Propagation, Vol. AP-21, November 1973, pp. 780-786.

30. Marhefka, R. J., and Burnside, W. D., "Numerical Solutions to Some On-Aircraft Antenna Pattern Problems," Technical Report 3390-4, October 1973, The Ohio State University ElectroScience Laboratory, Department of Electrical Engineering; prepared under Contract N62269-72-C-0354 for Naval Air Development Center.

31. Yu, C. L., and Burnside, W. D., "MLS Airborne Antenna Research," Semi-Annual Report 2902-22, May 1975, The Ohio State University ElectroScience Laboratory, Department of Electrical Engineering; prepared under Grant NGL 36-003-138 for National Aeronautics and Space Administration, Langley Research Center.

32. Yu, C. L., and Burnside, W. D., "Research on MLS Airborne Antenna," Semi-Annual Report 2902-23, in preparation, The The Ohio State University ElectroScience Laboratory, Department of Electrical Engineering; prepared under Grant NGL 36-003-138 for National Aeronautics and Space Administration, Langley Research Center.

33. Keller, J. F., "The Geometric Optics Theory of Diffraction," Proc. of the Symposium on Microwave Optics, Part II, McGill University (1953), pp. 207-210. (AD 211500)

34. Keller, J. B., "A Geometrical Theory of Diffraction," in Calculus of Variations and Its Applications, edited by L. M. Grover, McGraw-Hill Book Co. (1958), pp. 27-52.

35. Keller, J. B., "Geometrical Theory of Diffraction," Jour. Optical Soc. Amer., 52 (February 1962), pp. 116-130.

36. Sommerfeld, A., <u>Optics</u>, Academic Press, Inc., New York, 1954, pp. 245-265.

37. Rudduck, R. C., "Application of Wedge Diffraction to Antenna Theory," Report 1691-13, 30 June 1965, The Ohio State University ElectroScience Laboratory, Department of Electrical Engineering; prepared under Grant NsG-448 for National Aeronautics and Space Administration, Washington, D. C. Also published as NASA Report CR-372.

38. Pauli, W., "An Asymptotic Series for Functions in the Theory of Diffraction of Light," Phys Rev., $\underline{54}$ (1 December 1938), pp. 924-931.

39. Hutchins, D. L., and Kouyoumjian, R. G., "A New Asymptotic Solution to the Diffraction by a Wedge," URSI 1967 Spring Meeting, Ottawa, Canada, pp. 154-155.

40. Hutchins, D. L., "Asymptotic Series Describing the Diffraction of a Plane Wave by a Two-Dimensional Wedge of Arbitrary Angle," Ph.D. Dissertation, The Ohio State University, Department of Electrical Engineering, 1967.

41. Pathak, P. K., and Kouyoumjian, R. G., "The Dyadic Diffraction Coefficient for a Perfectly Conducting Wedge," Scientific Report No. 5, Report 2183-4, 5 June 1970, The Ohio State University ElectroScience Laboratory, Department of Electrical Engineering; prepared under Contract AF19(628)-5929 for Air Force Cambridge Research Laboratories.

42. Kouyoumjian, R. G., and Pathak, P., "A Uniform Geometrical Theory of Diffraction for an Edge of a Perfectly Conducting Surface," Proc. of the IEE, Vol. 62, No. 11, November 1974, pp. 1448-1461.

43. Levy, B. R., and Keller, J. B., "Diffraction by a Smooth Object," Institute of Mathematical Sciences, New York University, published under Contract No. AF 19(604)-1717; December 1957. Also in Comm. Pure Appl. Math., 12, 1959, pp. 159-209.

44. Franz, W., and Depperman, K., "Theorie der Beugang Am Zylinder unter Berucksichtigung der Kreichwelle," Ann. Physik, Vol. 10, June 1952, pp. 361-373.

45. Franz, W., and Depperman, K., "Theorie der Beugang der Kugel unter Berucksichtigung der Kreichwelle," Ann. Physik, Vol. 14, June 1954, pp. 253-264.

46. Kouyoumjian, R. G., "Asymptotic High-Frequency Methods," Proc. of the IEEE, Vol. 53, No. 8, August 1965, pp. 864-876.

47. Voltmer, D. V., "Diffraction by Doubly Curved Convex Surfaces," Ph.D. Dissertation, The Ohio State University, 1970.

48. Pathak, P., and Kouyoumjian, R. G., "An Analysis of the Radiation from Apertures in Curved Surfaces by the Geometrical Theory of Diffraction," Proc. of the IEE, Vol. 62, No. 11, November 1974, pp. 1438-1447.

49. Pathak, P. H., "Analysis of a Conformal Receiving Array of Slots in a Perfectly-Conducting Circular Cylinder by the Geometrical Theory of Diffraction," Technical Report 3735-2, January 1975, The Ohio State University ElectroScience Laboratory, Department of Electrical Engineering; prepared under Contract N00140-74-C-6017 for Naval Regional Procurement Office, Philadelphia Newport Division.

50. Pathak, P. H., and Kouyoumjian, R. G., "Effects of Torsional Surface Rays on the Radiation from Apertures in Convex Cylindrical Surfaces," presented at URSI Meeting, Boulder, Colorado, October 1974.

51. Kouyoumjian, R. G., and Pathak, P. H., "The Radiation from Torsional Surface Rays on Convex Cylinders," presented at URSI General Assembly, Lima, Peru, August 1975.

52. Pathak, P. H., and Luebbers, R. J., "An Analysis of the Radiation from Monopoles in Curved Surfaces by the Geometrical Theory of Diffraction," Report in preparation for publication, The Ohio State University ElectroScience Laboratory, Department of Electrical Engineering.

53. Wang, N. N., "Reaction Formulation for Radiation and Scattering from plates, Corner Reflectors and Dielectric-Coated Cylinders," Technical Report 2902-15, April 1974, The Ohio State University ElectroScience Laboratory, Department of Electrical Engineering; prepared under Grant NGR 36-008-138 for National Aeronautics and Space Administration, Langley

54. Jordan, E. C., and Balmain, K. G., Electromagnetic Waves and Radiating Systems, Prentice-Hall, Inc., New Jersey, 1968, pp. 375.

55. Pathak, P. H., "On Aircraft Antennas," Report 3973-2, January 1976, The Ohio State University ElectroScience Laboratory, Department of Electrical Engineering; prepared under Contract N62269-74-C-0788 for Naval Air Development Center.

56. Noble, Ben, Applied Linear Algebra, Prentice-Hall, Inc., New Jersey, 1969, pp. 142.